Title	Synthesis of Oxygen-Bridged π-Electronic Materials and Their Application to Organic Electronic Devices
Author(s)	中原, 勝正
Citation	大阪大学, 2014, 博士論文
Version Type	VoR
URL	https://doi.org/10.18910/34414
rights	
Note	

Doctoral Dissertation

Synthesis of Oxygen-Bridged π-Electronic Materials and Their Applications to Organic Electronic Devices

Katsumasa Nakahara
December 2013

Graduate School of Engineering,
Osaka University

Abstract

Recently, the importance of organic electronic devices has significantly increased from a field with great promise for both new materials and applications to a real industry. Organic semiconductors play important roles in printed electronics research owing to their environmentally friendly and low-cost availability for manufacturing processes. Organic materials therefore have greater potential than existing inorganic materials. Nowadays, various materials for organic devices such as organic field-effect transistors (OFETs), organic light-emitting diodes, and organic photovoltaics are being explored. Among these devices, OFETs, which have switching functions, are a key part of modern electronics. Materials that have carrier mobilities of over 1.0 cm^2 V^{-1} s^{-1} have been synthesized and reported to activate flat panel displays; however, there are other requirements for organic materials in addition to carrier mobility. Generally, the following four factors are necessary for the use of organic semiconducting materials: (1) an easy synthetic scheme for gram-scale production, (2) high thermal and chemical stabilities, (3) high solubilities in common organic solvents, and (4) high carrier mobilities, greater than or equal to 1.0 cm^2 V^{-1} s^{-1}, which is comparable to the value for amorphous Si. To address these issues, it is necessary to design and synthesize novel functional materials using synthetic organic chemistry methods. In this doctoral thesis, the author has focused on the molecular structures and properties of oxygen-bridged π-electronic systems, designed new organic semiconductors, and established a high-yield synthetic procedure. Moreover, the author found that these newly designed organic semiconductors have high field-effect mobilities of more than 1.0 cm^2 V^{-1} s^{-1}. The author also reports interesting light-emitting properties of these new materials, achieved by bridging π-systems with oxygen atoms.

This thesis consists of five chapters, and the details of each chapter are as follows. Chapter 1 describes the historical background and uses of organic semiconductors. The author focuses on organic compounds containing chalcogenophenes with bent structures, called V-shaped, W-shaped, and U-shaped compounds. Chapters 2 and 3 describe the synthesis, fundamental properties, aggregated structures, optical characteristics, and carrier transport performances of dinaphtho[2,3-*b*:2',3'-*d*]furan (V-shaped: **DNF–V**) derivatives and dinaphtho[1,2-*b*:2',1'-*d*]furan (W-shaped: **DNF–W**). Chapter 2 first describes the design and synthesis of the target materials. The author developed a facile synthetic scheme for **DNF–V** derivatives and showed, using photoelectron yield spectroscopy, that **DNF–V** derivatives and **DNF–W** are candidates for p-type semiconductors. X-ray single-crystal structural analysis provided information about the aggregated structures of these two types of compounds. Oxygen-bridged materials showed high absolute fluorescence quantum yields in the solid state. Thermal analysis revealed the stabilities of the materials against heat and the different phase-transition phenomena of two types of alkylated **DNF–V** (2,10-position-substituted: **C$_n$–DNF–VW**,

3,9-position-substituted: C_n**–DNF–VV**) derived by molecular rotation. Chapter 3 describes the carrier transport properties of **DNF–V** derivatives and **DNF–W**. The author then investigated the intrinsic carrier mobilities, using single crystals with no grain boundaries, and found that **DNF–V** derivatives had significant hole mobilities of more than 1.0 cm^2 V^{-1} s^{-1}. In contrast, the hole mobility of a single crystal of **DNF–W** was 10^{-2} cm^2 V^{-1} s^{-1}. This might result from differences in the packing structure. The author has developed a new class of organic electronic materials that not only have excellent light-emitting properties but also high charge-carrier-transporting capabilities. Chapter 4 describes dinaphtho[2,1-*b*:1',2'-*d*]furan (**DNF–U**) and dinaphtho[2,1-*b*:1',2'-*d*]thiophene (**DNT–U**), which are U-shaped materials with unique twisted π-electronic systems. The author was interested in the effect of twist-angle differences, derived from oxygen or sulfur atoms, on the packing structure and charge transport properties. X-ray single-crystal structural analysis showed that **DNF–U** molecules form two-dimensional herringbone packed structures. In contrast, **DNT–U** molecules form one-dimensional columnar π–π stacked structures. Because of the two-dimensional hole conduction in the single crystal, **DNF–U** marked 10 times higher values of two orders of magnitude compared to **DNT–U**. Chapter 5 discusses conclusions and future perspectives.

Synthesis of Oxygen-bridged π-Electronic Materials and Their Applications to Organic Electronic Devices

Table of Contents

Abbreviations and Symbols

The following abbreviations and symbols have been used in the text.

Anal.	elemental analysis
APCI	atmospheric pressure chemical ionization
Aq.	aqueous
Ar	aryl
a.u.	arbitrary unit
Bu	butyl
B3LYP	Becke's three-parameter hybrid with Lee, Yang, and Parr's correlation functional
Calcd	calculated
d	day(s)
d	doublet
dd	double doublet
δ	chemical shift of NMR signal in ppm
DFT	density functional theory
ε	molar absorption coefficient
eq	equivalent
Et	ethyl
Φ_F	fluorescence quantum yield
h	hour(s)
J	coupling constant in Hz
λ	wavelength
HOMO	highest occupied molecular orbital
HRMS	high-resolution mass spectrum
LUMO	lowest unoccupied molecular orbital
m	multiplet
Me	methyl
min	minute(s)
MS	mass spectrometry
m/z	mass-to-charge ratio
n-	normal
NMR	nuclear magnetic resonance
Ph	phenyl
Pr	propyl
q	quartet
R	an organic group
r.t.	room temperature
s	singlet
t-	tertiary

t   triplet

THF tetrahydrofuran

UV-vis ultraviolet and visible

XRD X-ray diffraction

Chapter 1
General Introduction

1.1 Organic Semiconductors

The history of organic semiconductor began in 1954. Akamatsu, Iguchi, and Matsunaga reported that charge transfer complexes composed of perylene and iodine had high conductivities.[1] In the late 1970s, Heeger, MacDiarmid, and Shirakawa, Nobel Prize laureates, discovered that doped acetylene had high electrical conductivity.[2,3] This discovery accelerated research and contributed to the advance of π-electronic organic materials as semiconductors. Organic π-conjugated materials have great potential as active elements in (opto)electronic devices that exploit their semiconducting properties, such as field-effect transistors (FETs),[4–9] light-emitting diodes (LEDs),[10] and photovoltaics (PVs).[11,12] These devices are expected to have applications such as incorporation into all-plastic integrated circuits for low-end and cheap electronics and all-plastic light-emitting displays, where each pixel consists of an organic LED (OLED) driven by an organic FET (OFET). For all of these applications, the efficiency of charge transport within the organic layers plays a key role. For example, in photovoltaic cells, the charges generated by photoexcitation are transported efficiently to be collected at metallic contacts and finally stored in the form of electrical energy. Another challenge is to develop materials displaying high electron and hole mobilities in field-effect device architectures for the design of complex organic circuits.

The key to high performance in all organic electronic devices is control of the molecular aggregated structure in the solid state.[13–16] In general, a good electronic performance requires strong intermolecular electronic coupling in the solid state, yielding strong π-overlap. There are two well-known two types of aggregated structure: one is herringbone and the other is π–π stacking (*Figure 1*). In the herringbone arrangement, the aromatic edge-to-face interaction dominates two-dimensional carrier transport.[17,18] In contrast, in face-to-face π–π stacking, one-dimensional carrier transport occurs in the crystalline phase. In terms of effective carrier transport in a single crystal or polycrystalline film, herringbone packing is more favorable than π–π stacking.
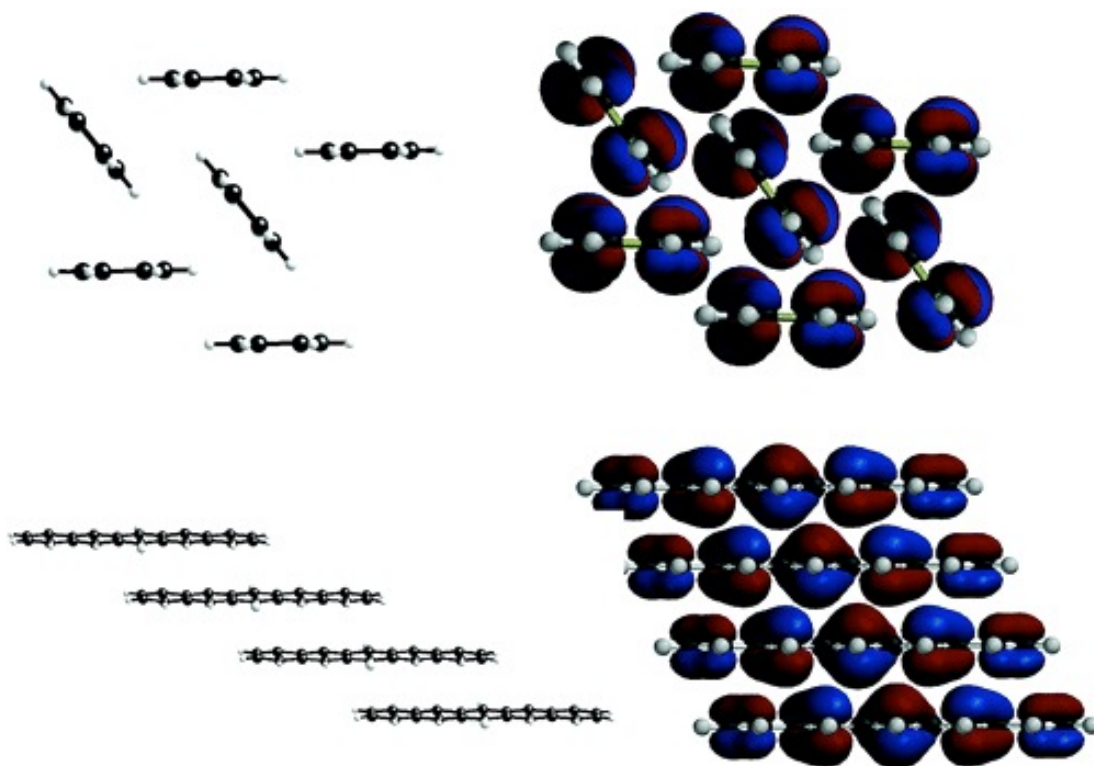
Figure 1. Herringbone (top) and π-stacking (bottom) arrangements of acenes, showing HOMO orbital interactions (Spartan '04, Wavefunction, Inc.)

Previously, some research groups have reported organic semiconductors with high carrier mobilities. In the late 1990s, it was reported that a pentacene polycrystalline thin film has a carrier mobility of 1.0 cm^2 V^{-1} s^{-1}, which is comparable to that of amorphous Si. This was a strong motivation to begin extensive studies of organic semiconductors.[19] Typical organic semiconducting materials consist mainly of π-electron-conjugated cores with rod-like molecular structures exhibiting high carrier mobilities, but are often poorly soluble because of strong π–π interactions.

Several approaches have been reported for overcoming this problem in the printed electronics industry. Anthony's group developed pentacene or anthradithiophene derivatives, in which the presence of outer bulky triisopropylsilyl groups enhances the solubility and the molecular aggregated structure. Pentacene substituted with triisopropylsilyl groups, which is called TIPS pentacene (*Figure 2*), is chemically stable and has a maximum mobility of 1.8 cm^2 V^{-1} s^{-1} for solution-processed devices.[20] Another approach is the introduction of long alkyl chains to thiophene-containing π-cores, as reported by Takimiya's group. Well-known materials are

benzothieno[3,2-*b*][1]benzothiophene (**BTBT**)[21] derivatives and dinaphtho[2,3-*b*:2',3'-*f*]thieno[3,2-*b*]thiophene (**DNTT**)[22] derivatives. Because such cores have advantageous intermolecular interactions between two sulfur atoms, these materials exhibit excellent performances, with mobilities above 10 cm^2 V^{-1} s^{-1}.[23] Fundamental research on OFETs is therefore based on promising **BTBT** and **DNTT** derivatives. The molecular design of these typical organic semiconductors with high carrier mobilities is mainly based on linearly or quasi-linearly fused molecular structures. However, such designed molecules often have insufficient solubilities and thermal durabilities, which prevents their practical use.


TIPS-Pentacene

TIPS-anthradithiophene

Alkyl-BTBT

Alkyl-DNTT
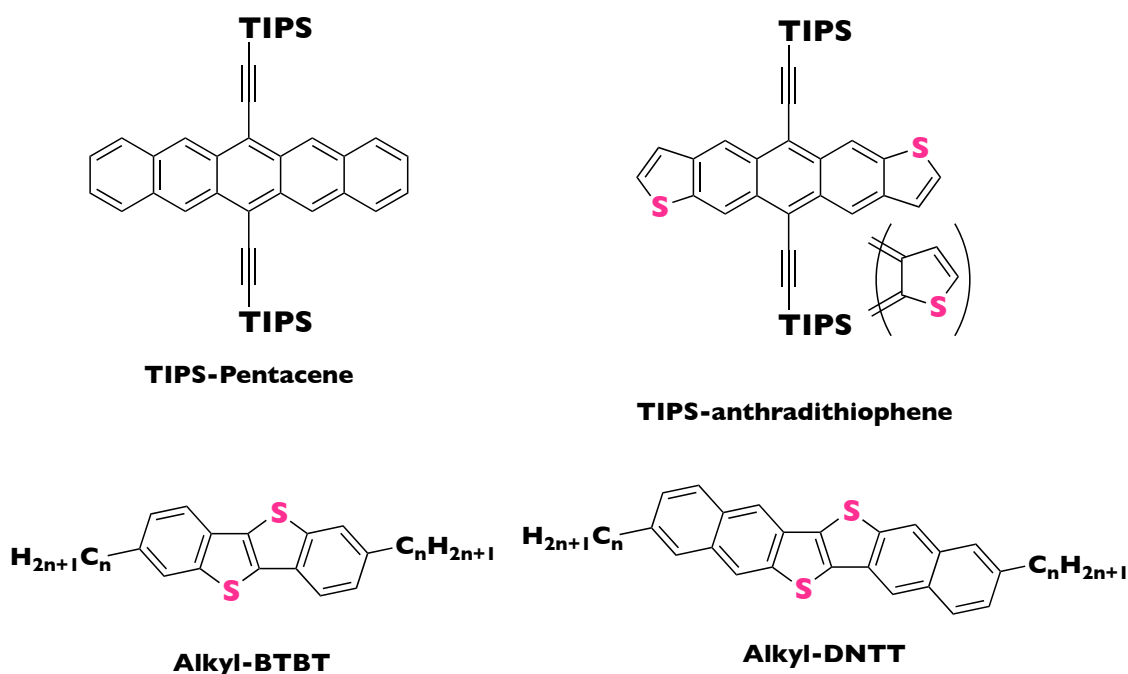
Figure 2. Representative organic semiconducting materials with high carrier mobilities.

1.2 Organic Semiconductors with Bent Structures

Instead of the traditional combination, our group originally proposed a conceptually new molecular design based on organic semiconductors with bent structures. Recently, our group reported extended V-shaped π-conjugated cores, dinaphtho[2,3-*b*:2',3'-*d*]thiophene (**DNT–V**) derivatives containing a thiophene ring at the central position, which are inherently soluble because of internal dipole moments and the large orbital coefficient of the highest occupied molecular orbital (HOMO) on the prominent sulfur atom, and are capable of high mobilities. A hexyl-substituted

DNT–V derivative (**C$_6$–DNT–VW**) exhibited excellent hole mobility up to 9.5 cm^2 V^{-1} s^{-1} in the form of a solution-crystallized single-crystalline thin film (*Figure 3*).[24]

Such a conceptually new molecular design could therefore be a milestone in the development of organic semiconductors for practical applications. Replacement of the central sulfur atom by other heteroatoms provides a large library of V-shaped materials.
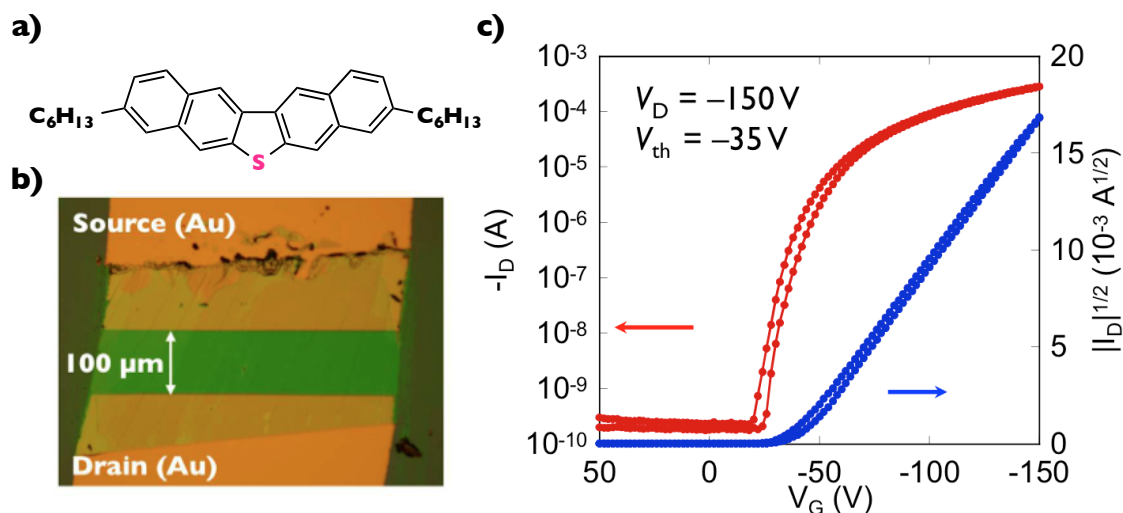
Figure 3. Recently reported novel organic semiconductor with outstanding hole mobility. a) Molecular structure of **C$_6$–DNT–VW**, b) solution-crystallized single-crystalline film, and c) transfer characteristics of OFET based on **C$_6$–DNT–VW**.

1.3 Characteristics of Oxygen-Bridged Organic Semiconductors

Furan is classified as a chalcogenophene analog because of its low stability under oxidation conditions.[25] In the presence of light, 3,4-unsubstituted furan rings are photooxidized to dicarbonyl compounds (*Scheme 1*). The problem of instability could be overcome by introducing various substituents or fused rings.

Scheme 1. Photooxidation of furan ring
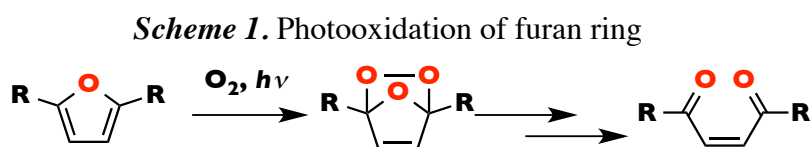
Furan-containing organic semiconductors have gained prominence because of their tightly packed crystal structures, which originate from their small element size.[26,27] The effects on the solid-state properties of the changes in the aggregated structure triggered

by altering the molecular structure by substitution of a sulfur atom for an oxygen atom is also interesting. In addition, the most important feature is efficient fluorescent properties. Representative furan-based semiconductors are shown in *Figure 4*. A well-balanced ambipolar material, 3,7-bis[4-(*N*-carbazolyl)phenyl]benzo[1,2-*b*:4,5-*b*']-difuran (**CZBDF**), which was reported by Nakamura's group, showed a hole mobility of 3.7×10^{-3} cm^2 V^{-1} s^{-1} and electron mobility of 4.4×10^{-3} cm^2 V^{-1} s^{-1}, evaluated using a time-of-flight (TOF) method. These values are the highest charge carrier mobilities reported for an amorphous material. The use of **CZBDF** has demonstrated that homojunction devices fabricated easily using appropriate ambipolar materials can provide viable routes to practical, useful OLEDs with the three primary colors of light.[28] Recently, Tanigaki's group reported a new furan-containing organic semiconductor, 2-(4-biphenyl)-5-[5-(4-biphenyl)-2-thienyl]furan (**BPFT**), which has a hole mobility of 0.27 cm^2 V^{-1} s^{-1} and a high fluorescence quantum yield of 51% in the solid state.[29] Bendikov's group has reported the electronic performances of linear α-oligofurans. The maximum field-effect mobility of **DH–6F** was 0.05 cm^2 V^{-1} s^{-1}. Additionally, **DH–6F** showed a higher photoluminescence quantum yield of 72% (in dioxane) than that of the α-oligothiophene analog **DH–6T** (38% in dioxane). As the author described above, oxygen-bridged π-conjugated compounds might be candidates for next-generation organic semiconductors, to solve the trade-off between carrier transport and photoluminescence, which has been difficult for sulfur-bridged organic molecules.
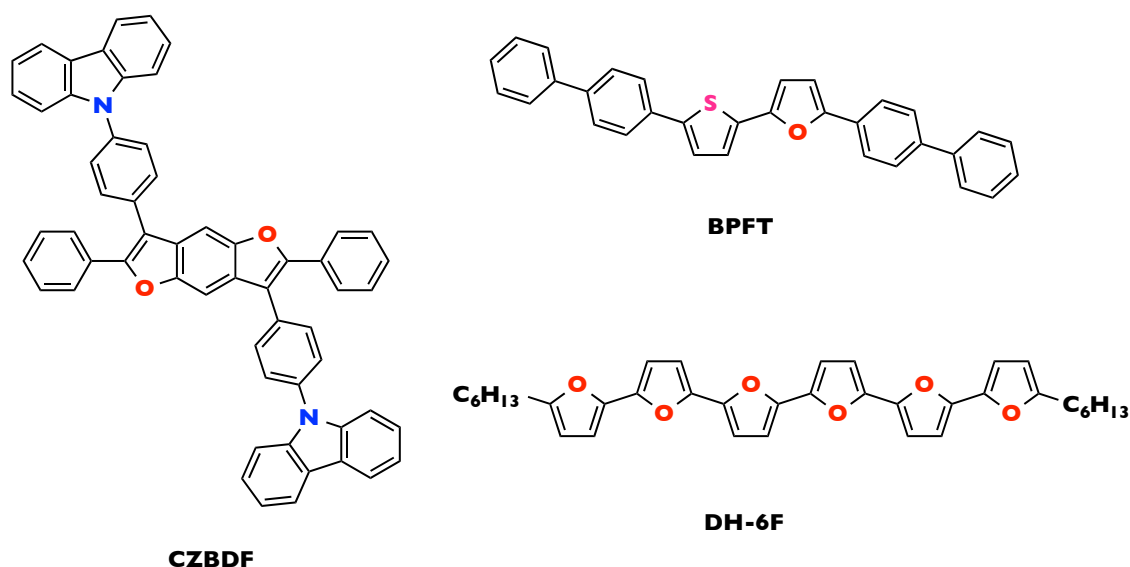
Figure 4. Recently reported furan-containing materials exhibiting high device performances.

Compared with thiophene-containing organic materials, furan-containing compounds show high emissivities. One reason for this might be the heavy atom effect. When a light atom is introduced, the probability of spin inversion is 0, as shown in Eq (1.1), where P is the probability of spin inversion, and the magnetic moments $|\alpha\rangle$ and $|\beta\rangle$ describe up and down spin states, respectively, because the Hamiltonian H representing interactions includes only electrostatic forces.

$$P \propto \left|\langle\alpha|H|\beta\rangle\right|^2 = 0 \qquad (1.1)$$

However, when a heavy atom is introduced, a large circular current is generated. Then Hamiltonian H includes a spin operator ($H = \xi \boldsymbol{L} \cdot \boldsymbol{S}$) because of the presence of spin–orbit coupling. As a result, the probability of spin inversion is not 0. The reason for the weak fluorescence of **DNT–V** derivatives (~3%) might be the heavy atom effect and sequential intercrossing system from the singlet excited state (S_1) to the triplet excited state (T_1). To add highly emissive properties to effective organic semiconductors with bent structures, the author focused on a light chalcogen atom, oxygen.

1.4 Purpose of this Study

As mentioned above, oxygen-bridged organic semiconductors potentially have both

effective carrier-transporting properties and high emissive properties. In this study, the author tried to combine these two molecular design concepts, and presented three types of bent molecular structure: V-shaped, W-shaped, and U-shaped (*Figure 5*). Chapter 2 describes the synthesis, fundamental properties, and crystal structures of dinaphtho[2,3-*b*:2',3'-*d*]furan (V-shaped: **DNF–V**) derivatives and dinaphtho[1,2-*b*:2',1'-*d*]furan (W-shaped: **DNF–W**). Furthermore, the author describes the interesting optical properties and phase-transition phenomena of these compounds. Chapter 3 describes the carrier-transporting capabilities of V-shaped and W-shaped organic semiconductors in FETs.

In Chapter 4 furan- and thiophene-based U-shaped organic semiconductors (**DNF–U** and **DNT–U**) are compared. Finally, in Chapter 5, the author summarizes this work and provides perspectives.
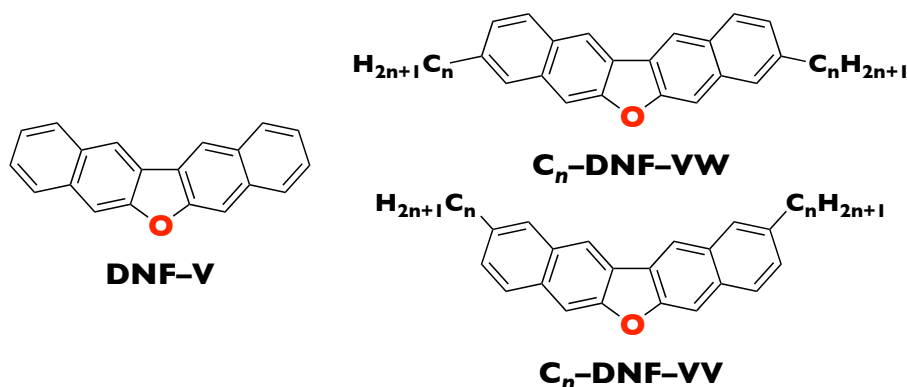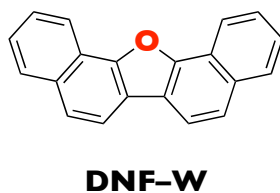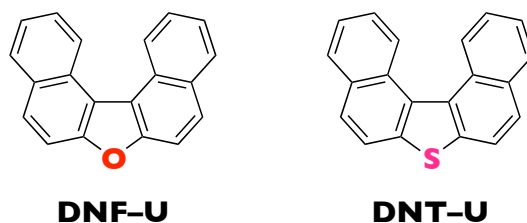

Figure 5. Organic materials with bent structures, which are candidates for semiconductors.

Chapter 2

Synthesis, Structures, and Physicochemical Properties of V-Shaped and W-Shaped Oxygen-Bridged Organic Semiconductors with Binaphthalene Frameworks

2.1 Introduction

Generally, organic semiconductors have π-conjugated molecular structures, and charge carriers (holes or electrons) move through active layers by intermolecular hopping or band transport. In organic electronic devices, π-orbital overlap critically affects the performances, as illustrated in *Figure 6*. According to Brédas's group,[30,31] the transfer integral for a tetracene cofacial dimer has the largest value, 500 meV, providing an upper limit for electronic couplings, although fully cofacial configurations are rarely encountered in actual aggregated structures when there is no molecular displacement. Effective π-orbital overlap between adjacent molecules is necessary to enhance the carrier transport abilities of organic semiconductors.
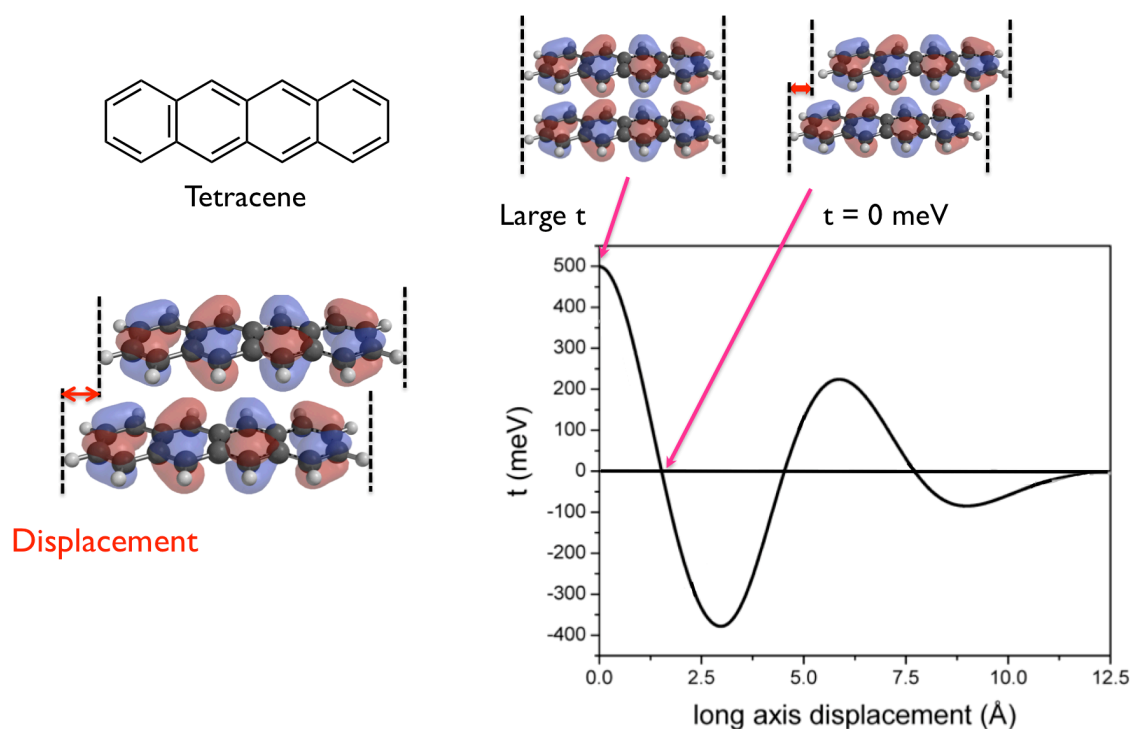
Figure 6. Evolution of intermediate neglect of differential overlap (INDO)[30,31]-calculated transfer integrals for electron and hole transfer in tetracene cofacial dimer, as a function of degree of translation of one molecule along its long axis; the intermolecular distance is set at 3.74 Å.

Recently, our group designed and reported **DNT–V**-based organic semiconductors with high carrier mobilities (*Figure 7*); the values depend on length and the positions of their alkyl chains on the **DNT–V** core. The displacement of the π-core varies from 0 to 1.27 Å, depending on the positions of the decyl groups on the **DNT–V** core. Because of

van der Waals interactions between alkyl groups, no molecular displacement was observed in the aggregated structure of **C$_{10}$–DNT–VW**. As the displacement became smaller, higher hole mobility was obtained.
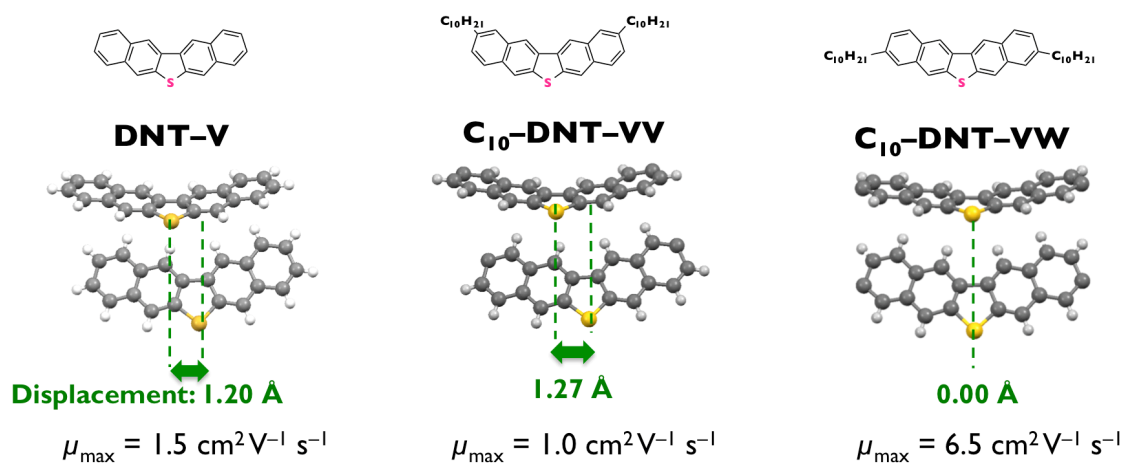

Figure 7. Comparison of molecular displacements (tail-to-tail molecules) of **DNT–V** derivatives. Alkyl chains were omitted for clarity.

As mentioned above, a V-shaped molecular structure is a promising framework for satisfying the requirements for highly efficient organic semiconducting materials. The physical and structural properties of a dinaphtho[2,3-*b*:2',3'-*d*]chalcogenophene core could be changed significantly by simply changing the central chalcogen atom from sulfur to oxygen, as illustrated in *Figure 8*. When the sulfur atom of **DNT–V** is replaced by an oxygen atom, the orbital coefficient of the chalcogen atom and the molecular bending angle (45° to 32°) become smaller. This oxygen-bridged V-shaped material is denoted by **DNF–V.**
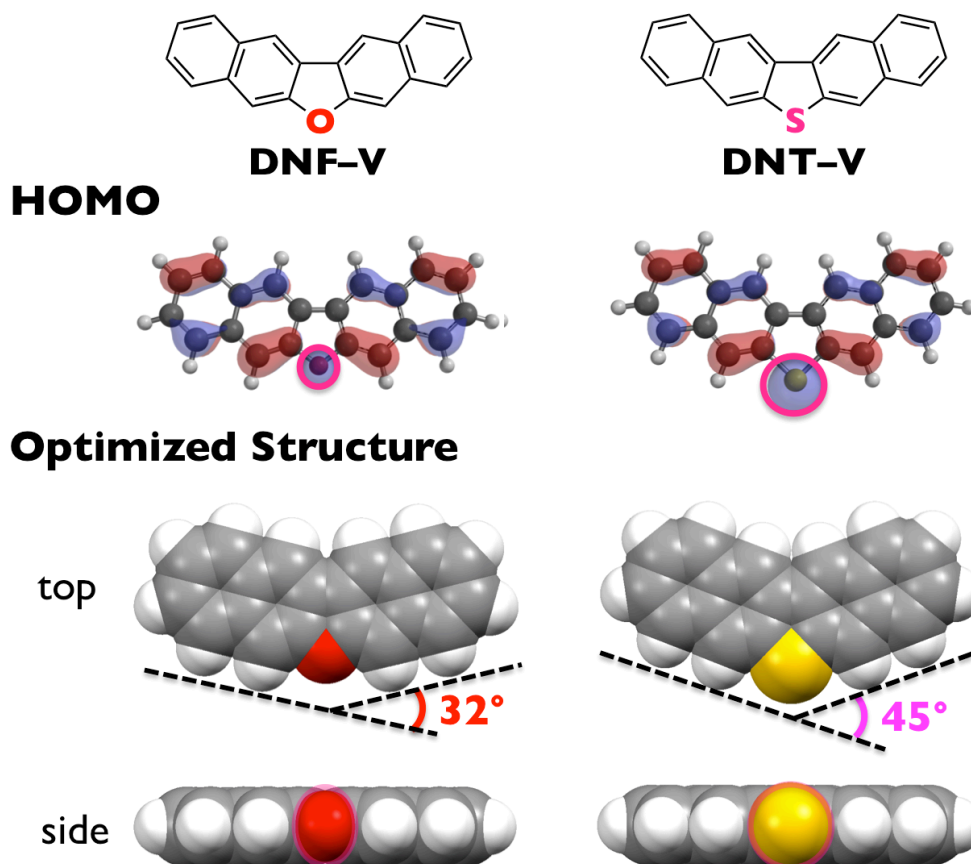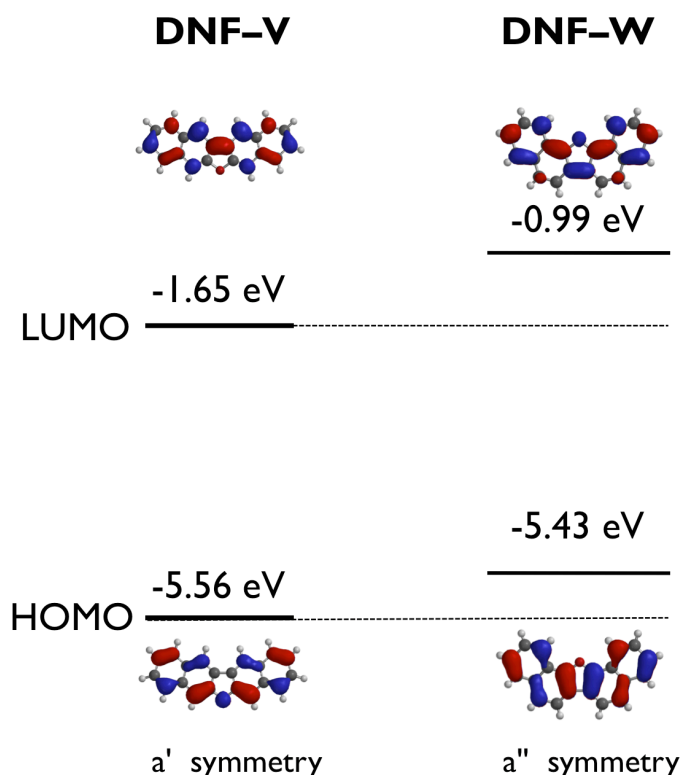
Figure 8. Comparison of HOMOs and structural features of **DNF–V** and **DNT–V**.

Theoretical calculations on **DNF–V** derivatives were carried out at the B3LYP/6-31G* level, using Spartan '04, to estimate their potential as organic semiconductors. *Figure 9* shows the frontier molecular orbitals of **DNF–V**, C_{10}–**DNF–VV**, and C_{10}–**DNF–VW** as representative materials. As illustrated in *Figure 9*, the HOMO levels of alkylated **DNF–V** derivatives were slightly higher than that of unsubstituted **DNF–V**, suggesting that these derivatives might be applicable in p-type semiconductors. The shallower HOMO levels of alkyl-**DNF–V**s stem from the electron-donating nature of the alkyl chain. These candidates for organic semiconductors have HOMO levels lower than –5.0 eV.[32] The calculation results indicate that **DNF–V** and its derivatives are air-stable organic semiconductors.
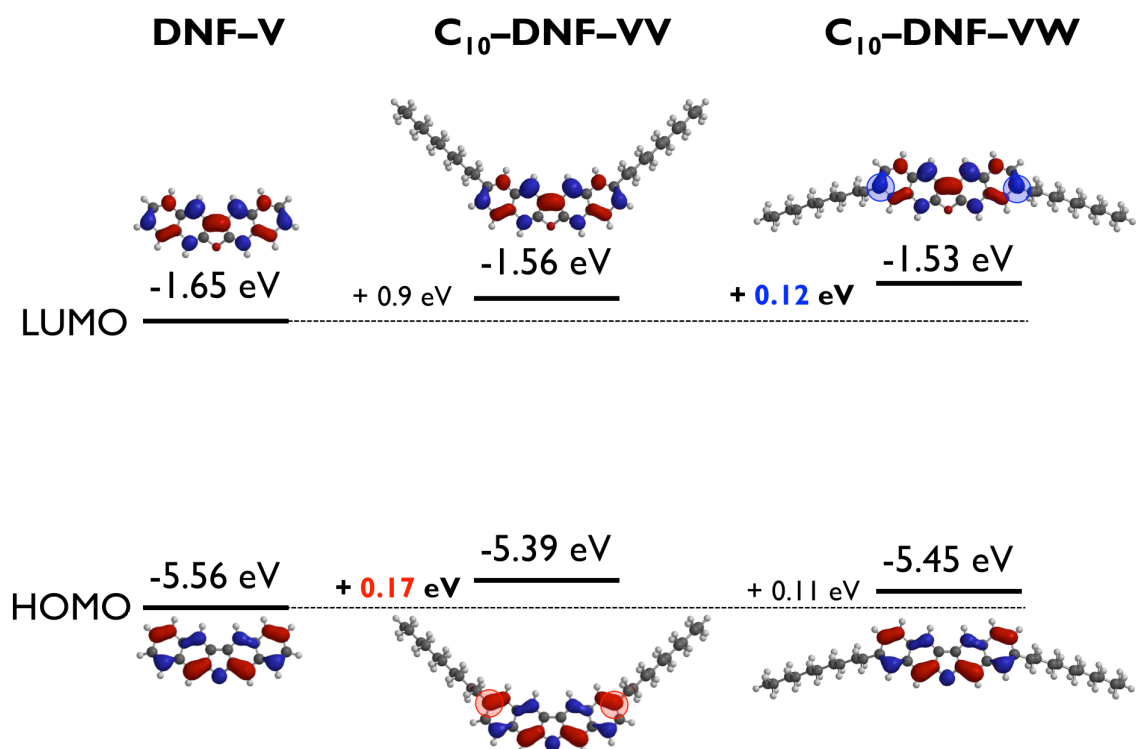
Figure 9. Frontier molecular orbitals of **DNF–V**, **C₁₀–DNF–VV**, and **C₁₀–DNF–VW**.

According to the literature on dinaphtho[1,2-*b*:2',1'-*d*]chalcogenophenes,[33] which are W-shaped organic semiconductors, the shape of the HOMO orbital of the dinaphtho[1,2-*b*:2',1'-*d*]furan (**DNF–W**) framework has a″ symmetry, exhibiting periodical changes in the sign of the wave function along the molecular long axis. The orbital energy level for a″ symmetry could be destabilized because of the shorter distance between antinodes with opposite signs on the chalcogenophene ring as the van der Waals radii and electronegativities of the chalcogen atom decrease. In contrast, the HOMO orbital on **DNF–V** has a′ symmetry. For a HOMO orbital with a′ symmetry, it is assumed that there is no phase change of the wave function and delocalization well along the molecular long axis, therefore the energy level is stabilized by the large electronegativity of the oxygen atom. The calculated values of the HOMO levels of **DNF–W** and **DNF–V** were –5.43 eV and –5.56 eV, respectively, which agree well with their orbital symmetries, as shown in *Figure 10*.

DNF–V　　　　　**DNF–W**

$$-0.99 \text{ eV}$$

$$-1.65 \text{ eV}$$

LUMO ————————————————————

$$-5.43 \text{ eV}$$

$$-5.56 \text{ eV}$$

HOMO ————————————————————

a' symmetry　　　　　a" symmetry

Figure 10. Frontier molecular orbitals of **DNF–V** and **DNF–W**.

In this chapter, the author compares the **DNF–V** and **DNF–W** frameworks in terms of physicochemical properties and structural features.

2.2 Synthesis

The author first synthesized decyl-substituted **DNF–V** (referred to for 3,9-substitution as **C₁₀–DNF–VW**, and for 2,10-substitution as **C₁₀–DNF–VV**) to examine the effect of the alkyl chain positions on the physical properties. **DNF–V** itself has already been synthesized by multiple steps in low yields (seven steps, 2% overall yield, *Scheme 2*).[34] Our recently developed facile and cost-effective synthetic protocol for the **DNF–V** framework was used to synthesize alkylated **DNF–V** derivatives, as shown in *Scheme 3*. Starting from either 2-decyl-7-methoxynaphthalene or 2-decyl-6-methoxynaphthalene, the homocoupling reaction proceeded smoothly via *ortho*-lithiation with *n*-butyllithium and oxidation using an iron(III) reagent. Subsequent demethylation afforded 2,2'-binaphthalene diols as the key precursors. Finally, on treatment with a zeolite catalyst,[35] dehydration proceeded to afford alkylated **DNF–V** derivatives in almost quantitative yield. In this synthetic methodology, the overall yields of **C₁₀–DNF–VW**

and **C$_{10}$–DNF–VV** were 67% and 63%, respectively. The author used this conventional procedure to introduce alkyl groups of various lengths into the **DNF–V** core at the 2,10- or 3,9-positions. The overall yields of alkyl-substituted **DNF–V** derivatives were approximately 50–60%, regardless of the alkyl chain length or substituent positions (*Table 1*).

Scheme 2. Previously reported synthetic route to **DNF–V**
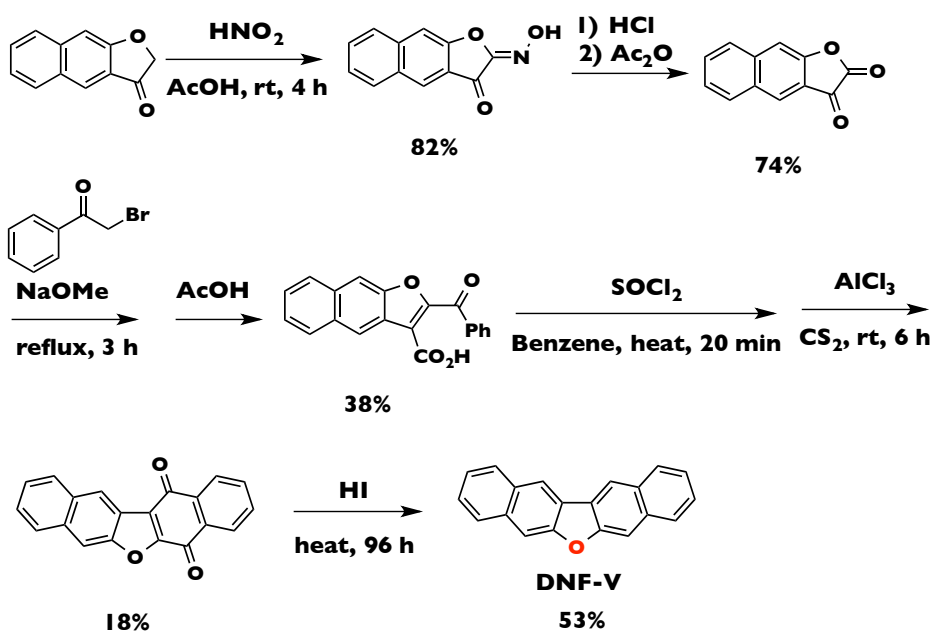
Scheme 3. Facile synthetic route to alkylated **DNF–V** derivatives
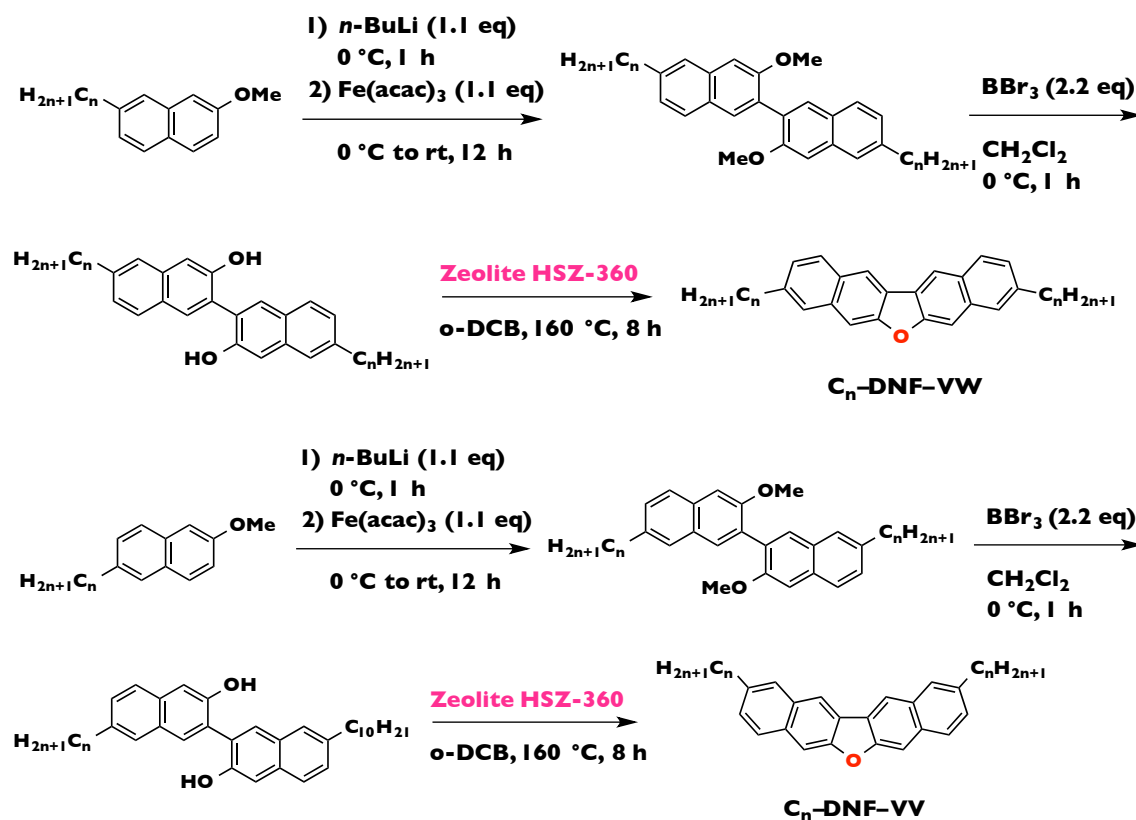
Table 1. Representative overall yields of C_n–DNF–VW and C_n–DNF–VV derivatives

Alkyl group (C_n)	Overall yield (%)[*]	
	C_n–DNF–VW	C_n–DNF–VV
Butyl (C_4)	60	–
Hexyl (C_6)	62	54
Decyl (C_{10})	67	63

[*]Overall yield was calculated from 2-alkyl-7-methoxynaphthalene (C_n–DNF–VW) or 2-alkyl-6-methoxynaphthalene (C_n–DNF–VV).

The solubility of an organic semiconductor is a crucial factor for applications to printed electronics. The author therefore tested the solubilities of these materials at room temperature. A series of C_n–DNF–VV derivatives exhibited high solubilities, over 1 wt%, in common organic solvents, as shown in *Table 2*. C_n–DNF–VV with shorter alkyl chains tended to have higher solubilities. C_6–DNF–VV exhibited extremely high

solubilities (3.22 wt% in chloroform and 2.37 wt% in toluene).

In contrast, unsubstituted **DNF–V** and **C$_n$–DNF–VW** had solubilities of less than 0.1 wt% under the same conditions. At 60 °C, the solubility of **C$_{10}$–DNF–VW** reached 0.165 wt% in toluene. As reported by our group, the solubilities of V-shaped materials in organic solvents depend on the internal dipole moments.[24] **DNTT** or **C$_{10}$–DNTT**, with no internal dipole moments, exhibited very low solubilities. In contrast, V-shaped sulfur-bridged organic semiconductors had much higher solubilities in common organic solvents. In a series of **DNT–V** derivatives, **C$_{10}$–DNT–VV**, with an internal dipole moment of 2.33 D had a solubility of 9.85 wt% in chloroform at room temperature. As shown in *Table 2*, the calculated internal dipole moments of **C$_n$–DNF–VV** (*n* = 6, 8, 10) range from 1.44 to 1.47 D. In comparison, the calculated internal dipole moments of **DNF–V** and **C$_{10}$–DNF–VW** were 0.39 and 0.95 D. The relatively low solubilities of these materials might be derived from the small internal dipole moments and aggregation densities.

*Table 2*. Solubilities of **C$_n$–DNF–VV** at room temperature

Alkyl group (C$_n$)	Solubility (wt%)		Internal dipole moment (D)
	Chloroform	Toluene	
Hexyl (C$_6$)	3.22	2.37	1.44
Octyl (C$_8$)	2.56	2.06	1.47
Decyl (C$_{10}$)	1.58	1.35	1.47

Dinaphtho[1,2-*b*:2',1'-*d*]furan (**DNF–W**) was synthesized using the procedure reported in the literature (*Scheme 4*).[36]

Scheme 4. Synthesis of **DNF–W**

DNF-W

64 %
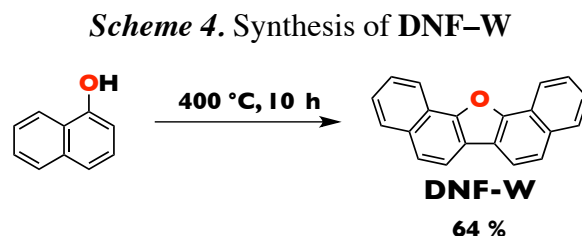
2.3 Energy Levels

To estimate the ionization potentials (IPs) of **C_{10}–DNF–VW** and **C_{10}–DNF–VV** in thin films, the author performed photoelectron yield spectroscopy (PYS) using vacuum-deposited thin films on quartz substrates (*Figure 11*). The PYS results show that the ionization potentials of alkylated **DNF–V**s, i.e., 5.73 eV (**C_{10}–DNF–VW**) and 5.77 eV (**C_{10}–DNF–VV**), are smaller than those of unsubstituted **DNF–V** (5.93 eV). The smaller ionization potentials of alkyl-**DNF–V**s are derived from the electron-donating nature of the alkyl chains. In the use of **DNF–V** derivatives as p-type semiconducting materials, hole injection from a gold electrode (IP: 5.1 eV) might occur preferentially. A similar tendency was observed for hexyl-substituted derivatives (**C_6–DNF–VW** and **C_6–DNF–VV**), as summarized in Table 3.
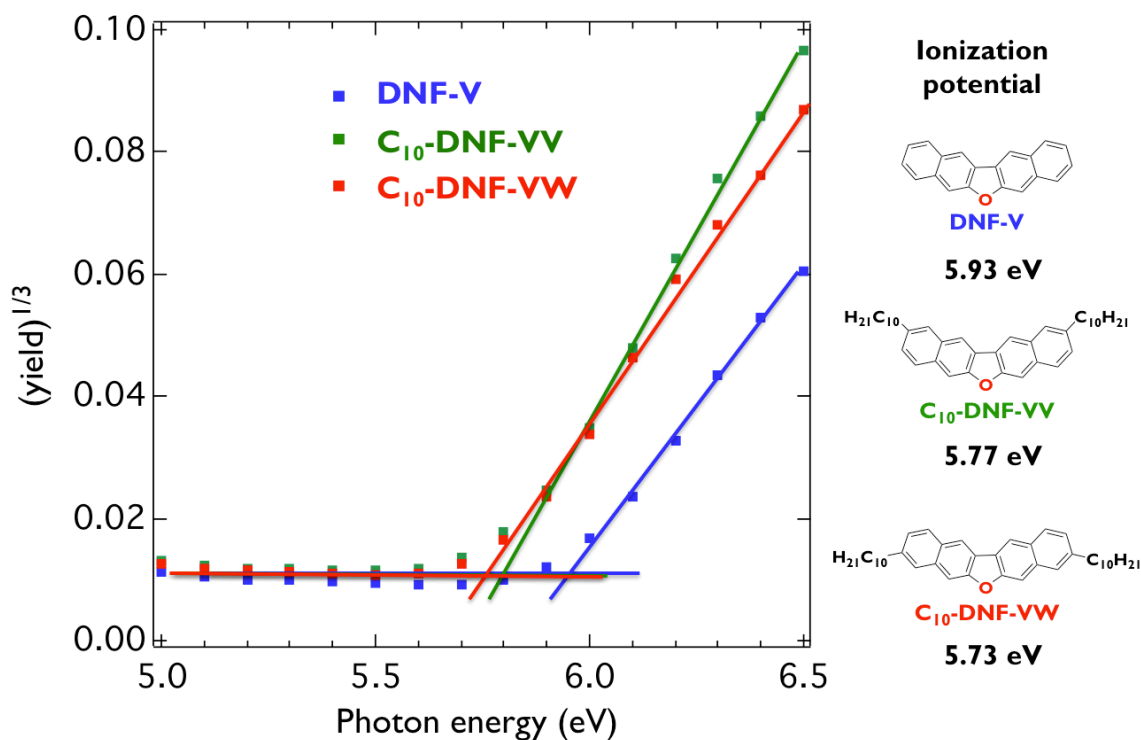
Figure 11. Photoelectron yield spectra of **DNF–V**, **C_{10}-DNF–VW**, and **C_{10}–DNF–VV** in thin films on quartz substrates after light illumination from a D_2 lamp in vacuo.

The IP of **DNF–W** was also estimated using PYS. The IP value of **DNF–W** was smaller than that of **DNF–V**, as shown in *Figure 12*; this is consistent with the calculated results.
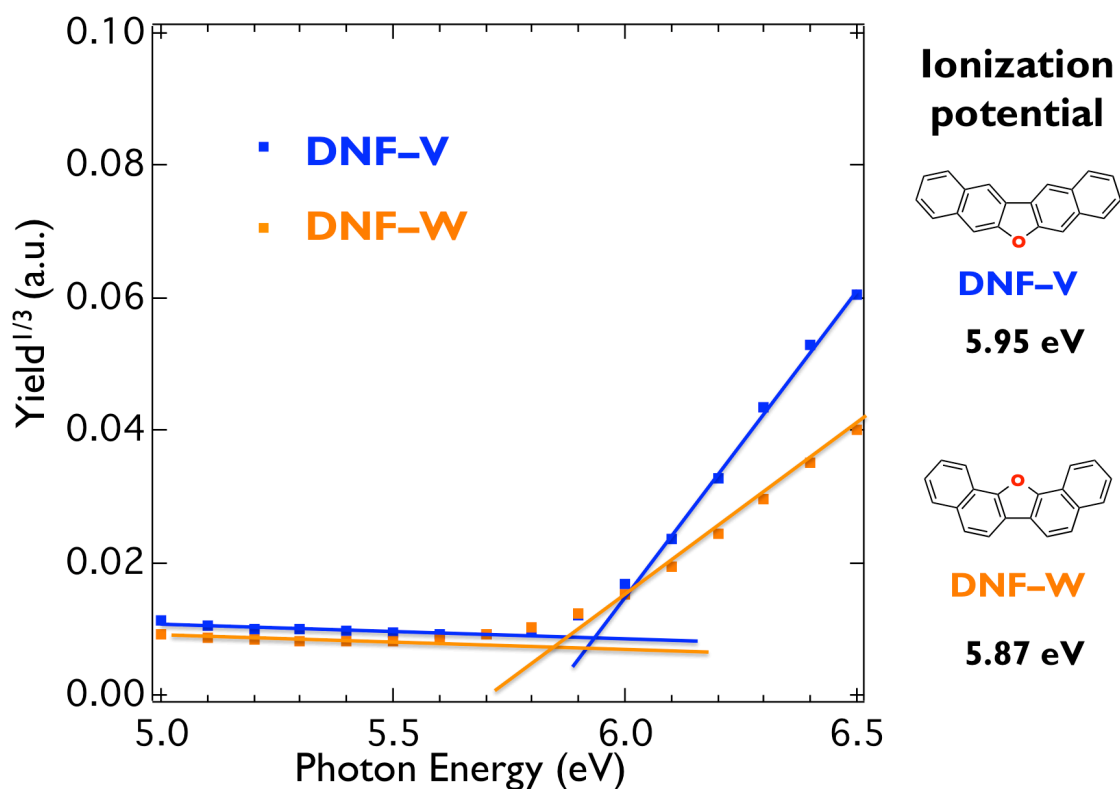
Figure 12. Photoelectron yield spectra of **DNF–V** and **DNF–W** in thin films on quartz substrates after light illumination from a D_2 lamp in vacuo.

Table 3. Ionization potentials of furan-based organic semiconductors, evaluated by PYS

Compound	Ionization potential (eV)
DNF–V	5.93
C$_{10}$–DNF–VW	5.73
C$_{10}$–DNF–VV	5.77
C$_6$–DNF–VW	5.78
C$_6$–DNF–VV	5.80
DNF–W	5.87

2.4 Thermal Stability

Chemical stability against heat is an important factor for thermally durable organic electronic devices. Thermogravimetric analysis (TGA) was performed on alkyl-substituted **DNF–V** derivatives to examine their thermal stabilities. No thermal

decomposition was observed for any material up to 500 °C under N_2 (*Figure 13* and *Figure 14*).
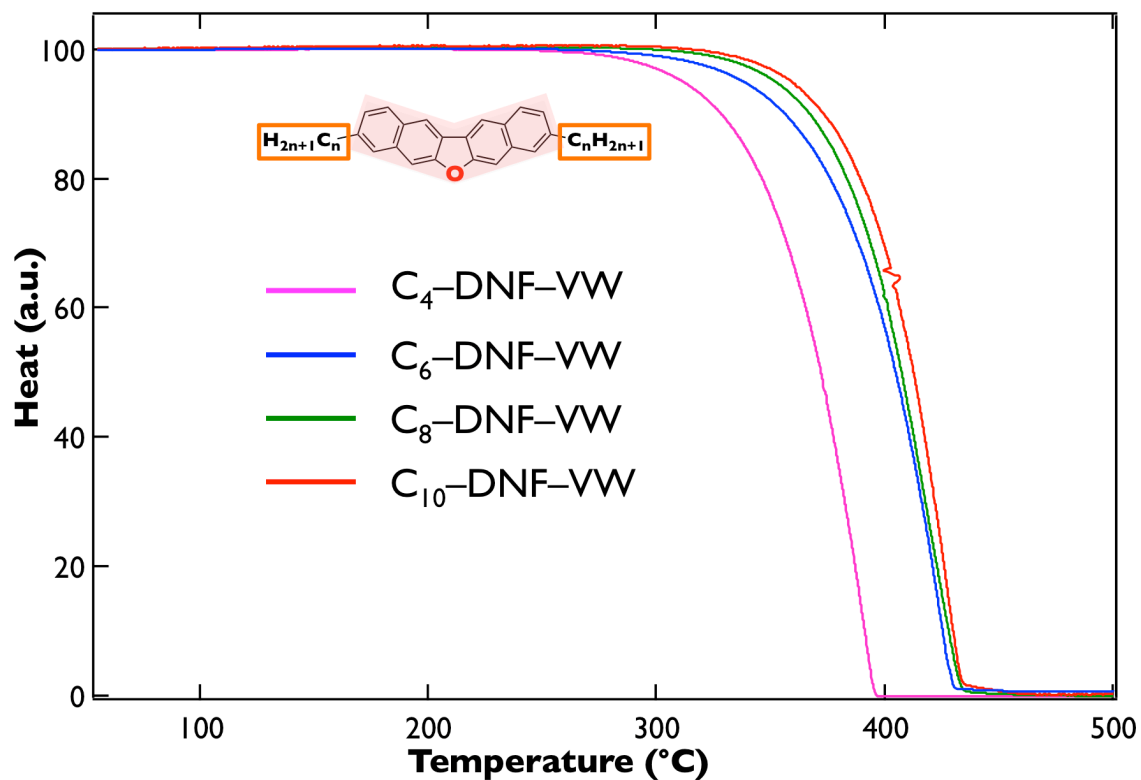
Figure 13. TGA charts of **C_n–DNF–VW**. Magenta line: **C_4–DNF–VW**, blue line: **C_6–DNF–VW**, green line: **C_8–DNF–VW**, and red line: **C_{10}–DNF–VW**.
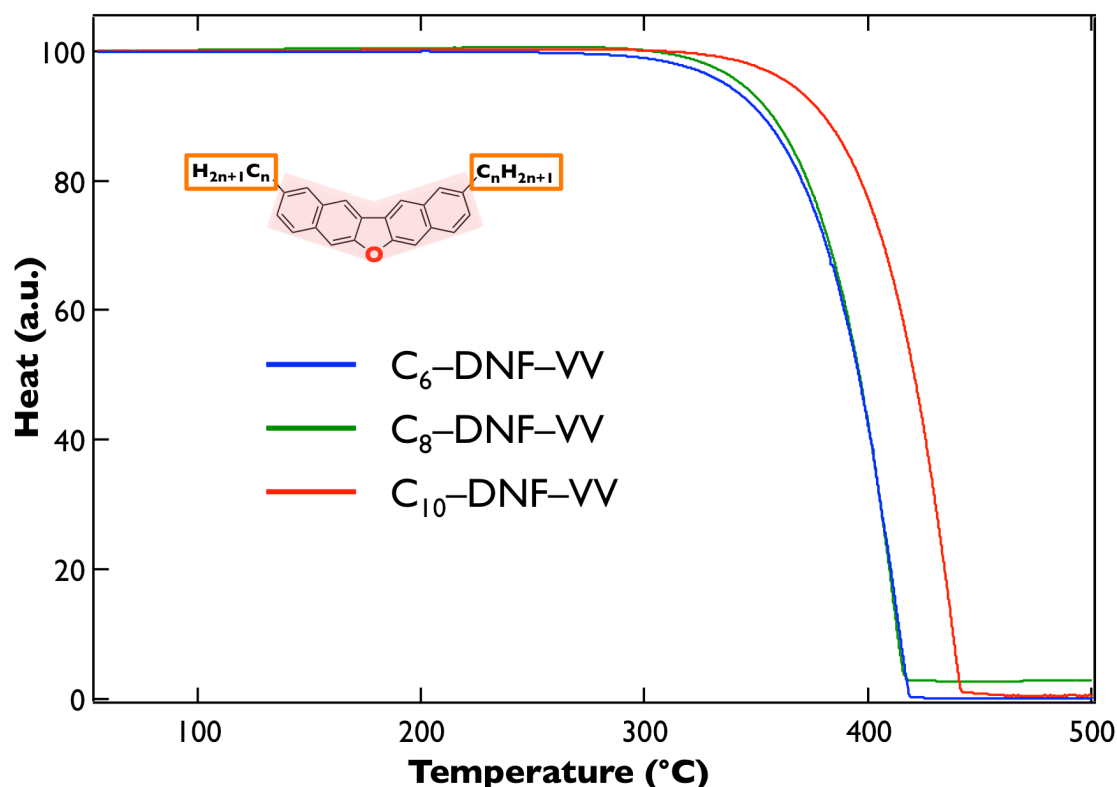
Figure 14. TGA charts of **C$_n$–DNF–VV**. Blue line: **C$_6$–DNF–VV**, green line: **C$_8$–DNF–VV**, and red line: **C$_{10}$–DNF–VV**.

2.5 X-Ray Single-Crystal Structural Analysis

To determine their intermolecular interactions and investigate their carrier-transporting abilities, the author performed X-ray single-crystal structural analyses on alkylated **DNF–V** derivatives. Single crystals were obtained by recrystallization from a mixture of toluene and 2-propanol. The obtained thin-platelet single crystals were successfully analyzed using single-crystal X-ray diffraction. **C$_{10}$–DNF–VW** assumes a slightly bent structure with a dihedral angle of 5.91° between two naphthalene units in the crystal, as illustrated in *Figure 15*, contrary to the calculated results, in which the optimized geometries are completely planar structures. The distorted structure in the single crystal can be explained by the characteristics of V-shaped molecules. The herringbone packing of the **DNF–V** core affects the planarity of neighboring **DNF–V** molecules in head-to-head and tail-to-tail fashions. When the **DNF–V**s are distorted out of plane along both the head and tail molecules, the π-cores effectively interact with each other by intermolecular interactions such as van der Waals forces. The molecular geometries are therefore transformed into non-planar structures along with the adjacent V-shaped

21

molecules. Such distortion should also simultaneously increase the attractive term with respect to intermolecular C–H···π interactions (*Figure 16*, *Figure 17*, and *Figure 18*). The structure of **C$_{10}$–DNF–VV** was much more non-planar. As shown in *Figure 18*, interactions between outer benzene rings and protons on the 1-positions of alkyl chains were observed.
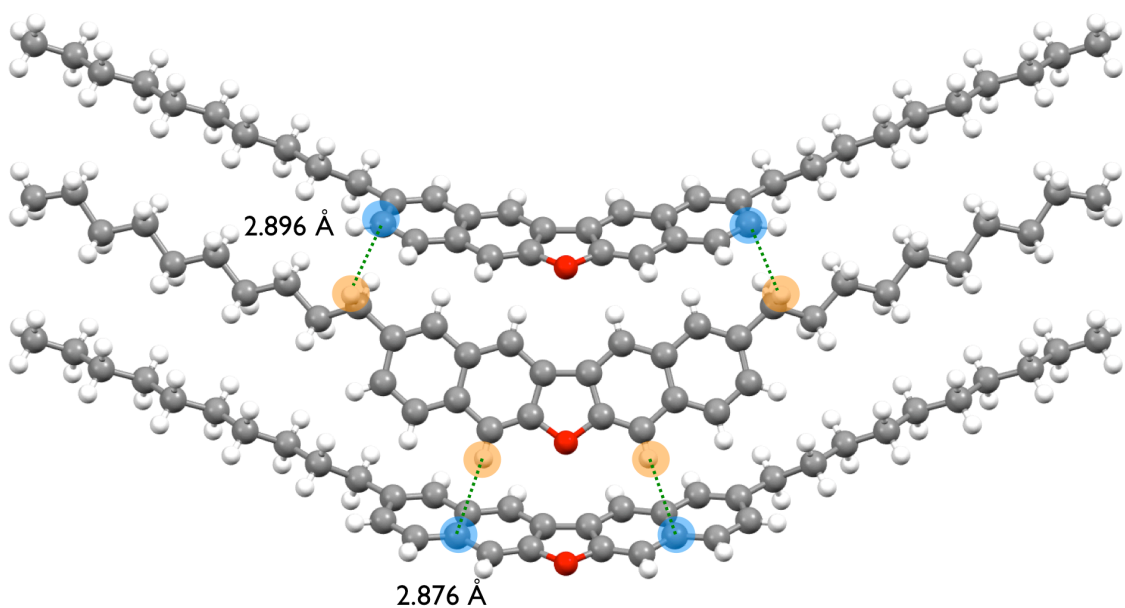

C$_{10}$–DNF–VW

Front View

5.91°

Side View

DNF–V: 4.00°

C$_{10}$–DNF–VV: 8.98°
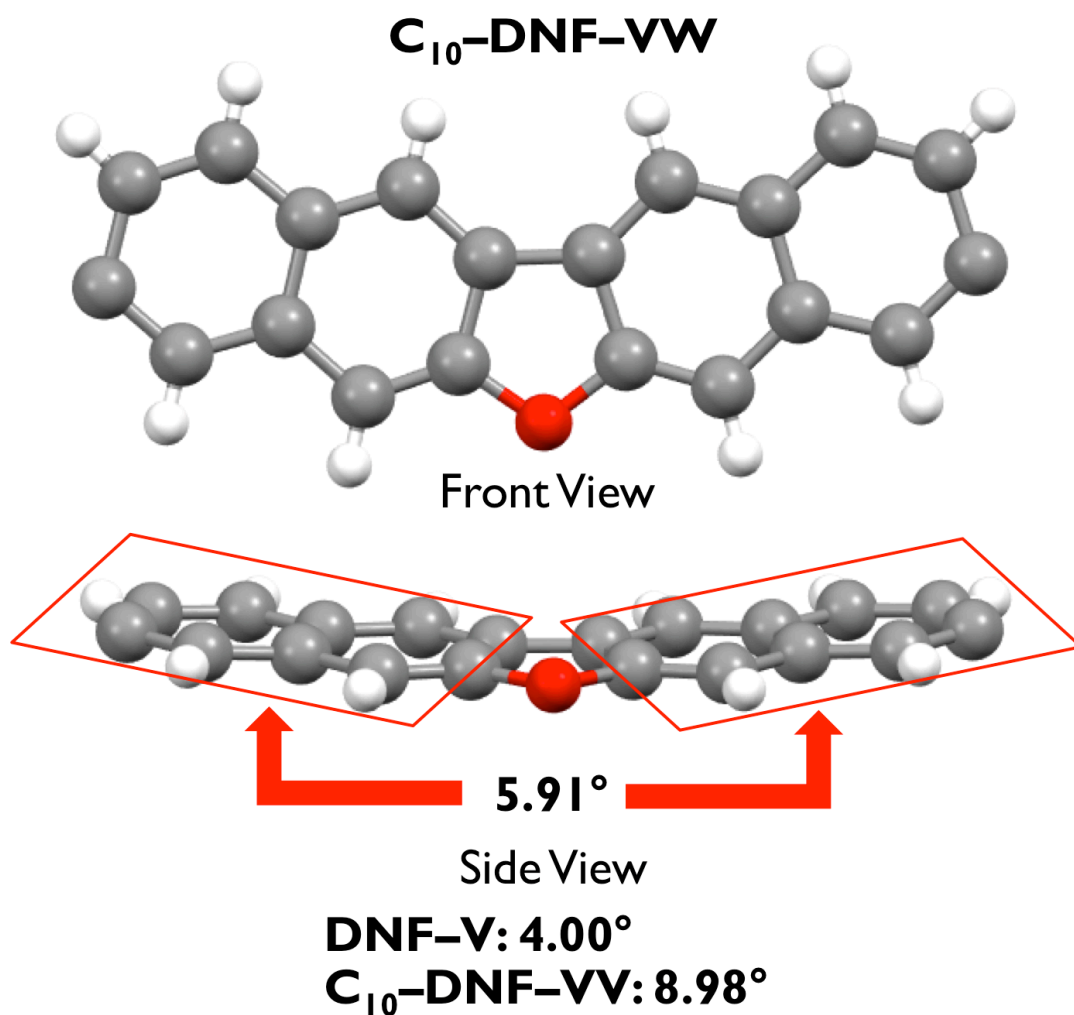
Figure 15. Front and side views of molecular structure of **C$_{10}$–DNF–VW**, and bending angles of **DNF–V** derivatives. The decyl groups were omitted for clarity.
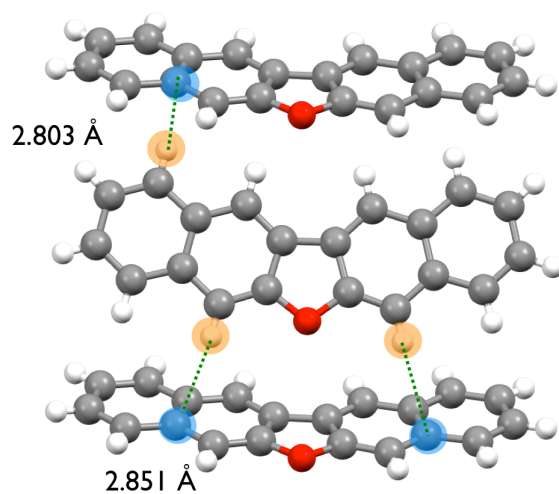
Figure 16. Neighboring intermolecular short contacts in **DNF–V**.
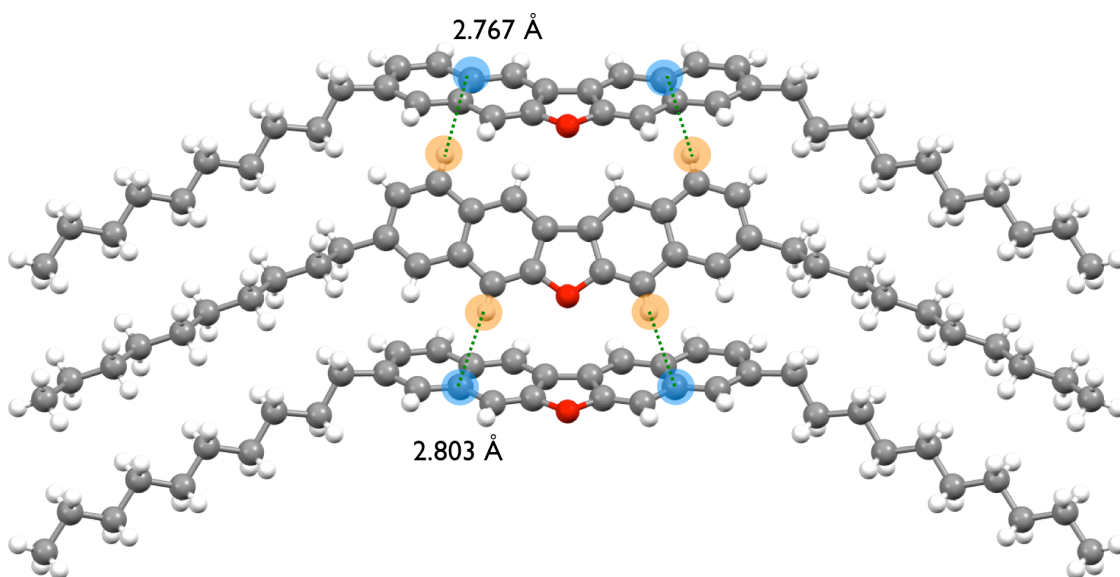
*Figure 17.* Neighboring intermolecular short contacts in **C$_{10}$–DNF–VW**.

Figure 18. Neighboring intermolecular short contacts in **C$_{10}$–DNF–VV**.

Table 4 and *Figure 19* show the molecular displacements and distances between the centers of masses for oxygen- or sulfur-bridged V-shaped organic semiconductors. Both **DNF–V** itself and alkylated **DNF–V** derivatives stack in a herringbone-packed manner, in which each molecule interacts with adjacent molecules with slight or no displacement, whereas **DNT–V** and **C$_{10}$–DNT–VV** form assembled structures with non-negligible molecular displacements, mainly because of the element sizes. These results indicate that an oxygen-bridged V-shaped π-core is less susceptible to molecular displacement in an aggregated structure than its sulfur-bridged counterparts are, therefore the **DNF–V** derivatives synthesized in this study exhibit high FET performances, regardless of the substituent positions.
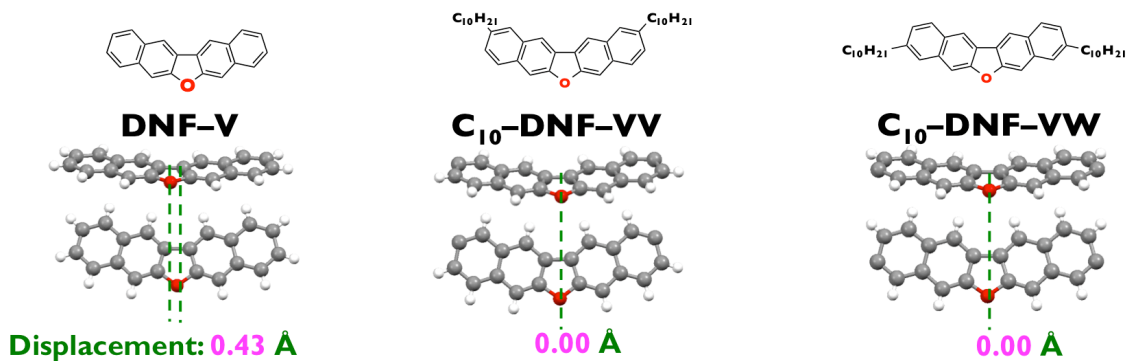
Table 4. Estimation of molecular displacements and distances between centers of masses based on single-crystal data for **DNF–V**, **C$_{10}$–DNF–VV**, **C$_{10}$–DNF–VW**, and **DNT–V** derivatives
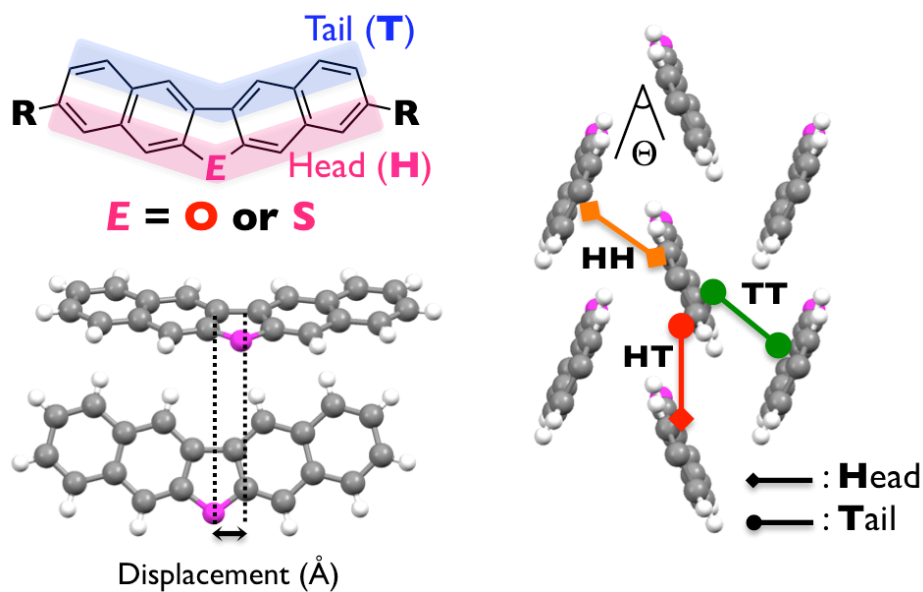
Compound	Displacement (Å)^a			Center of mass (Å)^b		
	HH	HT	TT	HH	HT	TT
DNF–V	0.01	0.03	0.43	4.83	5.97	4.82
C$_{10}$–DNF–VW	0.00	0.00	0.00	4.75	5.91	4.68
C$_{10}$–DNF–VV	0.00	0.00	0.00	4.74	6.06	5.07
DNT–V	0.75	0.22	1.20	4.92	6.39	5.12
C$_{10}$–DNT–VW	0.00	0.00	0.00	4.88	6.09	5.02
C$_{10}$–DNT–VV	1.06	0.24	1.27	4.90	6.75	5.27

^{a} Displacement between centers of masses. ^{d}Distance between centers of masses.

Displacement: 0.43 Å   **0.00 Å**   **0.00 Å**

Figure 19. Comparison of molecular displacements (tail-to-tail interactions) of **DNF–V** derivatives in single crystals. Alkyl chains were omitted for clarity.

The mechanisms of carrier transport in organic crystals are interpreted based on the hopping conduction model. The model for hopping rates is the Marcus expression for semi-classical electron transfer rates.[37] The hopping rate between neighboring molecules W is described as

$$W = \frac{t^2}{\hbar}\left(\frac{\pi}{\lambda k_B T}\right)^{1/2} \exp\left(-\frac{\lambda}{4 k_B T}\right) \qquad (2.1)$$

where t is the matrix element of electronic coupling (transfer integral), λ is the reorganization energy, k_B is the Boltzmann constant, and T is the temperature. When the hopping rate W is evaluated, the diffusion coefficient D is translated to

$$D = \frac{1}{6}\sum_i r_i^2 W_i P_i \qquad (2.2)$$

where i is an index to distinguish a combination of two molecules, r_i is the distance between centers of masses, and P_i is ith intermolecular hopping rate. P_i is written as

$$P_i = \frac{W_i}{\sum_i W_i} \qquad (2.3)$$

The theoretical charge carrier mobility μ is then given by the following equation, using D and the elementary charge e (Einstein's relational expression):

$$\mu = \frac{e}{k_B T} D \qquad (2.4)$$

The transfer integral t therefore affects the carrier transport properties and indicates the type of intermolecular overlap. According to Brédas's group,[18] the transfer integral t is obtained as

$$t = \frac{H_{RP} - S_{RP}\left(H_{RR} + H_{PP}\right)/2}{1 - S_{RP}^2} \qquad (2.5)$$

where H_{RP} is the charge transfer integral, S_{RP} is the spatial overlap between two molecules, and H_{RR} and H_{PP} are the site energies for each molecule. Each factor is described as follows:

$$H_{RP} = \left\langle \Psi_1 \middle| H \middle| \Psi_2 \right\rangle \qquad (2.6)$$

$$S_{RP} = \left\langle \Psi_1 \middle| \Psi_2 \right\rangle \qquad (2.7)$$

$$H_{RR} = \left\langle \Psi_1 \middle| H \middle| \Psi_1 \right\rangle \qquad (2.8)$$

$$H_{PP} = \left\langle \Psi_2 \middle| H \middle| \Psi_2 \right\rangle \qquad (2.9)$$

H is the electronic Hamiltonian (Kohn–Sham Hamiltonian[38]) of the dimer, and Ψ_1 and Ψ_2 are the wave functions of the two charge-localized states (HOMO for p-type or LUMO for n-type). The obtained crystal structures of the organic semiconductors are used to calculate all the transfer integrals at the DFT level with the PW91 functional and Slater-type triple-ζ plus polarization (TZP) basis set.[21,39,40] The author used the Amsterdam Density Functional (ADF) program.[41,42] The ADF program provided plausible results compared with those obtained using a program based on the extended Hückel method by Mori's group.[43,44] *Figure 20* depicts the calculated transfer integrals of **DNF–V** derivatives. Because the HOMO orbital on the oxygen atom is small for each material, the values of the transfer integrals along the head-to-tail direction are also

small. However, the transfer integrals along the head-to-head and tail-to-tail directions are relatively well balanced, therefore compensation for the lack of one component by two-dimensional conduction pathways might be expected.
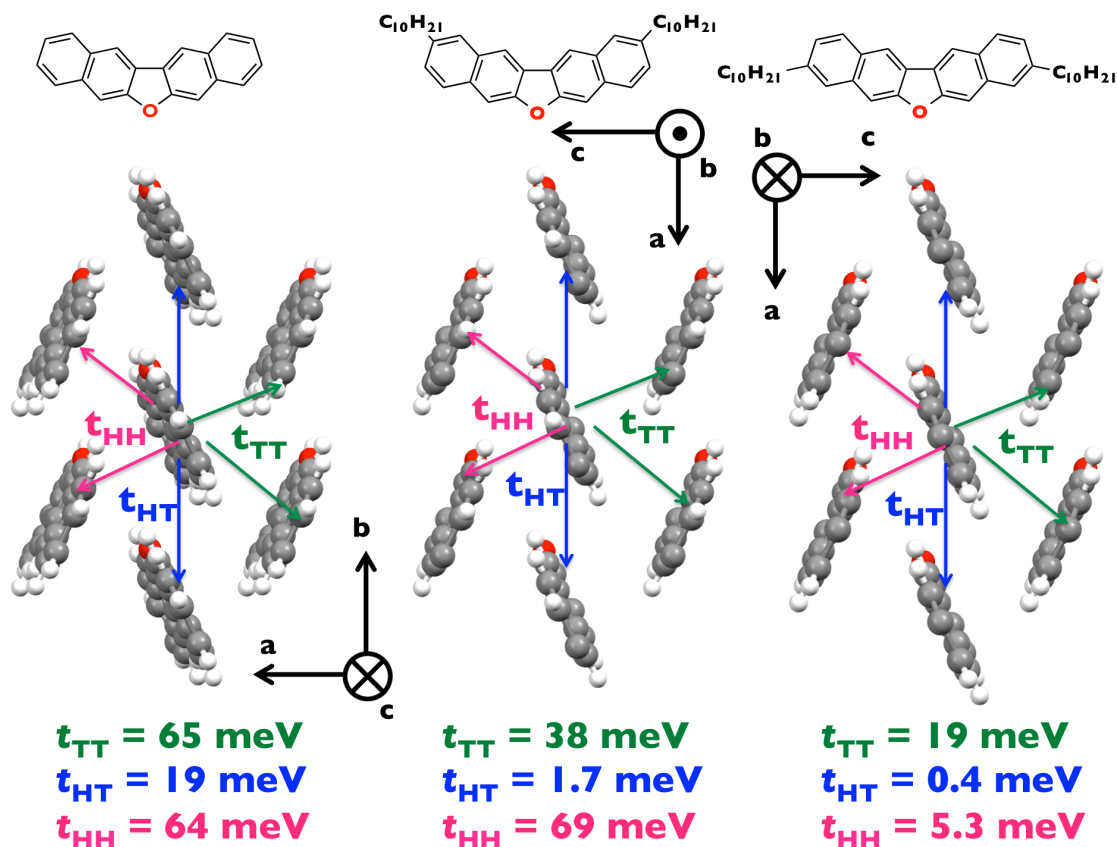
Figure 20. Packing structures and transfer integrals of **DNF−V**, **C$_{10}$−DNF−VV**, and **C$_{10}$−DNF−VW**.

In contrast, the W-shaped, furan-based compound, **DNF−W**, forms a one-dimensional π–π-stacked structure with anisotropic transfer integrals (*Figure 21*).[33] The difference between the aggregated structures of **DNF−V** derivatives and **DNF−W** might reflect the carrier transport properties in FETs. The device performances using these materials are discussed in Chapter 3.

t_b = 84 meV
t_{q1} = 13 meV
t_{q2} = 8 meV
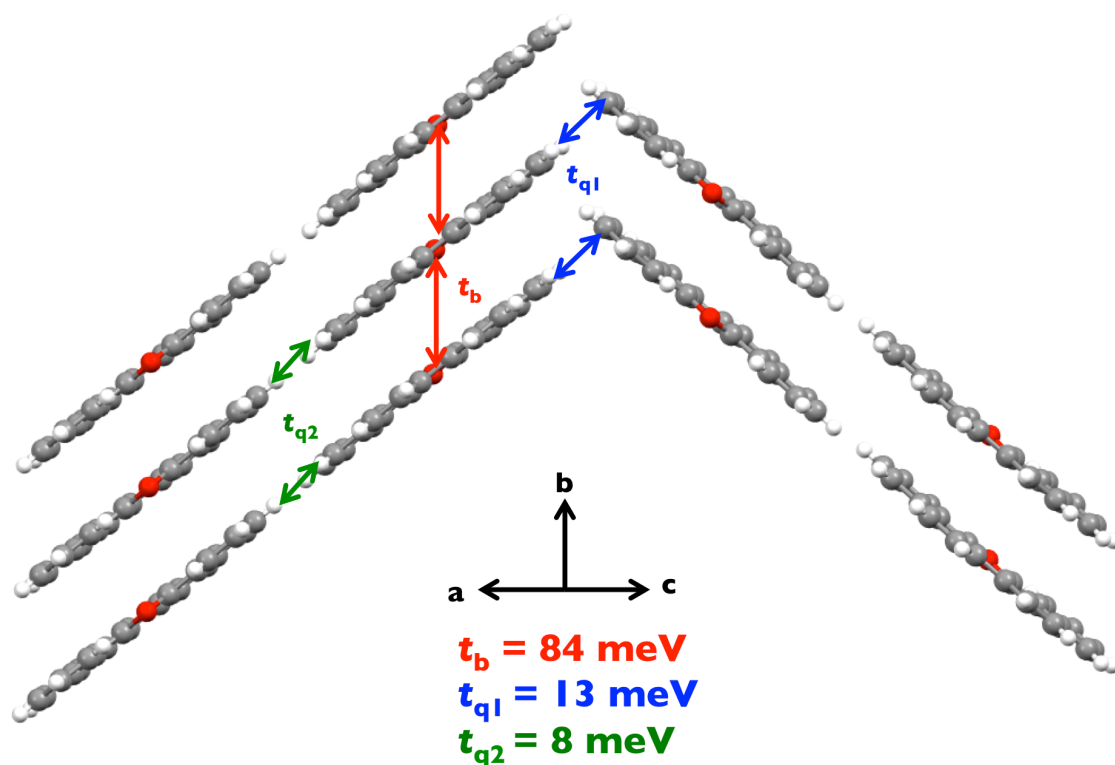
Figure 21. Packing structure and transfer integrals of **DNF–W**.

2.6 Phase-Transition Temperature

Phase-transition temperatures were measured using differential scanning calorimetry (DSC). As shown in *Figure 22*, the phase-transition temperature of C_{10}–**DNF–VV**, 176 °C, is higher than that of C_{10}–**DNF–VW** (128 °C). Notably, C_n–**DNT–VV** derivatives do not form liquid-crystalline phases, because rotational molecular motion is effectively suppressed by the banana-shaped π-core structure of C_n–**DNF–VV** and the molecular displacement is absent (*Figure 23*). In contrast, the sulfur-bridged counterparts (C_n–**DNT–VV**) transform into liquid-crystalline phases, since they assemble with large molecular displacements.

C_n–**DNF–VW** showed a liquid-crystalline state as a distinct feature during phase transition. This phenomenon might be due to differences in molecular rotation on heating. C_{10}–**DNF–VV** has a relatively bent molecular structure because of the presence of decyl groups at the 2,10-positions, therefore molecular rotation is inhibited. In contrast, because C_{10}–**DNF–VW** has a rod-like structure (*Figure 24*), the molecules rotate on heating, and a liquid-crystalline phase appears. Additionally, as the length of the alkyl chain shortens, the phase-transition temperatures shift to higher regions for

both **C$_n$–DNF–VW** and **C$_n$–DNF–VV** (*Figure 25* and *Figure 26*). This tendency results from the aspect ratio between the **DNF–V** core and the alkyl group length. In other words, the characteristics of the **DNF–V** core become dominant as the alkyl chain shortens.
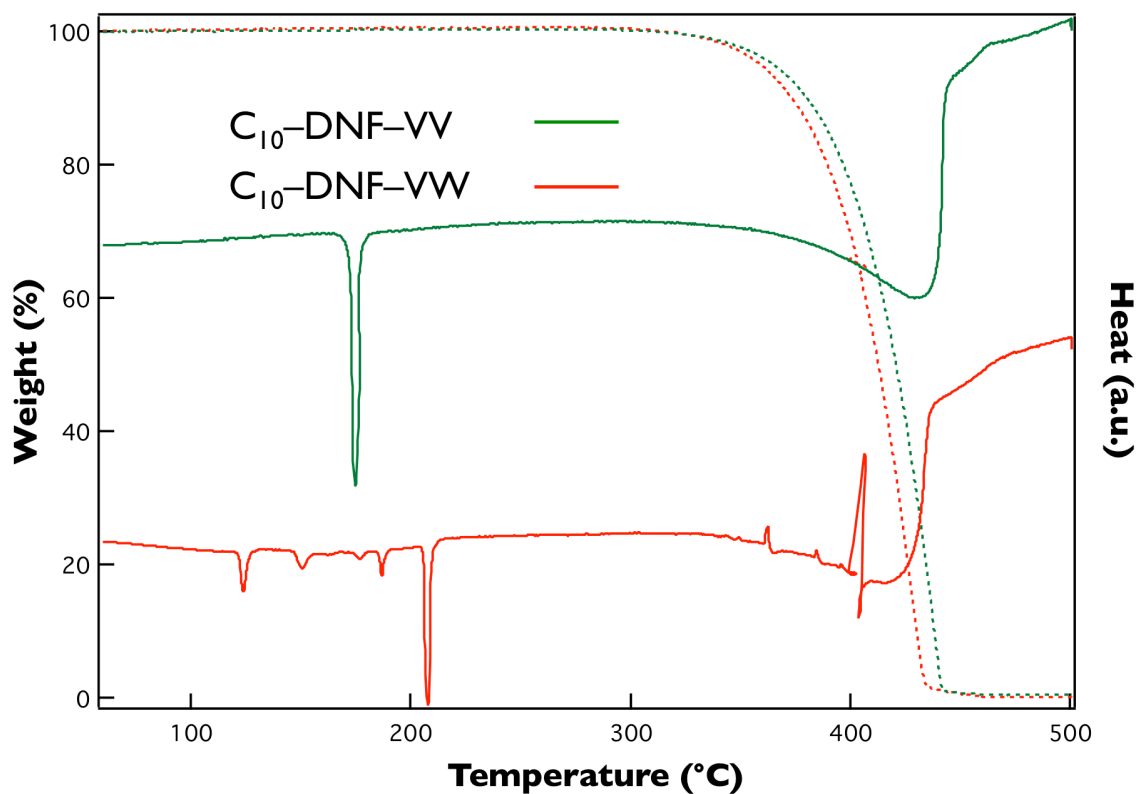

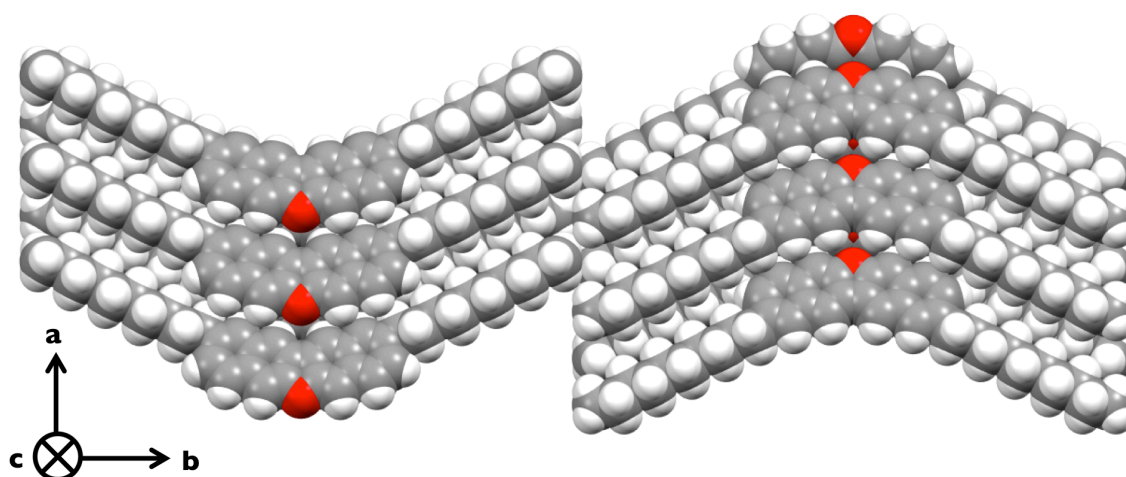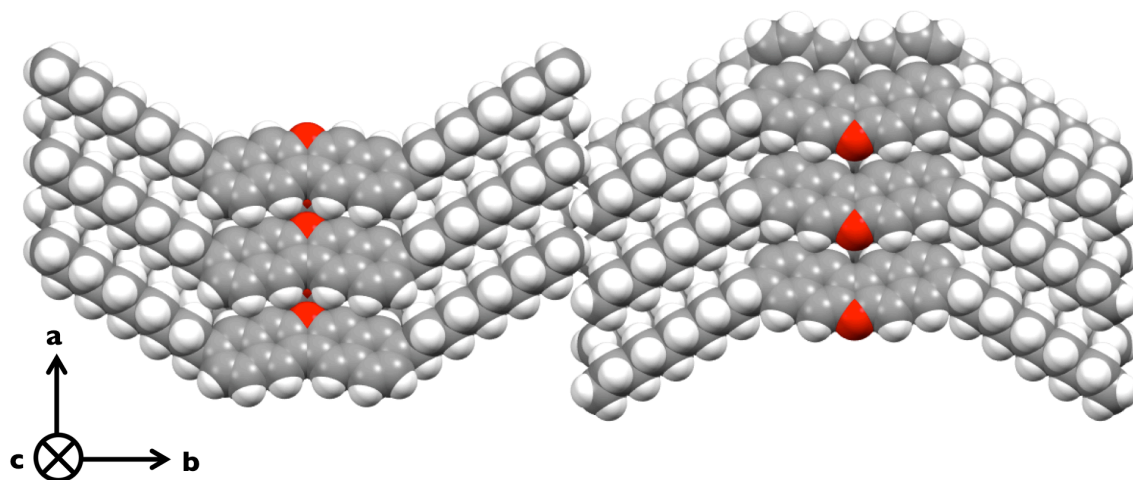*Figure 22.* DSC traces of **C$_{10}$–DNF–VV** (green line) and **C$_{10}$–DNF–VW** (red line).

Figure 23. Packing structure of **C$_{10}$–DNF–VV**.

Figure 24. Packing structure of **C₁₀–DNF–VW**.
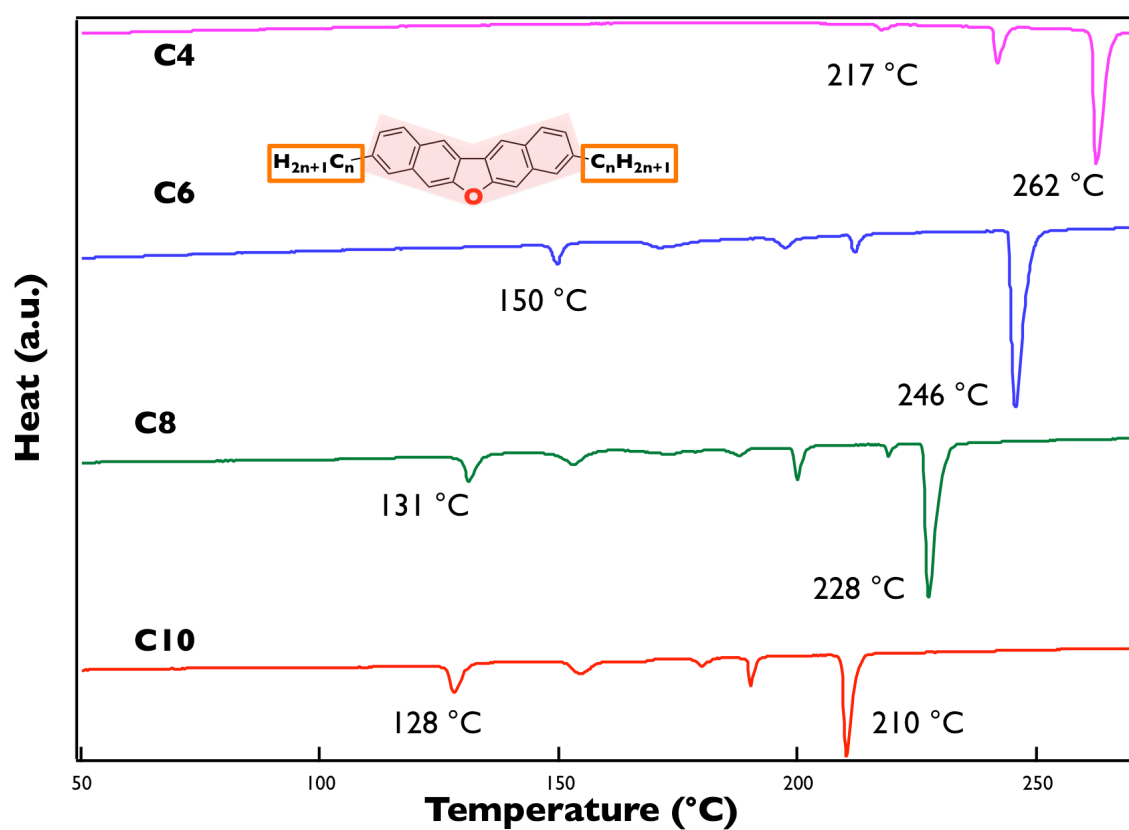
Figure 25. DSC traces of **Cₙ–DNF–VW**. Magenta line: **C₄–DNF–VW**, blue line: **C₆–DNF–VW**, green line: **C₈–DNF–VW**, and red line: **C₁₀–DNF–VW**.
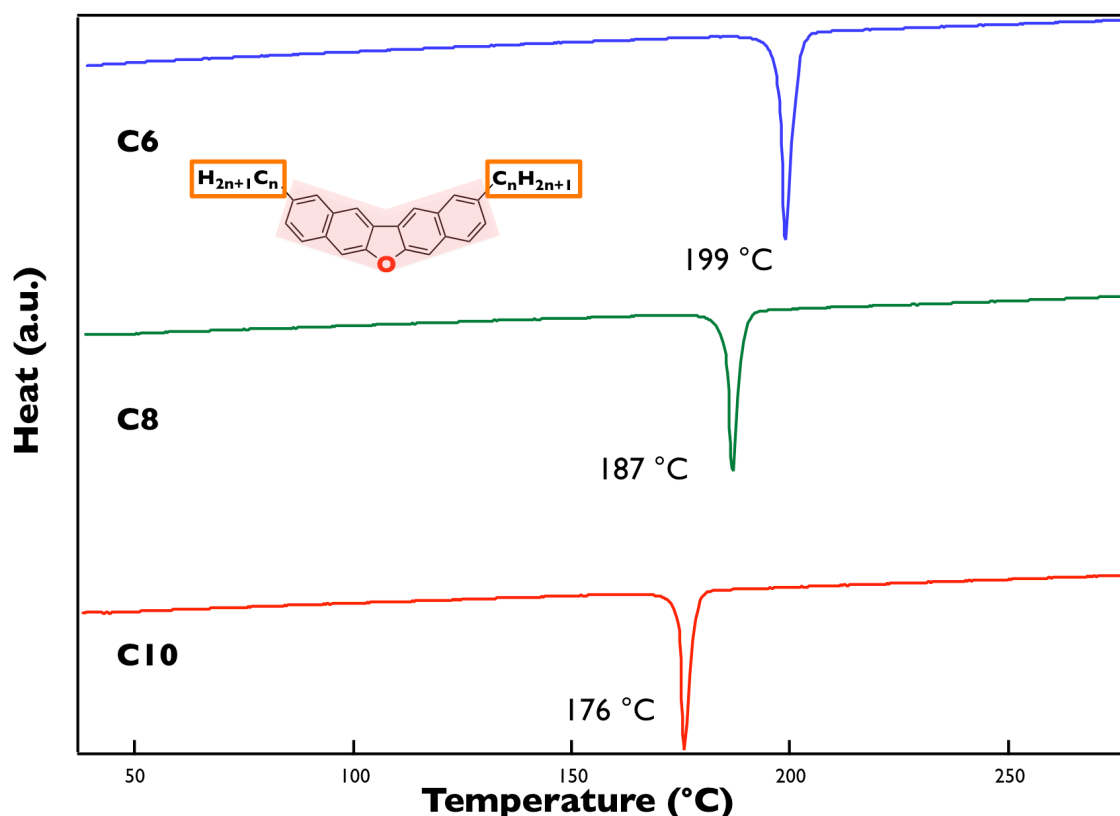
Figure 26. DSC traces of **C$_n$–DNF–VV**. Blue line: **C$_6$–DNF–VV**, green line: **C$_8$–DNF–VV**, and red line: **C$_{10}$–DNF–VV**.

2.7 Relationships between Molecular Structure and Optical Properties

To clarify the photophysical properties of the newly synthesized oxygen-bridged V-shaped compounds, absorption and emission spectroscopic measurements were performed. *Figure 27* shows the absorption spectra of **DNF–V** derivatives in 1,2-dichloroethane solutions. Red shifts were observed in the order **DNF–V**, **C$_{10}$–DNF–VW**, and **C$_{10}$–DNF–VV**. Each compound exhibited more red-shifted absorption characteristics in a thin film (*Figure 28*). The values are summarized in *Table 5*. The chemical stability of a thin film is an important factor for applications to organic electronic devices. The author measured the time-dependent UV-vis absorption spectrum of a vacuum-deposited thin film of **C$_6$–DNF–VW** as a representative material (*Figure 29*). This measurement verified the chemical stability of the **DNF–V** core in the solid state because the absorption spectrum did not change even after 1 week.
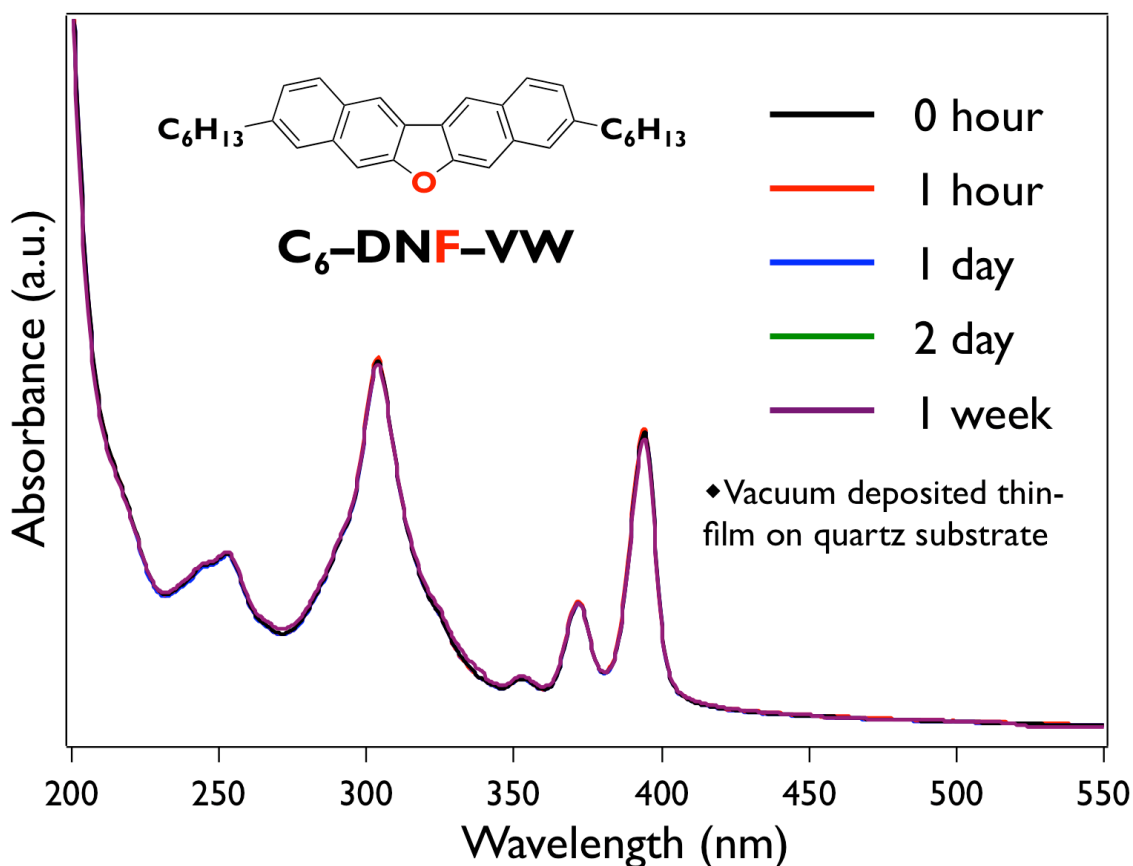
32
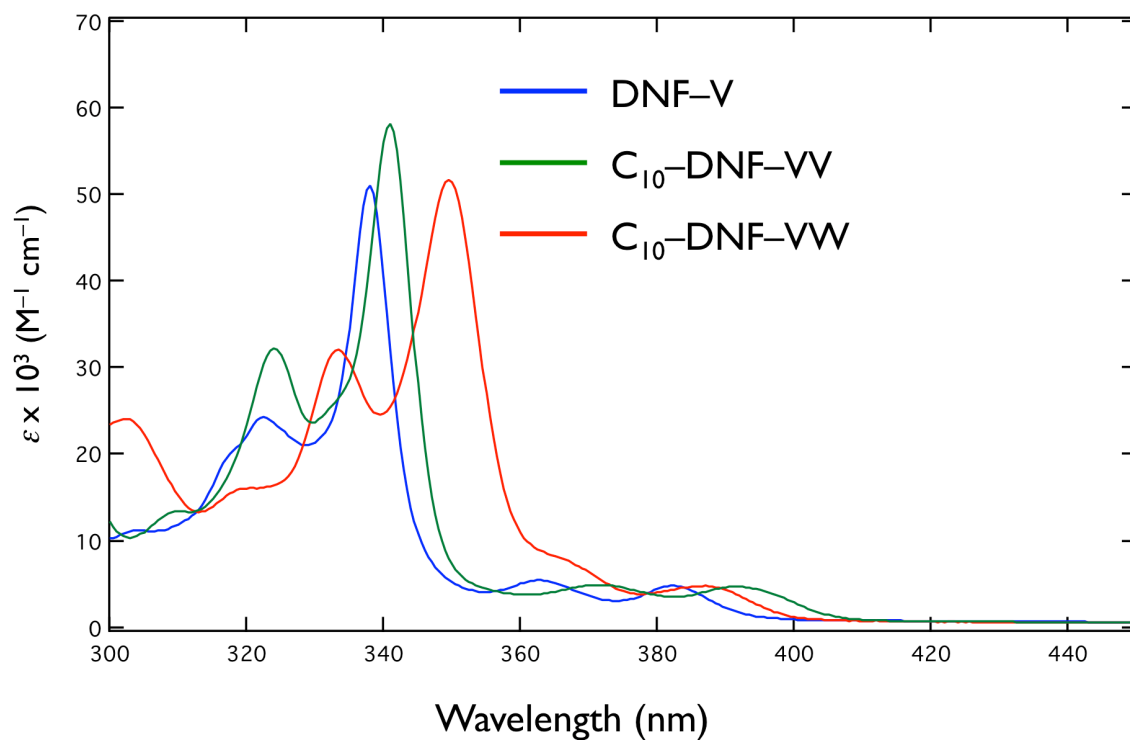
Figure 27. Absorption spectra of **DNF–V** (blue) **C$_{10}$–DNF–VV** (green), and **C$_{10}$–DNF–VW** (red) in 1,2-dichloroethane solutions (**DNF–V**: $C = 1.1 \times 10^{-5}$ M, **C$_{10}$–DNF–VV**: $C = 1.1 \times 10^{-5}$ M, and **C$_{10}$–DNF–VW**: $C = 5.7 \times 10^{-5}$ M).
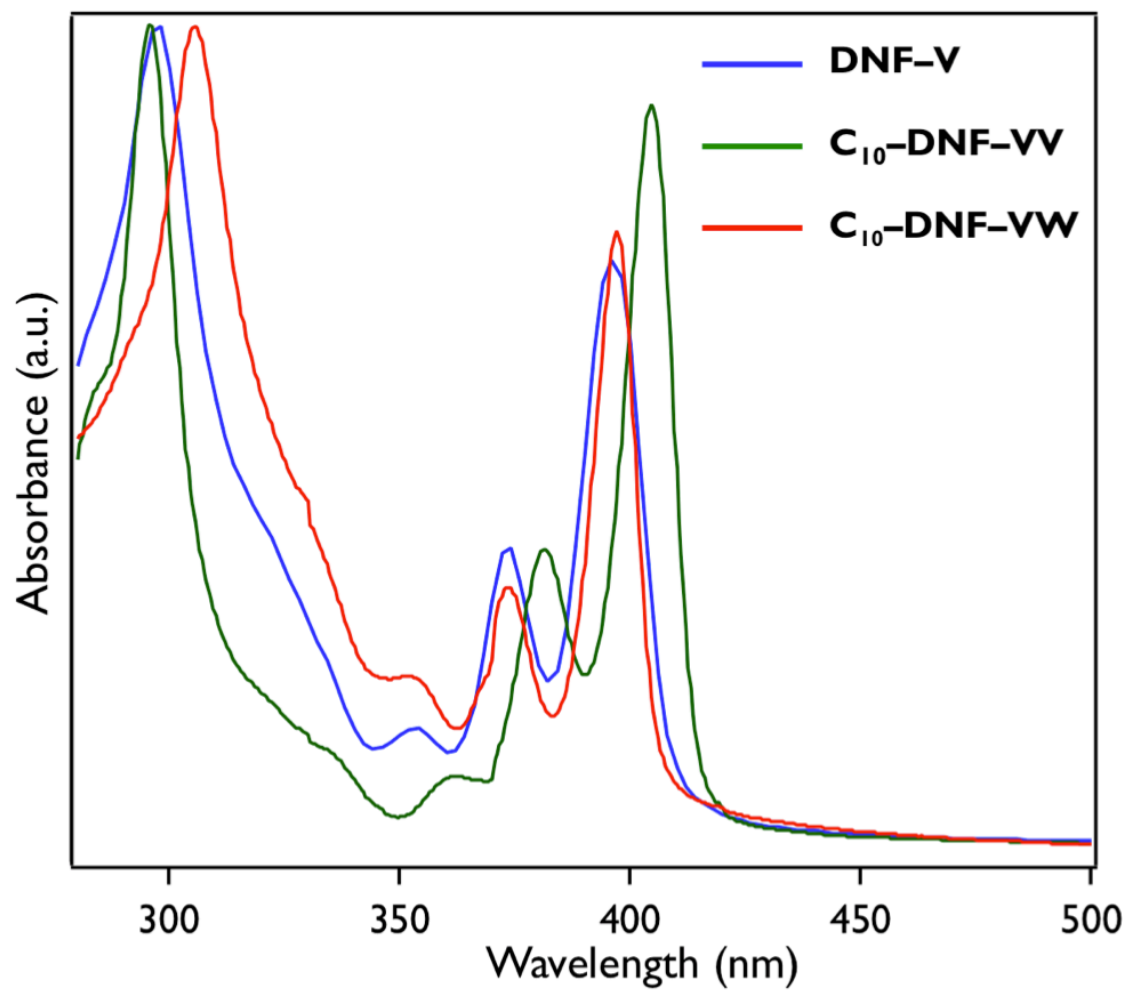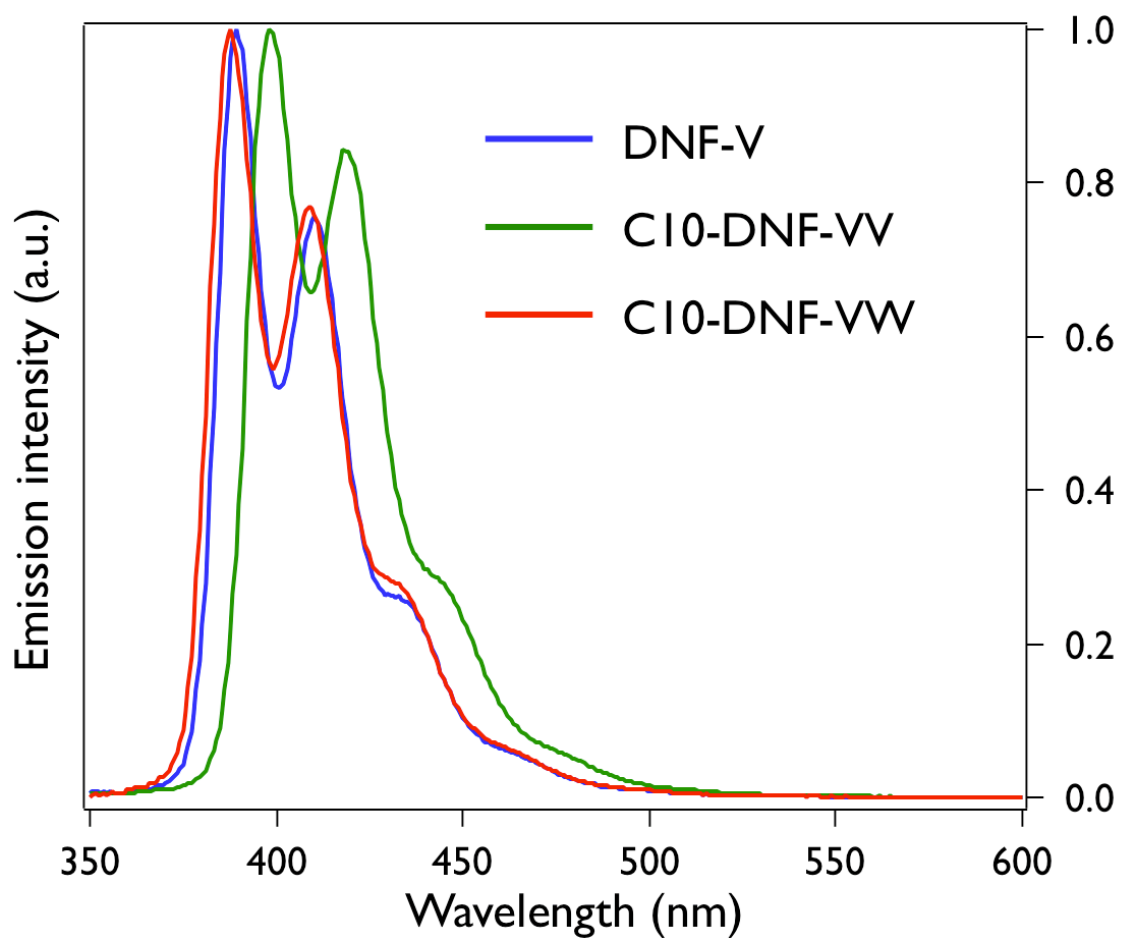
Figure 28. Absorption spectra of **DNF–V** derivatives (**DNF–V**: blue, **C$_{10}$–DNF–VV**: green, and **C$_{10}$–DNF–VW**: red) of vacuum-deposited thin films on quartz substrates.

Figure 29. Time-dependent UV-vis absorption spectra of **C₆–DNF–VW** vacuum-deposited thin film (nominal thickness: 100 nm) on quartz substrate under ambient conditions.

The author next measured the fluorescence spectra, quantum yields (Φ_f), and fluorescence lifetimes (τ) of the **DNF–V** derivatives. The **DNF–V** derivatives showed deep-blue emissions because of the large HOMO–LUMO gap, estimated from the absorption spectra (Figure 30). The fluorescence quantum yields of furan-containing organic semiconductors in 1,2-dichloroethane solutions were estimated to be around 80–90%, as summarized in *Table 6*. In contrast, differences among the fluorescence features were observed for these materials in the solid state (*Figure 31*). **DNF–W** and unsubstituted **DNF–V** exhibited very high Φ_f values of 60% and 72%, respectively, in the solid state, whereas the thiophene-containing π-conjugated material, **DNT–V**, showed a low Φ_f of 3%, mainly because of the strong spin–orbit coupling. In addition, the Φ_f of **DNF–V** decreased when alkyl chains were introduced into the π-core; among the alkyl-**DNF–V**s, **C₆–DNF–VW** and **C₁₀–DNF–VW** showed high Φ_f values of 51%

and 40%, respectively, in the solid state. To elucidate the origin of this trend, the author determined the τ values. As illustrated in *Figure 32*, these values were used to calculate the radiative relaxation (k_f) and non-radiative relaxation (k_{nr}) rate constants from the singlet excited states; the results are summarized in *Table 6*. Typically, the value of k_f is determined by the electronic state and that of k_{nr} is controlled by the surrounding environment. A comparison based on the substituent positions of the alkyl chains (*Figure 33*) shows that whereas the k_f values of **C$_n$–DNF–VW** and **C$_n$–DNF–VV** ($n = 6$, 10) are comparable to one another for all compounds (2.11–3.44 $\times$ 10^7 s^{-1}), the k_{nr} values of the more emissive **C$_n$–DNF–VW** (3.31 $\times$ 10^7 s^{-1} for **C$_6$** and 6.58 $\times$ 10^7 s^{-1} for **C$_{10}$**) are smaller than those of **C$_n$–DNF–VV** (10.3 $\times$ 10^7 s^{-1} for **C$_6$** and 13.9 $\times$ 10^7 s^{-1} for **C$_{10}$**). The smaller non-radiative rate constants of **C$_n$–DNF–VW** compared with those of **C$_n$–DNF–VV** might be due to the sizes of the distortion angles against the π-planes. The distortion angles of **C$_n$–DNF–VW** are smaller than those of **C$_n$–DNF–VV**, as shown in *Figure 15*. The higher planarity and rigidity of **C$_n$–DNF–VW** might therefore inhibit thermal deactivation without structural changes in the solid. The high Φ_f values of **C$_n$–DNF–VW** are therefore caused by suppression of non-radiative relaxation. (Notably, the exceptionally low non-radiative rate constant and high Φ_f of **C$_6$–DNF–VW** might be related to its chiral systems as shown in *Figure 34*.)

Figure 30. Fluorescence spectra of **DNF–V** derivatives (**DNF–V**: blue, **C$_{10}$–DNF–VV**: green, and **C$_{10}$–DNF–VW**: red) in 1,2-dichloroethane solutions.
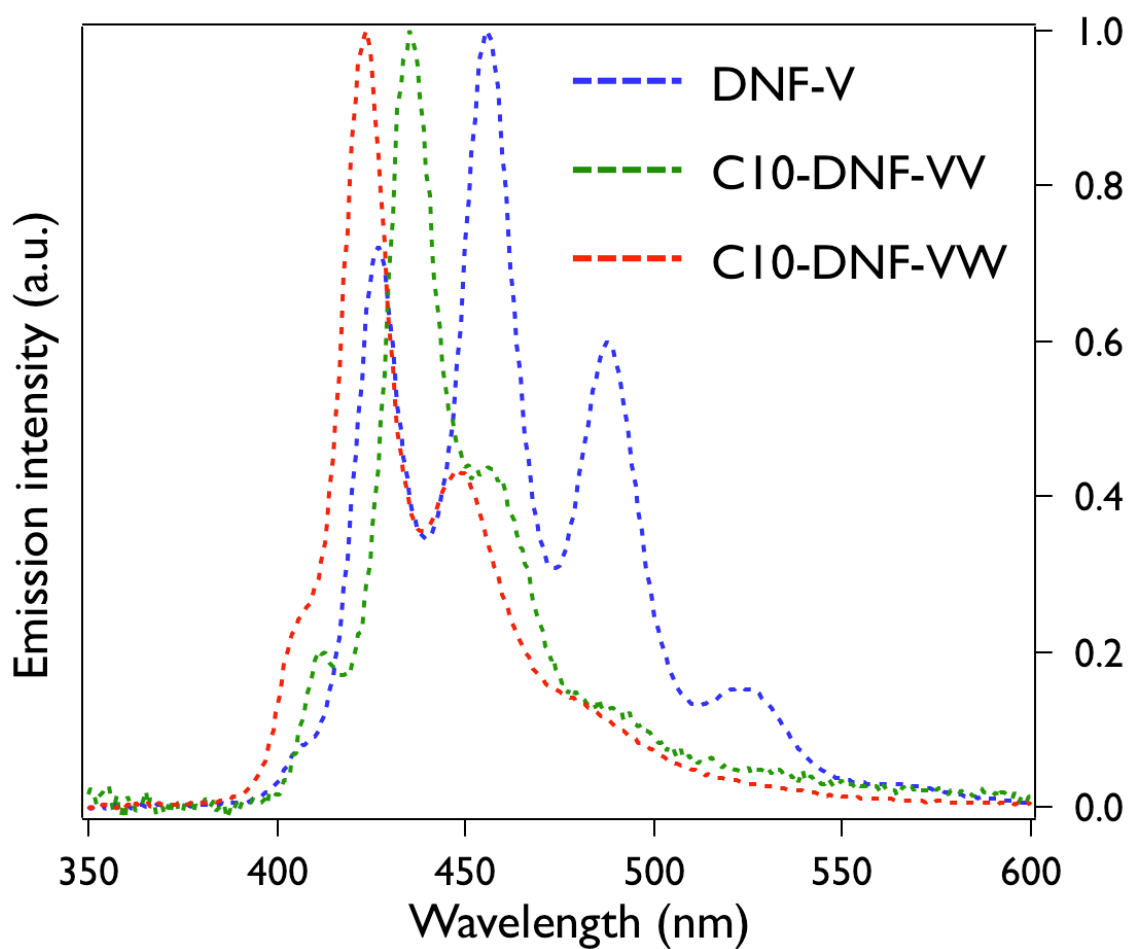
Figure 31. Fluorescence spectra of **DNF–V** (**DNF–V**: blue, C_{10}–**DNF–VV**: green, and C_{10}–**DNF–VW**: red) derivatives in solid state.

Table 5. Summary of optical properties of **DNF–V**, **C_{10}–DNF–VV**, and **C_{10}–DNF–VW**

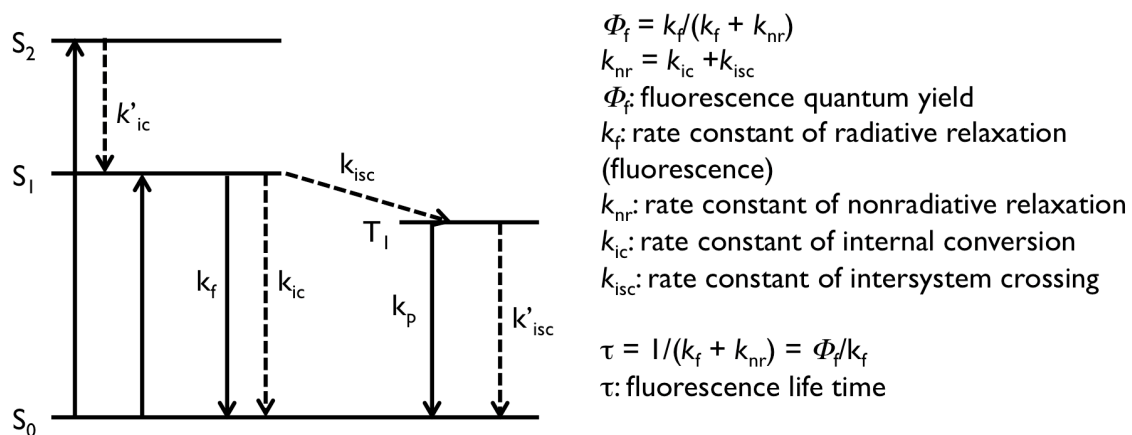| Compound	λ_{max}^{abs} (nm)[a]	λ_{max}^{em} (nm)[b]	λ_{max}^{em} (nm)[c]	ΔE (eV)[d]
DNF–V	322, 337, 362, 382	389, 410, 431 (sh)	408 (sh), 427, 455, 488, 524	3.14
C_{10}–DNF–VV	323, 340, 369, 389	398, 419, 444 (sh)	411, 435, 456 (sh)	3.04
C_{10}–DNF–VW	331, 348, 359 (sh), 381	388, 409, 431 (sh)	407 (sh), 424, 448	3.11

[a]Absorption spectra measured in 1,2-dichloroethane at room temperature; sh: shoulder. [b]Emission spectra excited at 340 nm measured in 1,2-dichloroethane at room temperature; sh: shoulder. [c]Emission spectra excited at 340 nm measured in solid state; sh: shoulder. [d]Determined from onset values of UV-vis absorptions in 1,2-dichloroethane.
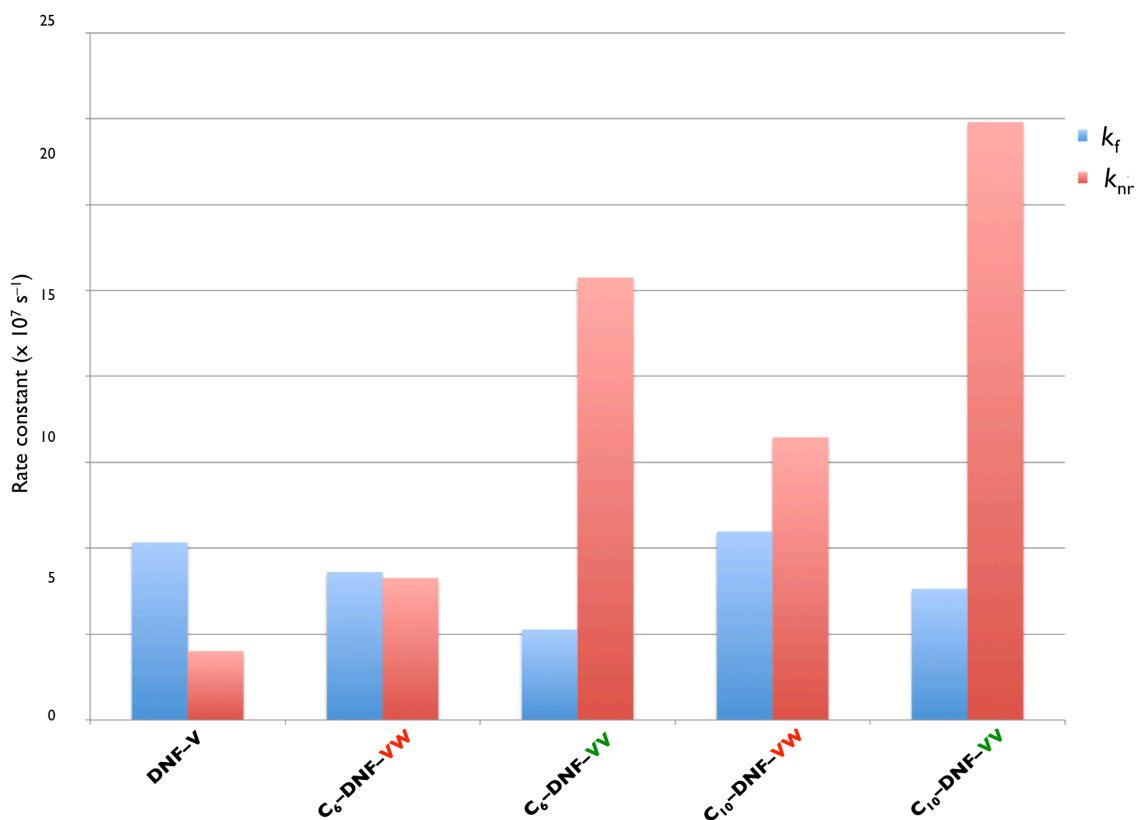
Table 6. Summary of fluorescence quantum yields, lifetimes, and photoluminescence rate constants of oxygen-bridged organic semiconductors

Compound.	Solution (in 1,2-dichloroethane)				Solid			
	Φ_f	τ (ns)	k_f ($\times 10^7$ s^{-1})[a]	k_{nr} ($\times 10^7$ s^{-1})[a]	Φ_f	τ (ns)	k_f ($\times 10^7$ s^{-1})[a]	k_{nr} ($\times 10^7$ s^{-1})[a]
DNF–V	0.83	23.084	3.60	0.74	0.72	17.415	4.13	1.61
C_4–DNF–VW	0.82	22.490	3.65	0.80	0.23	11.149	2.06	6.91
C_6–DNF–VW	0.89	22.340	3.98	0.49	0.51	14.815	3.44	3.31
C_8–DNF–VW	0.86	20.813	4.13	0.67	0.27	8.718	3.10	8.37
C_{10}–DNF–VW	0.83	22.683	3.66	0.75	0.40	9.112	4.39	6.58
C_6–DNF–VV	0.83	22.841	3.63	0.74	0.17	8.056	2.11	10.3
C_{10}–DNF–VV	0.87	22.619	3.85	0.58	0.18	5.890	3.06	13.9
DNF–W	–	–	–	–	0.60	5.666	10.60	7.06

[a]Radiative and non-radiative decay rate constants were calculated using Φ_f and τ, according to the formulas $k_f = \Phi_f/\tau$ and $k_{nr} = (1 - \Phi_f)/\tau$.

$\Phi_f = k_f/(k_f + k_{nr})$
$k_{nr} = k_{ic} + k_{isc}$
Φ_f: fluorescence quantum yield
k_f: rate constant of radiative relaxation (fluorescence)
k_{nr}: rate constant of nonradiative relaxation
k_{ic}: rate constant of internal conversion
k_{isc}: rate constant of intersystem crossing

$\tau = 1/(k_f + k_{nr}) = \Phi_f/k_f$
τ: fluorescence life time

Figure 32. Schematic diagram of photoluminescence mechanisms.

Figure 33. Comparison of radiative (k_f) and non-radiative (k_{nr}) decay rate constants of **DNF–V**, **C$_n$–DNF–VW**, and **C$_n$–DNF–VV** in solid state.
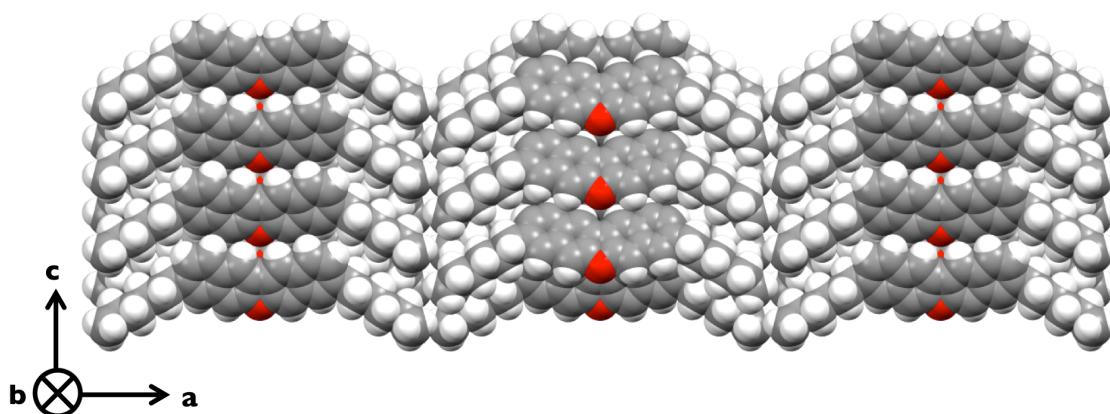
Figure 34. Molecular alignment along long axis in single crystal of **C₆–DNF–VW**.

2.8 Conclusion

In this chapter, the author developed a facile and efficient synthetic protocol for **DNF–V** derivatives using a zeolite catalyst. Each alkylated **DNF–V** derivative forms a herringbone packing structure, which is more favorable for efficient two-dimensional carrier transport then the one-dimensional π–π stacking structure of **DNF–W**. Furthermore, there was almost no molecular displacement in aggregated structures of **DNF–V** derivatives, indicating that all **the DNF–V** derivatives synthesized in this study might exhibit high FET performances, regardless of the positions of the alkyl groups. The dihedral angles between two naphthalene moieties in **C$_n$–DNF–VW** were smaller than those in **C$_n$–DNF–VV**. These small distortion angles against the π-cores might lead to high fluorescence quantum yields in the solid state. The results of this study of the fundamental properties, show the substituent-position effects on the solubility, phase transitions, and optical properties. **C₆–DNF–VW** and **C₁₀–DNF–VW**, in particular, exhibited high fluorescence quantum yields in the solid state. The rigid and planar π-cores of these two materials in the solid state suppressed non-radiative processes such as internal conversion and intercrossing systems compared with **C$_n$–DNF–VV**.

Experimental Section
Materials

<u>Reagents and Starting Materials</u>

Boron tribromide (1.0 M) in dichloromethane, 2-methoxy-6-bromonaphthalene, and NiCl$_2$(dppp) were purchased from TCI. All Grignard reagents, Fe(acac)$_3$, and trimethoxy(2-phenylethyl)silane were purchased from Sigma–Aldrich Inc. *N*-Methylpyrrolidone and 1,2-dichlorobenzene were purchased from Wako Pure Chemical Industries Ltd. *n*-BuLi (1.6 M) in hexane and all anhydrous solvents were purchased from Kanto chemicals. Zeolite HSZ-360 was purchased from the Tosoh Corp. 7-Methoxy-2-naphthyltrifluoromethanesulfonate[43] and 6-decyl-2-methoxynaphthalene[44] were prepared according to literature procedures.

Methods

<u>General Synthesis and Characterization Methods</u>

All the reactions were carried out under a N$_2$ atmosphere. Air- or moisture-sensitive liquids and solutions were transferred via a syringe or a Teflon cannula. Analytical thin-layer chromatography (TLC) was performed on glass plates with 0.25 mm 230–400 mesh silica gel containing a fluorescent indicator (Merck Silica gel 60 F254). TLC plates were visualized by exposure to a UV lamp (254 nm and 365 nm) and by dipping in 10% phosphomolybdic acid in ethanol and heating on a hot plate. Flash column chromatography was performed on Kanto silica gel 60. Open-column chromatography was performed on Wakogel C-200 (75–150 μm). All NMR spectra were recorded using JEOL ECA600 and JEOL ECS400 spectrometers. Chemical shifts are reported in parts per million (ppm, δ scale) from residual protons in deuterated solvents for ^{1}H NMR (δ 7.26 ppm for chloroform and δ 5.93 ppm for 1,1,2,2-tetrachloroethane) and from the solvent carbon for ^{13}C NMR (δ 77.16 ppm for chloroform and δ 74.00 ppm for 1,1,2,2-tetrachloroethane). The data are presented in the following format: chemical shift, multiplicity (s = singlet, d = doublet, t = triplet, m = multiplet), coupling constant in hertz (Hz), signal area integration in natural numbers, and assignment (*italic*). Mass spectra were measured using a JEOL JMS-T100LC APCI/ESI mass spectrometer. Melting points and elemental analyses were performed using a Mettler Toledo MP70 melting point system and J-Science Lab JM10 MICRO CORDER, respectively.

Photoelectron yield spectroscopy (PYS) was performed using a Sumitomo Heavy Industries Advanced Machinery PYS-202 instrument. For PYS measurements, thin films (100 nm) were thermally evaporated on ITO-coated quartz substrates and measurements were performed in a vacuum. TG–DTA measurements were carried out using a Rigaku Thermo Plus EVO II TG 8120 instrument. The sample was placed in an aluminum pan and heated at a rate of 5 K min^{-1}, under N_2 purging at a flow rate of 100 mL min^{-1}. Al_2O_3 was used as a reference material. DSC was performed using a Rigaku Thermo Plus EVO II DSC8270 instrument. The sample was placed in an aluminum pan and heated at a rate of 5 K min^{-1}, under N_2 purging at a flow rate of 100 mL min^{-1}. Al_2O_3 was used as a reference material. UV-vis absorption spectra were obtained using a JASCO V-570 spectrometer. Thin films of thickness 100 nm were prepared by vacuum deposition on quartz substrates. The sample solutions were prepared using degassed, analytical-grade 1,2-dichloroethane. Photoluminescence spectra and absolute quantum yields were recorded using a Hamamatsu Photonics C9920–02 Absolute PL Quantum Yield system. The sample solutions were prepared in degassed, analytical-grade 1,2-dichloroethane. Fluorescence lifetimes were evaluated using a Hamamatsu Photonics Quantaurus-Tau C11367-01 system.

General procedure for iron-catalyzed alkylation[45]
2-Decyl-7-methoxynaphthalene
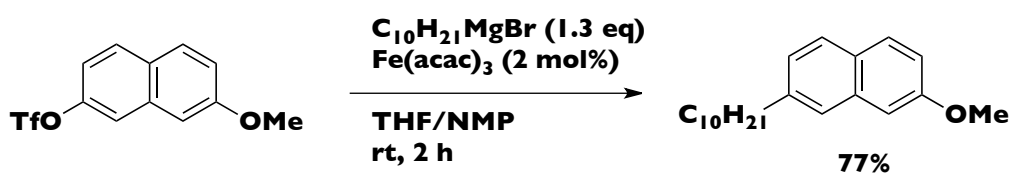
Decylmagnesium bromide (1.0 M in Et_2O, 96.7 mL, 96.7 mmmol, 1.3 mol amt.) was added dropwise to a solution of 7-methoxy-2-naphthyltrifluoromethanesulfonate (22.8 g, 74.4 mmol) and Fe(acac)$_3$ (525 mg, 1.49 mmol, 2 mol%) in THF (330 mL) and N-methylpyrrolidone (33 mL) at room temperature. The color immediately changed to dark brown, and the reaction was exothermic. After stirring for 2 h at ambient temperature, the reaction was quenched with water. The organic layer was extracted with EtOAc and washed with water and brine. After removal of the combined solvent
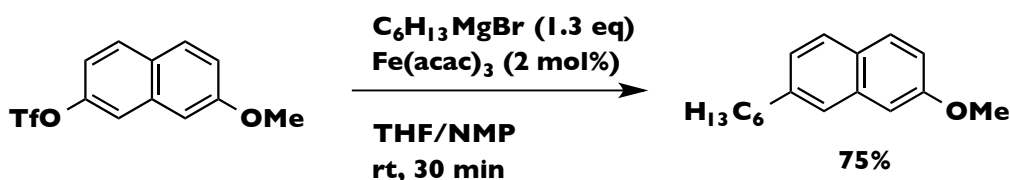
from the organic layer in vacuo, the crude material was purified by silica gel column chromatography (hexane:chloroform = 97:3) to afford the title compound (17.0 g, 57.0 mmol, 77%) as a white solid. The spectroscopic data were identical to those previously reported in the literature.[2]

2-Butyl-7-methoxynaphthalene
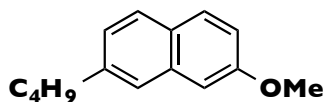
Colorless oil. Yield 77%. ^{1}H NMR (600 MHz, CDCl$_3$): δ 0.98 (t, J = 7.8 Hz, 3H, CH_3), 1.42 (sext, J = 7.8 Hz, 4H, CH_2CH$_3$), 1.71 (quin, J = 7.8 Hz, 2H, ArCH$_2$CH_2), 2.75 (t, J = 7.8 Hz, 2H, ArCH_2), 3.94 (s, 3H, OCH_3), 7.08 (d, J = 8.4 Hz, 1H, ArH), 7.09 (s, 1H, ArH), 7.20 (d, J = 8.4 Hz, 1H, ArH), 7.53 (s, 1H, ArH), 7.67–7.71 (m, 2H, ArH). ^{13}C NMR (150 MHz, CDCl$_3$): δ 14.1, 22.7, 29.3, 29.4, 29.5, 31.4, 31.9, 36.2, 55.2, 105.4, 117.7, 125.2, 125.3, 127.4 (two carbons), 129.1, 134.7, 141.1, 157.6. TOF HRMS (APCI): Calcd for C$_{15}$H$_{19}$O [M+H] 215.1436, found 215.1428.

2-Hexyl-7-methoxynaphthalene

Hexylmagnesium bromide (2.0 M in Et$_2$O, 31.8 mL, 63.7 mL) was added dropwise to a red solution of 7-methoxy-2-naphthyltrifluoromethanesulfonate (15.0 g, 49.0 mmol) and Fe(acac)$_3$ (346 mg, 0.98 mmol, 2 mol%) in THF (245 mL) and N-methylpyrrolidone (25 mL) at room temperature. The color changed immediately to dark brown. The resulting mixture was stirred for 30 min, and the reaction was then quenched with water. The organic layer was extracted with EtOAc, washed with water and brine, and the solvent was removed in vacuo. The crude material was purified by silica gel column chromatography (hexane:chloroform = 90:10) to afford the title compound (8.87 g, 36.6 mmol, 75%) as a white solid. M.p.: 37.3–38.0 °C. ^{1}H NMR (400 MHz, CDCl$_3$): δ 0.88 (t, J = 6.8 Hz, 3H, CH_3), 1.39–1.30 (m, 6H, (CH_2)$_3$), 1.69 (quin, J = 6.8 Hz, 2H, ArCH$_2$CH_2), 2.73 (t, J = 7.6 Hz, 2H, ArCH_2CH$_2$), 3.91 (s, 3H,

OC*H₃*), 7.12–7.11 (m, 2H, Ar*H*), 7.30 (d, *J* = 8.4 Hz, 1H, Ar*H*), 7.54 (s, 1H, Ar*H*), 7.68–7.65 (m, 2H, Ar*H*). ^{13}C NMR (150 MHz, CDCl₃): δ 14.3, 22.8, 29.2, 31.5, 31.9, 36.3, 55.4, 105.6, 117.9, 125.3, 125.4, 127.5, 127.6, 129.2, 134.9, 141.2, 157.8. TOF HRMS (APCI): Calcd for C₁₇H₂₃O [M+H] 243.1749, found 243.1746.

2-Octyl-7-methoxynaphthalene
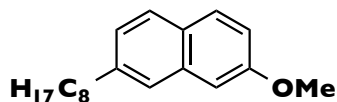
White solid. Yield 78%. M.p.: 39.4–40.9 °C. ^{1}H NMR (600 MHz, CDCl₃): δ 0.89 (t, *J* = 7.8 Hz, 3H, C*H₃*), 1.25–1.38 (m, 10H, (C*H₂*)₅), 1.70 (quin, *J* = 7.2 Hz, 2H, ArCH₂C*H₂*), 2.74 (t, *J* = 7.2 Hz, 2H, ArC*H₂*CH₂), 3.92 (s, 3H, OC*H₃*), 7.07 (d, *J* = 8.4 Hz, 1H, Ar*H*), 7.08 (s, 1H, Ar*H*), 7.18 (d, *J* = 8.4 Hz, 1H, Ar*H*), 7.51 (s, 1H, Ar*H*), 7.67–7.70 (m, 2H, Ar*H*). ^{13}C NMR (150 MHz, CDCl₃): δ 14.1, 22.7, 29.3, 29.4, 29.5, 31.4, 31.9, 36.2, 55.2, 105.4, 117.7, 125.2, 125.3, 127.4 (two carbons), 129.1, 134.7, 141.1, 157.6. TOF HRMS (APCI): Calcd for C₁₉H₂₇O [M+H] 271.2062, found 271.2058.

**General procedure for alkylation via Kumada–Tamao cross coupling of 2-hexyl-6-methoxynaphyhalene**
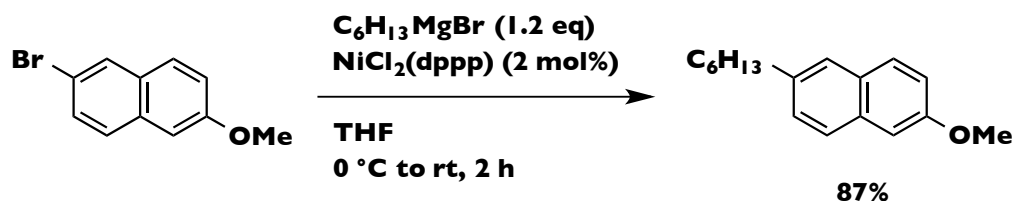
Hexylmagnesium bromide (2.0 M in Et₂O, 60 mL, 120 mmol) was added dropwise to a solution of 2-methoxy-6-bromonaphthalene (21.71 g, 100 mmol) and NiCl₂(dppp) (1.08 mg, 2 mmol) in THF (100 mL) at 0 °C. The color changed immediately to dark brown. After the addition, the green-colored reaction mixture was warmed to room temperature and stirred for 2 h. The reaction was quenched by filtration with a silica pad. The crude material was then purified by silica gel column chromatography (hexane:chloroform = 90:10) to afford the title compound (21.03 g, 86.7 mmol, 87%) as a white solid. M.p.: 54.0–55.0 °C. ^{1}H NMR (600 MHz, CDCl₃): δ 0.88 (t, *J* = 6.8 Hz, 3H, C*H₃*), 1.36–1.25 (m, 6H, (C*H₂*)₃), 1.69 (quin, *J* = 6.8 Hz, 2H, ArCH₂C*H₂*), 2.74 (t, *J* = 7.6 Hz, 2H, ArC*H₂*CH₂), 3.91 (s, 3H, OC*H₃*), 7.06–7.08 (m, 2H, Ar*H*), 7.18 (d, *J* = 8.4 Hz, 1H,

ArH), 7.51 (s, 1H, ArH), 7.67–7.70 (m, 2H, ArH). ^{13}C NMR (150 MHz, CDCl$_3$): δ 14.2, 22.8, 29.2, 31.6, 31.9, 36.1, 55.4, 105.7, 118.7, 126.3, 125.7, 128.1, 129.0, 129.2, 133.0, 138.3 157.2 TOF HRMS (APCI): Calcd for C$_{17}$H$_{23}$O [M+H] 243.1749, found 243.1740.
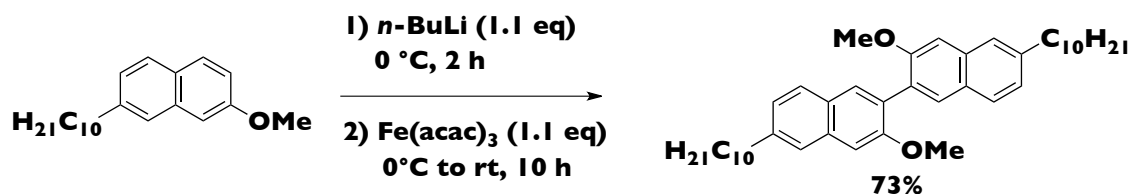
2-Octyl-6-methoxynaphthalene
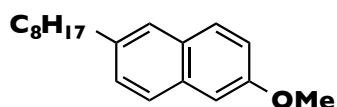
White solid. Yield 56%. M.p.: 52.7–54.0 °C. ^{1}H NMR (400 MHz, CDCl$_3$): δ 0.88 (t, J = 7.2 Hz, 3H, CH$_3$), 1.25–1.43 (m, 18H, (CH$_2$)$_9$), 1.69 (quin, J = 7.6 Hz, 2H, ArCH$_2$CH$_2$), 2.74 (t, J = 7.6 Hz, 2H, ArCH$_2$CH$_2$), 3.91 (s, 3H, OCH$_3$), 7.07 (d, J = 8.4 Hz, 1H, ArH), 7.08 (s, 1H, ArH), 7.18 (d, J = 8.0 Hz, 1H, ArH), 7.51 (s, 1H, ArH), 7.66–7.70 (m, 2H, ArH). ^{13}C NMR (150 MHz, CDCl$_3$): δ 14.2, 22.8, 29.4, 29.5, 29.7, 29.8, 31.6, 32.0, 36.1, 55.4, 105.7, 118.7, 126.2, 126.7, 128.1, 129.0, 129.2, 133.0, 138.3, 157.2. TOF HRMS (APCI): Calcd for C$_{23}$H$_{35}$O [M+H] 271.2062, found 271.2051.

## General procedure for homocoupling reaction
6,6'-Didecyl-3,3'-dimethoxy-2,2'-binaphthalene (for synthesis of C$_{10}$–DNF–VW)

n-BuLi in hexane (1.62 M, 17.0 mL, 27.5 mmol, 1.1 mol amt.) was added to a solution of 7-decyl-2-methoxynaphthalene (7.46 g, 25.0 mmol) in THF (100 mL) at 0 °C. After stirring at 0 °C for 2 h, Fe(acac)$_3$ (9.71 g, 27.5 mmol, 1.1 mol amt.) was added at 0 °C and the resultant mixture was stirred at room temperature for 10 h. After the reaction was complete, the crude material was passed through a short pad of Celite to remove the inorganic salt. After removing the solvent in vacuo, the crude material was purified by silica gel column chromatography (hexane:chloroform = 90:10) to afford the title compound (5.43 g, 9.13 mmol, 73%) as a white solid. M.p.: 68.4–71.5 °C. ^{1}H NMR (400 MHz, CDCl$_3$): δ 0.89 (t, J = 6.8 Hz, 6H, CH$_3$), 1.26–1.40 (m, 28H, (CH$_2$)$_7$), 1.70 (quin, J = 7.2 Hz, 4H, ArCH$_2$CH$_2$), 2.76 (t, J = 7.2 Hz, 4H, ArCH$_2$), 3.86 (s, 6H, OCH$_3$), 7.16 (s, 2H, ArH), 7.19 (d, J = 8.4 Hz, 2H, ArH), 7.56 (s, 2H, ArH), 7.68–7.71 (m, 4H,
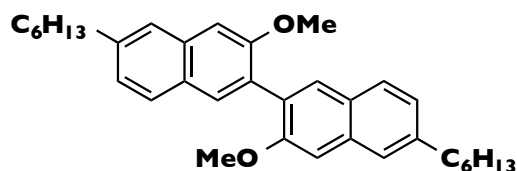
Ar*H*). ^{13}C NMR (150 MHz, CDCl$_3$): δ 14.3, 22.9, 29.2 (two carbons), 29.75, 29.82 (two carbons), 31.6, 32.1, 36.4, 55.8, 105.1, 125.2, 125.4, 127.2, 127.6, 129.2, 130.1, 134.6, 141.0, 156.5. TOF HRMS (APCI): Calcd for C$_{42}$H$_{59}$O$_2$ [M+H] 595.4515, found 595.4537. Anal. Calcd for C$_{42}$H$_{58}$O$_2$: C, 84.79; H, 9.83. Found: C, 84.85; H, 9.72.

6,6'-Dibutyl-3,3'-dimethoxy-2,2'-binaphthalene
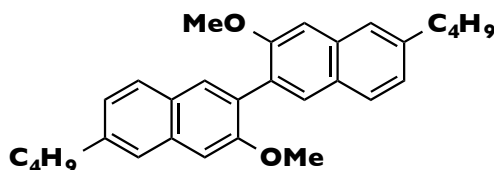
White solid. Yield: 67%. M.p.: 102.4–103.2 °C. ^{1}H NMR (500 MHz, CDCl$_3$): δ 0.96 (t, *J* = 7.2 Hz, 6H, C*H$_3$*), 1.40 (sext, *J* = 7.2 Hz, 4H, C*H$_2$*CH$_3$), 1.70 (quin, *J* = 7.2 Hz, 4H, ArCH$_2$C*H$_2$*), 2.77 (t, *J* = 8.3 Hz, 4H, Ar*CH$_2$*), 3.85 (s, 6H, OC*H$_3$*), 7.16 (s, 2H, Ar*H*), 7.19 (d, *J* = 8.3 Hz, 2H, Ar*H*), 7.56 (s, 2H, Ar*H*), 7.68–7.71 (m, 4H, Ar*H*). ^{13}C NMR (125 MHz, CDCl$_3$): δ 14.0, 22.4, 33.6, 35.9, 55.7, 105.0, 125.1, 125.3, 127.2, 127.5, 129.1, 130.0, 134.5, 140.8, 156.4. TOF HRMS (APCI): Calcd for C$_{30}$H$_{35}$O$_2$ [M+H] 427.2637, found 427.2633.

6,6'-Dihexyl-3,3'-dimethoxy-2,2'-binaphthalene

White solid. Yield: 73%. M.p.: 102.0–102.6 °C. ^{1}H NMR (600 MHz, CDCl$_3$): δ 0.89 (t, *J* = 7.2 Hz, 6H, C*H$_3$*), 1.30–1.38 (m, 12H, (C*H$_2$*)$_3$), 1.70 (quin, *J* = 7.8 Hz, 4H, ArCH$_2$C*H$_2$*), 2.76 (t, *J* = 7.8 Hz, 4H, Ar*CH$_2$*), 3.86 (s, 6H, OC*H$_3$*), 7.16 (s, 2H, Ar*H*), 7.19 (d, *J* = 7.8 Hz, 2H, Ar*H*), 7.56 (s, 2H, Ar*H*), 7.68–7.71 (m, 4H, Ar*H*). ^{13}C NMR (150 MHz, CDCl$_3$): δ 14.3, 22.8, 29.2, 31.6, 32.0, 36.4, 55.8, 105.1, 125.2, 125.4, 127.2, 127.6, 129.2, 130.1, 134.6, 141.0, 156.5. TOF HRMS (APCI): Calcd for C$_{34}$H$_{43}$O$_2$ [M+H] 483.3263, found 483.3255.

6,6'-Dioctyl-3,3'-dimethoxy-2,2'-binaphthalene
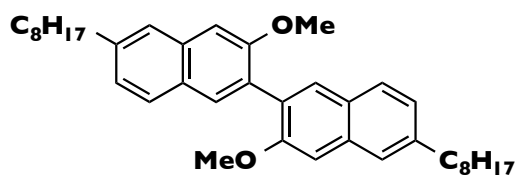
White solid. Yield: 57%. M.p.: 80.6–82.6 °C. ^{1}H NMR (600 MHz, CD$_3$Cl): δ 0.89 (t, J = 7.2 Hz, 6H, CH_3), 1.28–1.36 (m, 20H, (CH_2)$_5$), 1.71 (quin, J = 7.2 Hz, 4H, ArCH$_2$CH_2), 2.76 (t, J = 7.2 Hz, 4H, ArCH_2), 3.86 (s, 6H, OCH_3), 7.16 (s, 2H, ArH), 7.19 (d, J = 8.4 Hz, 2H, ArH), 7.56 (s, 2H, ArH), 7.68–7.71 (m, 4H, ArH). ^{13}C NMR (150 MHz, CDCl$_3$): δ 14.3, 22.8, 29.4, 29.5, 29.7, 31.6, 32.1, 36.3, 55.8, 105.125.2, 125.4, 127.3, 127.7, 129.2, 130.1, 134.6, 141.0, 156.5. TOF HRMS (APCI): Calcd for C$_{38}$H$_{51}$O$_2$ [M+H] 539.3889, found 539.3881.

7,7'-Didecyl-3,3'-dimethoxy-2,2'-binaphthalene (for synthesis of **C$_{10}$–DNF–VV**)
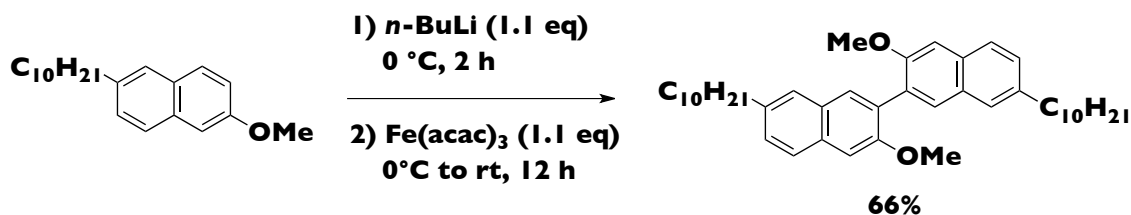
White solid. Yield: 66%. M.p.: 65.4–66.4 °C. ^{1}H NMR (400 MHz, CDCl$_3$): δ 0.88 (t, J = 6.8 Hz, 6H, CH$_3$), 1.26–1.35 (m, 28H, (CH_2)$_7$), 1.69 (quin, J = 7.6 Hz, 4H, ArCH$_2$CH_2), 2.74 (t, J = 7.6 Hz, 4H, ArCH_2), 3.86 (s, 6H, OCH_3), 7.19 (s, 2H, ArH), 7.30 (d, J = 8.4 Hz, 2H, ArH), 7.55 (s, 2H, ArH), 7.68 (s, 2H, ArH), 7.70 (d, J = 8.4 Hz, 2H, ArH). ^{13}C NMR (150 MHz, CDCl$_3$): δ 14.3, 22.9, 29.48, 29.51, 29.7, 29.80 (two carbons), 31.7, 32.1, 36.1, 55.8, 105.3, 126.3, 126.4, 127.9, 129.0, 129.9, 130.1, 132.8, 138.3, 155.9. TOF HRMS (APCI): Calcd for C$_{42}$H$_{59}$O$_2$ [M+H] 595.4515, found 595.4509. Anal. Calcd for C$_{42}$H$_{58}$O$_2$: C, 84.79; H, 9.83. Found: C, 84.73; H, 9.56.

7,7'-Dihexyl-3,3'-dimethoxy-2,2'-binaphthalene
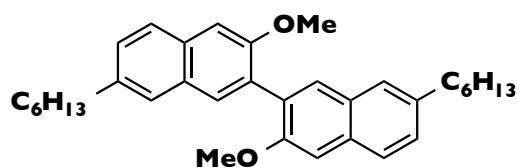
White solid. Yield: 61%. ^{1}H NMR (600 MHz, CDCl$_3$): δ 0.90 (t, J = 7.2 Hz, 6H, CH_3), 1.32–1.37 (m, 12H, (CH_2)$_3$), 1.69 (quin, J = 7.2 Hz, 4H, ArCH$_2$CH_2), 2.75 (t, J = 7.2 Hz, 4H, ArCH_2), 3.87 (s, 6H, OCH_3), 7.20 (s, 2H, ArH), 7.32 (d, J = 8.4 Hz, 2H, ArH), 7.56 (s, 2H, ArH), 7.69 (s, 2H, ArH), 7.72 (d, J = 8.4 Hz, 2H, ArH). ^{13}C NMR (150 MHz, CDCl$_3$): δ 14.3, 22.8, 29.2, 31.6, 32.0, 36.4, 55.8, 105.2, 126.3, 126.4, 127.8, 129.0, 129.8, 130.1, 132.8, 138.1, 155.8. TOF HRMS (APCI): Calcd for C$_{34}$H$_{43}$O$_2$ [M+H] 483.3263, found, 483.3260. Anal. Calcd for C$_{34}$H$_{42}$O$_2$: C, 84.60; H, 8.77. Found: C, 83.47; H, 8.78.

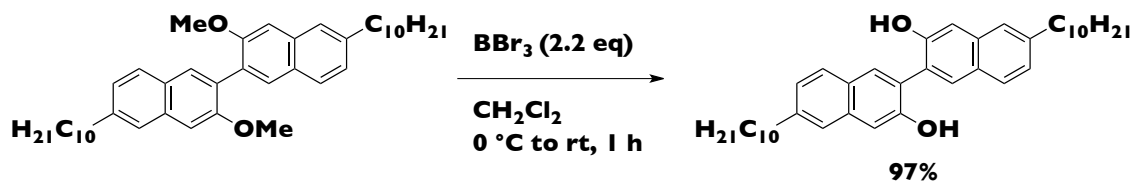**7,7'-Dioctyl-3,3'-dimethoxy-2,2'-binaphthalene**
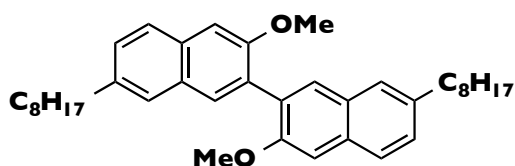
White solid. Yield: 54%. ^{1}H NMR (400 MHz, CDCl$_3$): δ 0.91 (t, J = 7.0 Hz, 6H, CH_3), 1.30–1.36 (m, 20H, (CH_2)$_5$), 1.71 (quin, J = 7.2 Hz, 4H, ArCH$_2$CH_2), 2.76 (t, J = 7.2 Hz, 4H, ArCH_2), 3.88 (s, 6H, OCH_3), 7.22 (s, 2H, ArH), 7.33 (d, J = 8.4 Hz, 2H, ArH), 7.58 (s, 2H, ArH), 7.72 (s, 2H, ArH), 7.73 (d, J = 8.4 Hz, 2H, ArH). ^{13}C NMR (100 MHz, CDCl$_3$): δ 14.2, 22.8, 29.4, 29.6, 29.7, 31.6, 32.0, 36.0, 55.4, 105.2, 126.3, 126.4, 127.8, 129.0, 129.8, 130.1, 132.8, 138.1, 155.8. TOF HRMS (APCI): Calcd for C$_{38}$H$_{51}$O$_2$ [M+H] 539.3889, found, 539.3885. Anal. Calcd for C$_{38}$H$_{50}$O$_2$: C, 84.71; H, 9.35. Found: C, 84.69; H, 9.38.

General procedure for demethylation reaction

**6,6'-Didecyl-2,2'-binaphthalene-3,3'-diol (for synthesis of C$_{10}$–DNF–VW)**

BBr$_3$ in dichloromethane (1.0 M, 16.5 mL, 16.5 mmol, 2.2 mol amt.) was added to a solution of 6,6'-didecyl-3,3'-dimethoxy-2,2'-binaphthalene (4.46 g, 7.50 mmol) in dichloromethane (30 mL) at 0 °C, and the resulting mixture was stirred at room temperature for 1 h. The crude material was poured into ice-water, and then the organic

layer was extracted with EtOAc, washed with water and brine, and dried over MgSO$_4$. After removing the solvent in vacuo, the crude material was purified by silica gel column chromatography (hexane:EtOAc = 80:20) to afford the title compound (4.12 g, 7.27 mmol, 97%) as a white solid. M.p.: 117.5–118.8 °C. ^{1}H NMR (600 MHz, CDCl$_3$): δ 0.89 (t, J = 7.2 Hz, 6H, CH_3), 1.26–1.41 (m, 28H, (CH_2)$_7$), 1.72 (quin, J = 7.2 Hz, 4H, ArCH$_2$CH_2), 2.77 (t, J = 7.2 Hz, 4H, ArCH_2), 5.51 (s, 2H, OH), 7.24 (d, J = 8.4 Hz, 2H, ArH), 7.36 (s, 2H, ArH), 7.54 (s, 2H, ArH), 7.73 (d, J = 8.4 Hz, 2H, ArH), 7.80 (s, 2H, ArH). ^{13}C NMR (150 MHz, CDCl$_3$): δ 14.3, 22.9, 29.51, 29.53, 29.7, 29.78, 29.80, 31.5, 32.1, 36.4, 111.0, 124.8, 125.0, 126.1, 127.7, 127.8, 130.8, 135.2, 142.0, 151.3. TOF HRMS (APCI): Calcd for C$_{40}$H$_{55}$O$_2$ [M+H] 567.4202, found 567.4199. Anal. Calcd for C$_{42}$H$_{54}$O$_2$: C, 84.75; H, 9.60. Found: C, 84.81; H, 9.34.

6,6'-Dibutyl-2,2'-binaphthalene-3,3'-diol
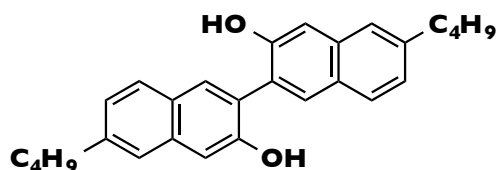
White solid. Yield: 92%. M.p.: 152.3–153.5 °C. ^{1}H NMR (600 MHz, CDCl$_3$): δ 0.96 (t, J = 7.2 Hz, 6H, CH_3), 1.42 (sext, J = 7.2 Hz, 4H, CH_2CH$_3$), 1.70 (quin, J = 7.2 Hz, 4H, ArCH$_2$CH_2), 2.78 (t, J = 7.2 Hz, 4H, ArCH_2), 5.61 (s, 2H, OH), 7.24 (d, J = 8.4 Hz, 2H, ArH), 7.36 (s, 2H, ArH), 7.54 (s, 2H, ArH), 7.73 (d, J = 8.4 Hz, 2H, ArH), 7.81 (s, 2H, ArH). ^{13}C NMR (150 MHz, CDCl$_3$): δ 14.1, 22.6, 33.6, 36.1, 111.0, 125.0, 125.1, 126.1, 127.7, 127.8, 130.9, 135.1, 141.9, 151.4. TOF HRMS (APCI): Calcd for C$_{28}$H$_{31}$O$_2$ [M+H] 399.2324, Found 399.2315.

6,6'-Dihexyl-2,2'-binaphthalene-3,3'-diol
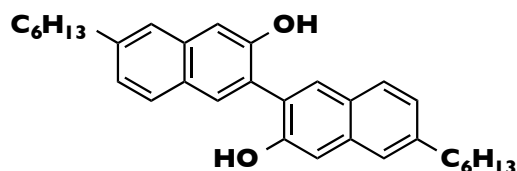
White solid. Yield: 96%. M.p.: 131.0–132.7 °C. ^{1}H NMR (600 MHz, CDCl$_3$): δ 0.90 (t, J = 7.2 Hz, 6H, CH_3), 1.32–1.39 (m, 12H, (CH_2)$_3$), 1.72 (quin, J = 7.8 Hz, 4H, ArCH$_2$CH_2), 2.77 (t, J = 7.8 Hz, 4H, ArCH_2), 5.54 (s, 2H, OH), 7.24 (d, J = 8.4 Hz, 2H,

Ar*H*), 7.36 (s, 2H, Ar*H*), 7.54 (s, 2H, Ar*H*), 7.73 (d, *J* = 8.4 Hz, 2H, Ar*H*), 7.81 (s, 2H, Ar*H*). ^{13}C NMR (150 MHz, CDCl$_3$): δ 14.3, 22.8, 29.2, 31.4, 31.9, 36.4, 111.0, 125.0, 126.1, 127.7, 127.8, 130.9, 135.1, 142.0, 151.3. TOF HRMS (APCI): Calcd for C$_{32}$H$_{39}$O$_2$ [M+H] 455.2950, found 455.2947.

6,6'-Dioctyl-2,2'-binaphthalene-3,3'-diol
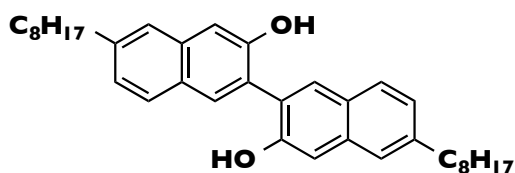
White solid. Yield: 86%. M.p.: 121.3–122.8 °C. ^{1}H NMR (600 MHz, CDCl$_3$) δ 0.88 (t, *J* = 7.2 Hz, 6H, C*H$_3$*), 1.27–1.38 (m, 20H, (C*H$_2$*)$_5$), 1.71 (quin, *J* = 7.8 Hz, 4H, ArCH$_2$C*H$_2$*), 2.77 (t, *J* = 7.8 Hz, 4H, Ar*CH$_2$*), 5.44 (s, 2H, O*H*), 7.24 (d, *J* = 8.4 Hz, 2H, Ar*H*), 7.37 (s, 2H, Ar*H*), 7.54 (s, 2H, Ar*H*), 7.73 (d, *J* = 8.4 Hz, 2H, Ar*H*), 7.81 (s, 2H, Ar*H*). ^{13}C NMR (150 MHz, CDCl$_3$): δ 14.3, 22.8, 29.4, 29.5, 29.7, 31.5, 32.0, 36.4, 111.1, 125.0, 126.2, 127.7, 127.8, 130.9, 135.2, 142.0, 151.3. TOF HRMS (APCI): Calcd for C$_{36}$H$_{47}$O$_2$ [M+H] 511.3576, found 511.3564.

7,7'-Didecyl-2,2'-binaphthalene-3,3'-diol (for synthesis of C$_{10}$–DNF–VV)
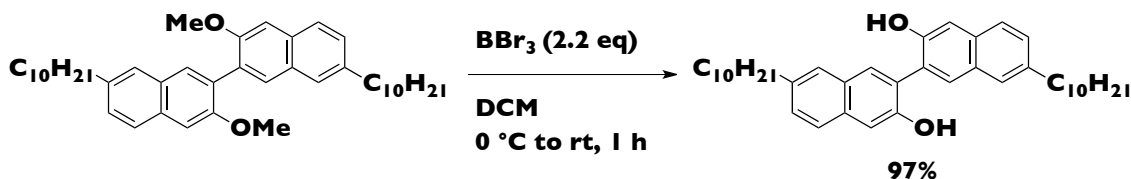
White solid. Yield: 97%. M.p.: 105.4–106.8 °C. ^{1}H NMR (400 MHz, CDCl$_3$): δ 0.88 (t, *J* = 6.4 Hz, 6H, CH$_3$), 1.26–1.35 (m, 28H, (CH$_2$)$_7$), 1.72 (quin, *J* = 7.6 Hz, 4H, ArCH$_2$C*H$_2$*), 2.76 (t, *J* = 7.6 Hz, 4H, Ar*CH$_2$*), 5.63 (s, 2H, OH), 7.34 (d, *J* = 8.4 Hz, 2H, Ar*H*), 7.39 (s, 2H, Ar*H*), 7.58 (s, 2H, Ar*H*), 7.69 (d, *J* = 8.4 Hz, 2H, Ar*H*), 7.79 (s, 2H, Ar*H*). ^{13}C NMR (100 MHz, CDCl$_3$): δ 29.76, 78 (two carbons), 31.6, 32.1, 36.1, 111.4, 125.9, 126.3, 126.4, 128.9, 129.5, 130.6, 133.4, 139.1, 150.7. TOF HRMS (APCI): Calcd for C$_{40}$H$_{55}$O$_2$ [M+H] 567.4202, found 567.4213.

7,7'-Dihexyl-2,2'-binaphthalene-3,3'-diol
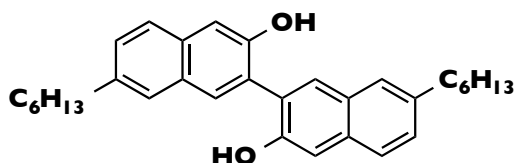
White solid. Yield: 91%. M.p.: 107.8–108.8 °C. ^{1}H NMR (400 MHz, CDCl$_3$): δ 0.89 (t, J = 7.0 Hz, 6H, CH_3), 1.32–1.35 (m, 12H, (CH_2)$_3$), 1.70 (quin, J = 7.5 Hz, 4H, ArCH$_2$CH_2), 2.76 (t, J = 7.5 Hz, 4H, ArCH_2), 5.47 (s, 2H, OH), 7.36 (d, J = 8.4 Hz, 2H, ArH), 7.40 (s, 2H, ArH), 7.58 (s, 2H, ArH), 7.70 (d, J = 8.4 Hz, 2H, ArH), 7.79 (s, 2H, ArH). ^{13}C NMR (100 MHz, CDCl$_3$): δ 14.3, 22.8, 29.2, 31.5, 31.9, 36.1, 111.6, 126.2, 126.3, 127.6, 128.3, 129.6, 130.9, 132.9, 138.7, 150.3. TOF HRMS (APCI): Calcd for C$_{32}$H$_{39}$O$_2$ [M+H] 455.2950, found 455.2944.

7,7'-Dioctyl-2,2'-binaphthalene-3,3'-diol
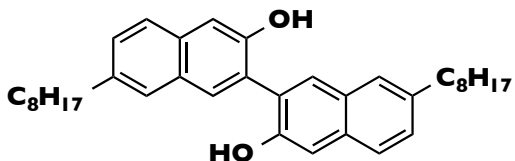
White solid. Yield: 95%. M.p.: 49.0–49.6 °C. ^{1}H NMR (400 MHz, CDCl$_3$): δ 0.88 (t, J = 7.0 Hz, 6H, CH_3), 1.28–1.35 (m, 20H, (CH_2)$_5$), 1.71 (quin, J = 7.2 Hz, 4H, ArCH$_2$CH_2), 2.76 (t, J = 7.2 Hz, 4H, ArCH_2), 5.51 (s, 2H, OH), 7.35 (d, J = 8.4 Hz, 2H, ArH), 7.40 (s, 2H, ArH), 7.58 (s, 2H, ArH), 7.69 (d, J = 8.4 Hz, 2H, ArH), 7.79 (s, 2H, ArH). ^{13}C NMR (100 MHz, CDCl$_3$): δ 14.2, 22.8, 29.5, 29.7, 29.9, 31.5, 32.1, 36.1, 111.6, 126.1, 126.3, 127.7, 128.2, 129.5, 130.9, 132.8, 138.6, 150.2. TOF HRMS (APCI): Calcd for C$_{36}$H$_{47}$O$_2$ [M+H] 511.3576, found 511.3573.

General procedure for synthesis of C$_n$–DNF–VW or C$_n$–DNF–VV derivatives

3,9-Didecyldinaphtho[2,3-b:2',3'-d]furan (C$_{10}$–DNF–VW)
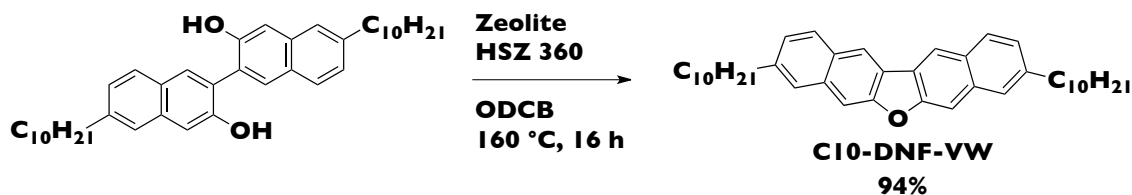
Zeolite HSZ-360 (200 mg) was added to a solution of 6,6'-didecyl-2,2'-binaphthalene-3,3'-diol (998 mg, 1.76 mmol) in 1,2-dichlorobenzene

(35 mL) and the reaction mixture was heated at 160 °C for 16 h. After the reaction was complete, the organic material was dissolved in hot 1,1,2,2-tetrachloroethane, which was passed through a short pad of silica gel using 1,1,2,2-tetrachloroethane to remove the zeolite. After reducing the solvent to ca. 10 mL in vacuo, addition of methanol afforded a white precipitate (909 mg, 1.66 mmol, 94%), which was collected by vacuum filtration. The obtained white solid was purified by vacuum sublimation with a diffusion pump (high temperature = 280 °C, low temperature = 180 °C, pressure < 0.003 Torr).

M.p.: 209.4–210.4 °C. ^{1}H NMR (600 MHz, CDCl$_2$CDCl$_2$): δ 0.82 (t, J = 6.6 Hz, 6H, CH_3), 1.22–1.36 (m, 28H, (CH_2)$_7$), 1.68 (quin, J = 7.2 Hz, 4H, ArCH$_2$CH_2), 2.75 (t, J = 7.2 Hz, 4H, ArCH_2), 7.31 (d, J = 8.4 Hz, 2H, ArH), 7.67 (s, 2H, ArH), 7.75 (s, 2H, ArH), 7.90 (d, J = 8.4 Hz, 2H, ArH), 8.40 (s, 2H, ArH). ^{13}C NMR (150 MHz, CDCl$_2$CDCl$_2$, 100 °C): δ 14.0, 22.6, 29.3, 29.4, 29.51, 29.59 (two carbons), 31.1, 31.9, 36.2, 106.1, 119.6, 124.6, 126.1, 126.3, 128.3, 128.9, 134.1, 141.2, 156.2. TOF HRMS (APCI): Calcd for C$_{40}$H$_{53}$O [M+H] 549.4096, found 549.4095. Anal. Calcd for C$_{40}$H$_{52}$O: C, 87.54; H, 9.55. Found: C, 87.59; H, 9.62.

3,9-Dihexyldinaphtho[2,3-*b*:2',3'-*d*]furan (C$_4$–DNF–VW)
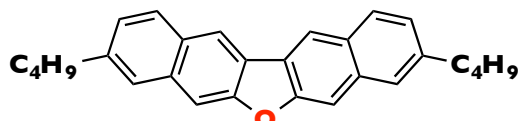
White solid. Yield: 97%. M.p.: 264.0–265.0 °C. ^{1}H NMR (400 MHz, CDCl$_3$): δ 0.98 (t, J = 7.2 Hz, 6H, CH_3), 1.39–1.46 (m, 4H, (CH_2)$_4$), 1.74 (quin, J = 8.0 Hz, 4H, ArCH$_2$CH_2), 2.82 (t, J = 8.0 Hz, 4H, ArCH_2), 7.34 (dd, J = 8.8, 1.2 Hz, 2H, ArH), 7.73 (s, 2H, ArH), 7.80 (s, 2H, ArH), 7.96 (d, J = 8.8 Hz, 2H, ArH), 8.44 (s, 2H, ArH). ^{13}C NMR (150 MHz, CDCl$_2$CDCl$_2$, 120 °C): δ 13.8, 22.4, 33.2, 35.8, 106.1, 119.5, 124.6, 126.1 (two carbons), 128.3, 129.0, 134.2, 141.1, 156.3. TOF HRMS (APCI): Calcd for C$_{28}$H$_{29}$O [M+H] 381.2218, found 381.2218. Anal. Calcd for C$_{28}$H$_{28}$O: C, 88.38; H, 7.42. Found: C, 88.30; H, 7.29.

3,9-Dihexyldinaphtho[2,3-*b*:2',3'-*d*]furan (C$_6$–DNF–VW)
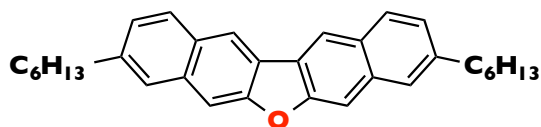
White solid. Yield: 88%. M.p.: 246.5–247.6 °C. ^{1}H NMR (600 MHz, CDCl$_3$): δ 0.90 (t, J = 7.2 Hz, 6H, CH_3), 1.34–1.42 (m, 12H, (CH_2)$_3$), 1.75 (quin, J = 7.2 Hz, 4H, ArCH$_2$CH_2), 2.82 (t, J = 7.2 Hz, 4H, ArCH_2), 7.34 (dd, J = 7.8, 1.2 Hz, 2H, ArH), 7.73 (s, 2H, ArH), 7.80 (s, 2H, ArH), 7.95 (d, J = 7.8 Hz, 2H, ArH), 8.44 (s, 2H, ArH). ^{13}C NMR (150 MHz, CDCl$_2$CDCl$_2$, 100 °C): δ 14.0, 22.5, 29.0, 31.1, 31.7, 36.2, 106.2, 119.6, 124.6, 126.1, 126.3, 128.3, 128.9, 134.1, 141.2, 156.3. TOF HRMS (APCI): Calcd for C$_{32}$H$_{37}$O [M+H] 437.2844, found 437.2837. Anal. Calcd for C$_{40}$H$_{52}$O: C, 88.03; H, 8.31. Found: C, 88.06; H, 8.26.

3,9-Dioctyldinaphtho[2,3-*b*:2',3'-*d*]furan (C$_8$–DNF–VW)
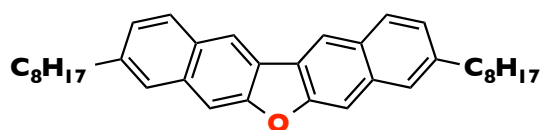
White solid. Yield: 42%. M.p.: 105.4–106.8 °C. ^{1}H NMR (400 MHz, CDCl$_3$): δ 0.89 (t, J = 6.8 Hz, 6H, CH_3), 1.28–1.37 (m, 20H, (CH_2)$_5$), 1.75 (quin, J = 7.2 Hz, 4H, ArCH$_2$CH_2), 2.82 (t, J = 6.8 Hz, 4H, ArCH_2), 7.34 (dd, J = 8.4, 1.6 Hz, 2H, ArH), 7.73 (s, 2H, ArH), 7.80 (s, 2H, ArH), 7.95 (d, J = 8.4 Hz, 2H, ArH), 8.44 (s, 2H, ArH). ^{13}C NMR (150 MHz, CDCl$_2$CDCl$_2$, 120 °C): δ 13.9, 22.5, 29.1, 29.4 (two carbons), 31.0, 31.8, 36.2, 106.1, 119.5, 124.6, 126.1, 126.3, 128.3, 129.0, 134.2, 141.1, 156.3. TOF HRMS (APCI): Calcd for C$_{36}$H$_{45}$O [M+H] 493.3470, found 493.3463. Anal. Calcd for C$_{36}$H$_{44}$O: C, 87.75; H, 9.00. Found: C, 87.69; H, 9.10.

### 2,10-Didecyldinaphtho[2,3-*b*:2',3'-*d*]furan (C$_{10}$–DNF–VV)
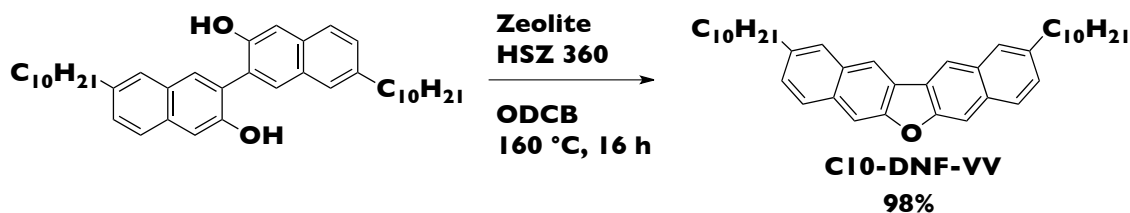
White solid. Yield: 98%. The obtained white solid was finally purified by vacuum

sublimation with a diffusion pump (High temperature = 250 °C, low temperature = 150 °C, pressure < 0.003 Torr).

M.p.: 173.9–174.3 °C. ^{1}H NMR (400 MHz, CDCl$_3$): δ 0.89 (t, J = 6.4 Hz, 6H, CH_3), 1.26–1.40 (m, 28H, (CH_2)$_7$), 1.75 (quin, J = 7.2 Hz, 4H, ArCH$_2$CH_2), 2.82 (t, J = 7.2 Hz, 4H, ArCH_2), 7.40 (d, J = 8.4 Hz, 2H, ArH), 7.81 (s, 2H, ArH), 7.83 (s, 2H, ArH), 7.88 (d, J = 8.4 Hz, 2H, ArH), 8.43 (s, 2H, ArH). ^{13}C NMR (150 MHz, CDCl$_2$CDCl$_2$): δ 14.4, 22.9, 29.5, 29.6, 29.70, 29.77, 29.79, 31.5, 32.0, 36.1, 106.5, 119.6, 125.1, 126.8, 127.6, 128.3, 130.3, 132.0, 139.3, 155.4. TOF HRMS (APCI): Calcd for C$_{40}$H$_{53}$O [M+H] 549.4096, found 549.4128. Anal. Calcd for C$_{40}$H$_{52}$O: C, 87.54; H, 9.55. Found: C, 87.61; H, 9.50.

2,10-Dihexyldinaphtho[2,3-b:2',3'-d]furan (C6–DNF–VV)
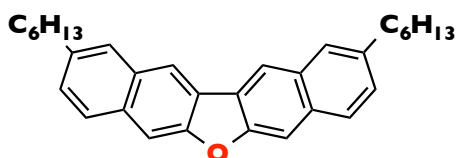
White solid. Yield: 97%. M.p.: 198.7–199.1 °C. ^{1}H NMR (600 MHz, CDCl$_3$): δ 0.91 (t, J = 6.6 Hz, 6H, CH_3), 1.34–1.42 (m, 12H, (CH_2)$_5$), 1.75 (quin, J = 7.8 Hz, 4H, ArCH$_2$CH_2), 2.82 (t, J = 7.8 Hz, 4H, ArCH_2), 7.40 (d, J = 7.8 Hz, 2H, ArH), 7.81 (s, 2H, ArH), 7.83 (s, 2H, ArH), 7.88 (d, J = 8.4 Hz, 2H, ArH), 8.43 (s, 2H, ArH). ^{13}C NMR (150 MHz, CDCl$_2$CDCl$_2$, 100 °C): δ 14.0, 22.6, 29.0, 31.1, 31.7, 36.0, 106.4, 119.4 (two carbons), 125.3, 126.7, 127.6, 130.6, 132.4, 139.2, 155.7. TOF HRMS (APCI): Calcd for C$_{40}$H$_{53}$O [M+H] 549.4096, found 549.4095. Anal. Calcd for C$_{32}$H$_{36}$O: C, 88.03; H, 8.31. Found: C, 88.12; H, 8.26.

2,10-Dioctyldinaphtho[2,3-b:2',3'-d]furan (C8–DNF–VV)
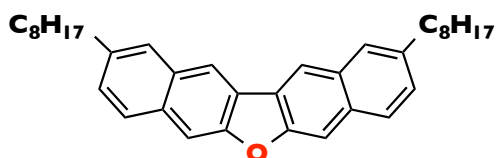
White solid. Yield: 78%. M.p.: 187.0–188.0 °C. ^{1}H NMR (600 MHz, CDCl$_3$): δ 0.89 (t, J = 6.6 Hz, 6H, CH_3), 1.29–1.41 (m, 20H, (CH_2)$_5$), 1.75 (quin, J = 7.8 Hz, 4H, ArCH$_2$CH_2), 2.82 (t, J = 7.8 Hz, 4H, ArCH_2), 7.40 (d, J = 8.4 Hz, 2H, ArH), 7.81 (s, 2H, ArH), 7.83 (s, 2H, ArH), 7.88 (d, J = 8.4 Hz, 2H, ArH), 8.43 (s, 2H, ArH). ^{13}C NMR

(150 MHz, CDCl$_2$CDCl$_2$, 120 °C): δ 13.9, 22.5, 29.1, 29.4 (two carbons), 31.1, 31.8, 36.0, 106.4, 119.3, 125.3, 126.7, 127.5, 128.1, 130.7, 132.4, 139.1, 155.8. TOF HRMS (APCI): Calcd for C$_{36}$H$_{45}$O [M+H] 493.3470, found 493.3462. Anal. Calcd for C$_{36}$H$_{44}$O: C, 87.75; H, 9.00. Found: C, 87.83; H, 8.87.

Chapter 3

Evaluation of Carrier-Transporting Properties of V-Shaped and W-Shaped Organic Semiconductors

3.1 Introduction

Organic field-effect transistors (OFETs) have been of great interest in recent years as next-generation electronic components such as pixel control devices in active matrix flexible displays. There is one advantage in evaluating carrier transport abilities using FETs compared with techniques such as space charge limited current (SCLC) and time of flight (TOF) – a small amount of sample (ca. 10 mg) is enough. The key parameters extracted from OFETs are carrier mobility, on/off current ratio (I_{on}/I_{off}), and threshold voltage. Mobility is one of the most commonly reported benchmarks and is essentially the drift velocity of the charge carrier (cm s^{-1}) per applied field (V cm^{-1}), leading to units for mobility of cm^2 V^{-1} s^{-1}.

A schematic illustration of an OFET structure is shown in *Figure 35*. The OFET consists of three parts: an insulator layer, an organic semiconducting layer, and three metallic electrodes. Two of the electrodes, called the source and drain, have direct contacts with the organic semiconductor. The third electrode, called the gate, is electrically isolated from the semiconductor by the gate insulator. When the gate voltage, V_G, between the gate and source is applied, an electric field emerges within the metal–insulator–semiconductor (MIS) structure. To terminate the electric field, charges are injected simultaneously from the metal–semiconductor contacts into the organic semiconductor, as in the case of a capacitor. If the injected charges are conductive, the charge carriers travel through the organic semiconductor from the source to the drain electrodes when a drain voltage V_D is applied, and a drain current I_D is obtained.
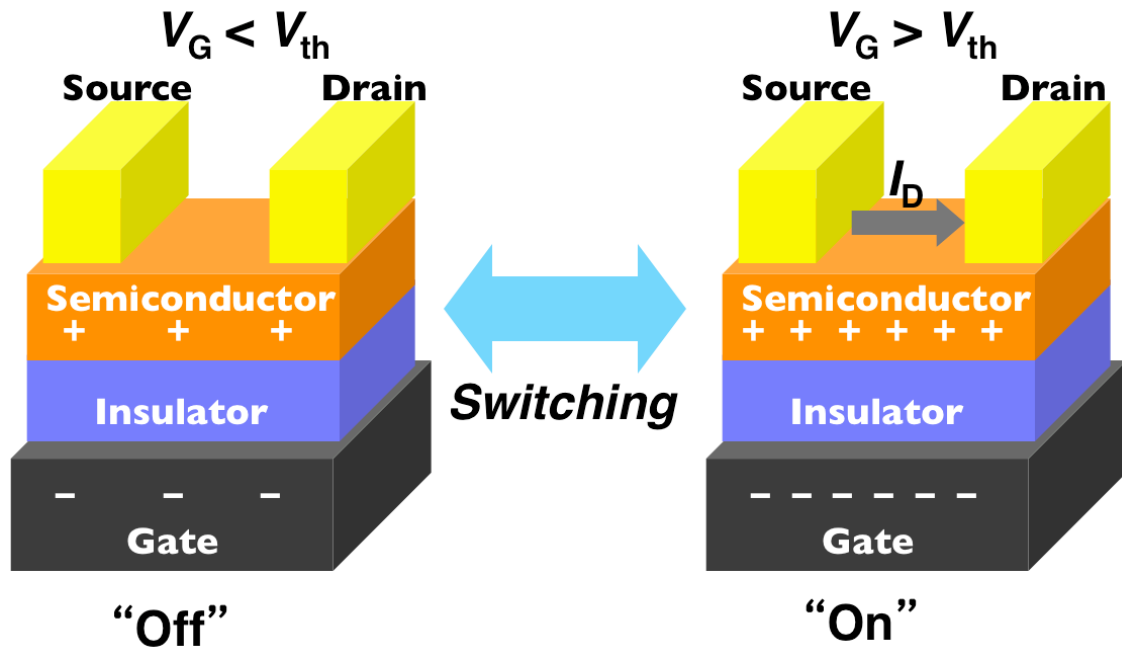
Figure 35. Schematic illustration of typical OFET device.

The electrical conductivity σ of a solid is simply described using the carrier density n and carrier mobility μ, and is the average carrier velocity per unit of electric field along the direction of charge transport:

$$\sigma = ne\mu, \tag{3.1}$$

where e is the elementary charge. Similar to the amount of charge in a capacitor, the charge density of carriers in an organic semiconductor, which is accumulated by the OFET structure, is generally estimated as

$$Q = C(V_G - V_{th}) = ne, \tag{3.2}$$

where C is the capacitance of the gate insulator per unit area and V_{th} is the threshold voltage equivalent to that required to start accumulating charge carriers. Practical OFETs sometimes require a finite threshold voltage to eliminate possible carriers, carrier traps, or dipoles at the surface of the gate insulator.

When the drain voltage, V_D, which is much smaller than V_G, is applied between the source and drain (the so-called linear region), it is presumed that the carrier density is

uniform across the channel. The σ value of the organic semiconductor, which depends on the applied V_G and C, can be obtained from Eqs. 3.1 and 3.2, and σ of an OFET can therefore be described as

$$\sigma = C(V_G - V_{th})\mu.$$

(3.3)

The drain current I_D flowing between the two electrodes is estimated, using V_D, as

$$I_D = C(V_G - V_{th})\mu V_D \frac{W}{L}.$$

(3.4)

Here, L and W are the length and width of the conduction channel, respectively. Eq. 3.5 provides the carrier mobility μ as

$$\mu = \frac{1}{CV_D} \frac{\partial I_D}{\partial V_G} \frac{L}{W}.$$

(3.5)

Figure 36 (a) shows a schematic representation of the characteristics of a p-type OFET, by plotting I_D as a function of V_G in the linear region. I_D increases linearly with V_G at $|V_{th}|$ << $|V_G|$, where the proportionality factor indicates the carrier mobility. In this regard, however, a discussion of I_D and μ is based on the assumption that the contact resistance between the organic semiconductor and metal is negligibly small.
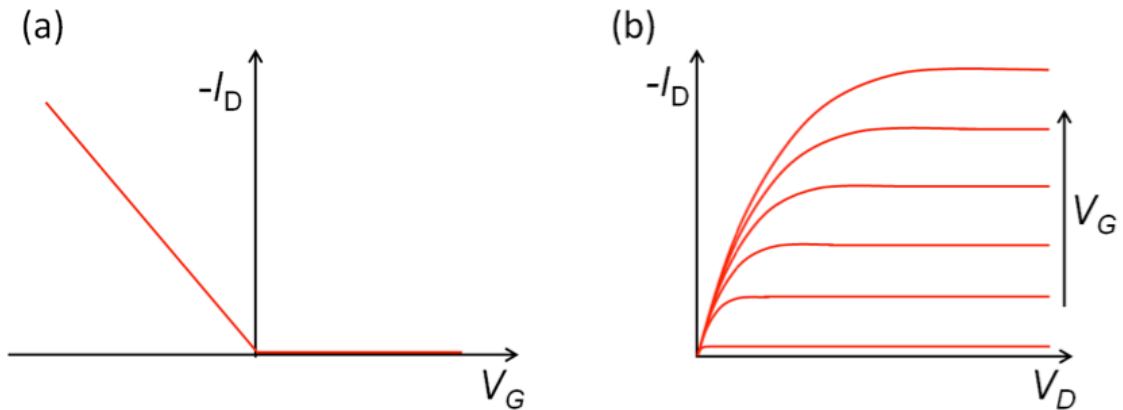
Figure 36. Schematic representation of characteristics of p-type OFETs: (a) I_D (σ) vs. V_G plot and (b) I_D vs. V_D plot for p-type OFETs.

When the drain voltage increases to much higher than the gate voltage ($V_D \gg V_G$), a region in which the accumulated charges are reduced to nearly zero, and the current is produced by diffusion of carriers, is formed next to the drain. A schematic representation of the I_D–V_D characteristics (the output characteristics) are shown in *Figure 36* (b) for a p-type device. The I_D (V_D) saturates at $V_D \gg V_G$, therefore this region is called a saturation region. In this region, the drain current is obtained as

$$I_D = \frac{1}{2}C(V_G - V_{th})^2 \mu \frac{W}{L} \qquad\qquad \textbf{(3.6)}$$

through the gradual channel approximation. According to Eq. 3.6, the mobility, μ, can be estimated based on the slope of a plot of $\sqrt{I_D}$ vs. V_G. According to Eq. 3.6, there are various ways of obtaining a large drain current. One is increasing the channel width; however, the larger the channel width becomes, the larger the device will be. Next is decreasing the channel length, but there is a technical limit. The most effective way to generate a large drain current is enhancement of the mobility. In addition, mobility enhancement will achieve high-speed switching.

In Chapter 2, the author described the design and synthesis of oxygen-bridged V-shaped organic materials (**DNF–V**s), and clarified that **DNF–V** derivatives form herringbone packing structures in single-crystals, which are preferable for two-dimensional charge carrier conduction. In this chapter, the author describes the evaluation of the carrier-transporting abilities of **DNF–V** derivatives by application in FETs in the form of polycrystalline and single-crystalline films.

3.2 Evaluation of Hole Mobility in Polycrystalline Film

Since the ionization potentials of **DNF–V** derivatives are suitable for applications in p-type OFETs, as mentioned in Chapter 2, the author first fabricated organic thin-film transistors (OTFTs) in the form of vacuum-deposited polycrystalline thin films. The device fabrication process is as follows. The surface of a substrate with 500 nm thick thermally oxidized SiO_2 (relative dielectric constant: 3.9, C = 6.9 nF cm^{-2}) on n-doped Si, the gate electrode, was washed in an ultrasound bath with acetone and 2-propanol for 5 min, consecutively. The surface was then cleaned using a UV lamp for 30 min. The clean substrate was then treated with decyltriethoxysilane (DTS)[46] or

heptadecafluorodecyltriethoxysilane (F-DTS)[47] in a furnace to form self-assembled monolayers (SAMs). Thin films of organic semiconductors were deposited under reduced pressure at a deposition rate of 0.5 Å s^{-1}. When thin-film formation was complete, an acceptor (2,3,5,6-tetrafluoro-7,7,8,8-tetracyanoquinodimethane, F$_4$-TCNQ: 1 nm)[48] and gold (30 nm) were successively deposited. The device configuration (top-contact–bottom-gate) is illustrated in *Figure 37*. Electrical characterization was performed using a semiconductor parameter analyzer (Keithley 4200). The field-effect mobilities in the saturation region were estimated using Eq. 3.6.
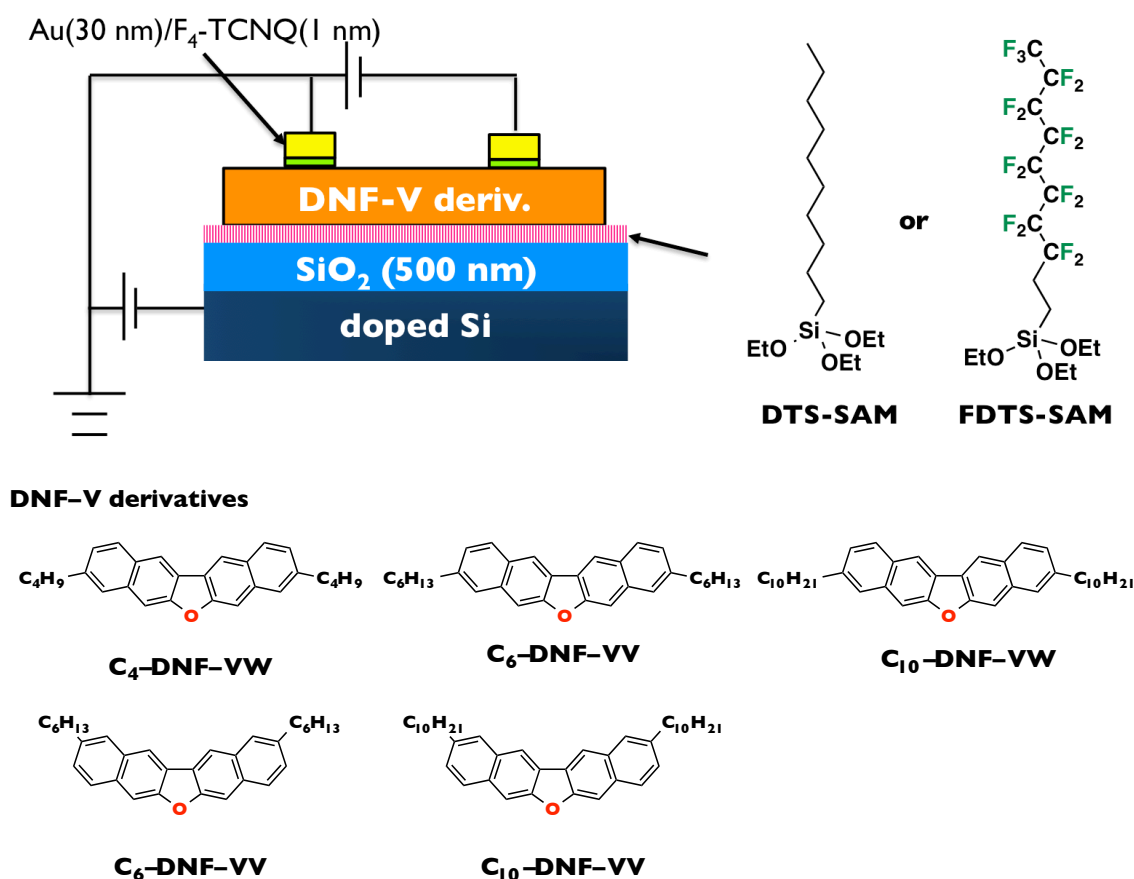
Figure 37. Top-contact–bottom-gate OFET configuration to demonstrate carrier mobilities of **DNF–V** derivatives in polycrystalline film.

The author fabricated OTFTs based on **C$_4$–DNF–VW**, **C$_6$–DNF–VW**, **C$_{10}$–DNF–VW**, **C$_6$–DNF–VV**, and **C$_{10}$–DNF–VV**. As summarized in *Table 7*, **C$_n$–DNF–VW** on F-DTS-treated substrates exhibited higher performances than those on DTS-treated substrates. The transfer and output characteristics of **C$_6$–DNF–VW** devices are shown

in *Figure 38*. Among **DNF–V** derivatives, **C₆–DNF–VW** exhibited the maximum hole mobility, 1.61 cm² V⁻¹ s⁻¹, and hysteresis was almost reduced in the thin film deposited on the F-DTS-treated substrate.

Table 7. OTFT characteristics of **C$_n$–DNF–VW**- and **C$_n$–DNF–VV**-based devices[a]

Compound	SAM	μ_{sat} (cm² V⁻¹ s⁻¹)[a]	I_{on}/I_{off}
C₄–DNF–VW	DTS	0.45–0.59	10^5
	F-DTS	0.60–0.78	10^4
C₆–DNF–VW	DTS	0.07–0.39	10^5
	F-DTS	1.07–1.61	10^5
C₁₀–DNF–VW	DTS	0.43–0.61	10^4
	F-DTS	0.80–0.84	10^5
C₆–DNF–VV	DTS	no field-effect	–
	F-DTS	10^{-3}	10^2
C₁₀–DNF–VV	DTS	0.02–0.4	10^4
	F-DTS	0.06–0.5	10^5

[a]Four devices were examined. Top-contact–bottom-gate configuration with L/W =1/10; substrate temperature: 120 °C.

63
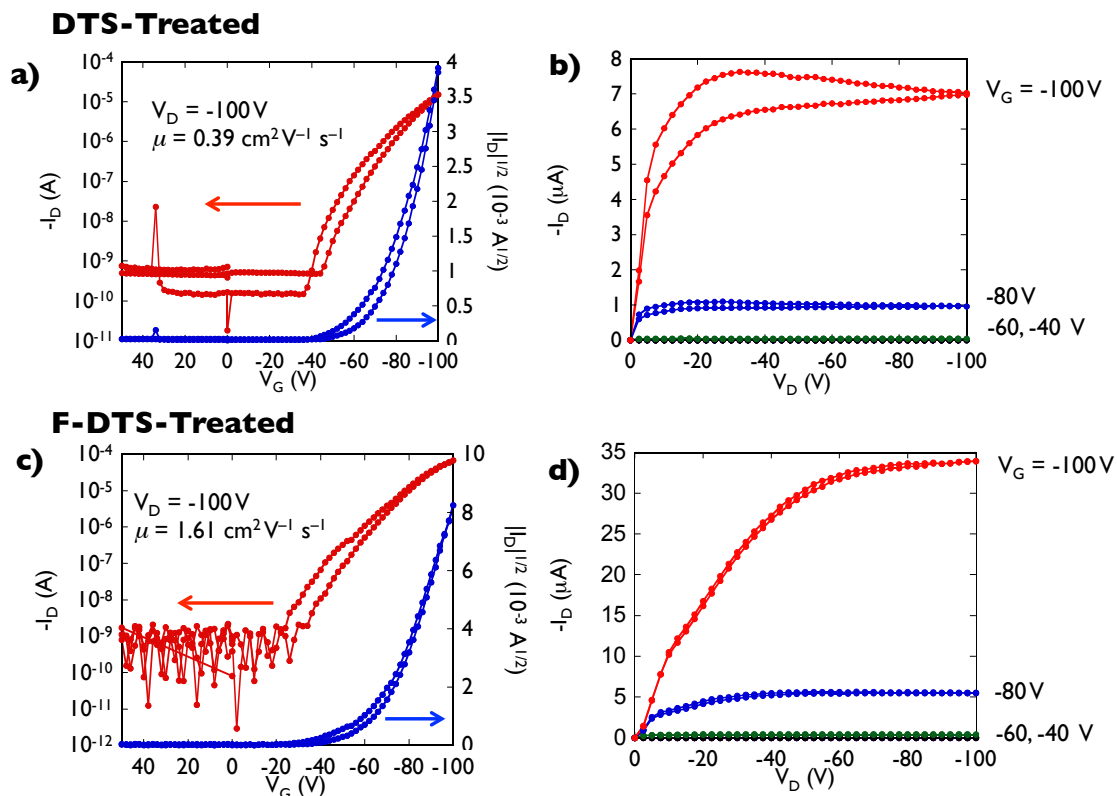
Figure 38. OTFT characteristics of **C₆–DNF–VW**. a) and c): transfer curves; b) and d): output curves.

Thin-film XRD analyses were carried out on vacuum-deposited OTFT devices, using a Rigaku Ultima VI X-ray diffractometer (Cu Kα source: $\lambda = 1.54187$ Å). Representative thin-film XRD patterns (**C₆–DNF–VW**) are shown in *Figure 39*. Peaks can be assigned if the molecules are oriented in an edge-on manner. The length of the long axis ($a = 54.69(4)$ Å) is in good accordance with the *d*-spacings of **C₆–DNF–VW**. Atomic force microscopy (AFM) images (*Figure 40*) showed that the crystalline grains on the F-DTS-treated substrate were smaller than those on the thin film on the DTS-treated substrate. Despite the film morphology, the reason that the thin film deposited on the F-DTS-treated SiO_2 had higher mobility might be the high water repellency of F-DTS. (Water is the origin of hysteresis.)
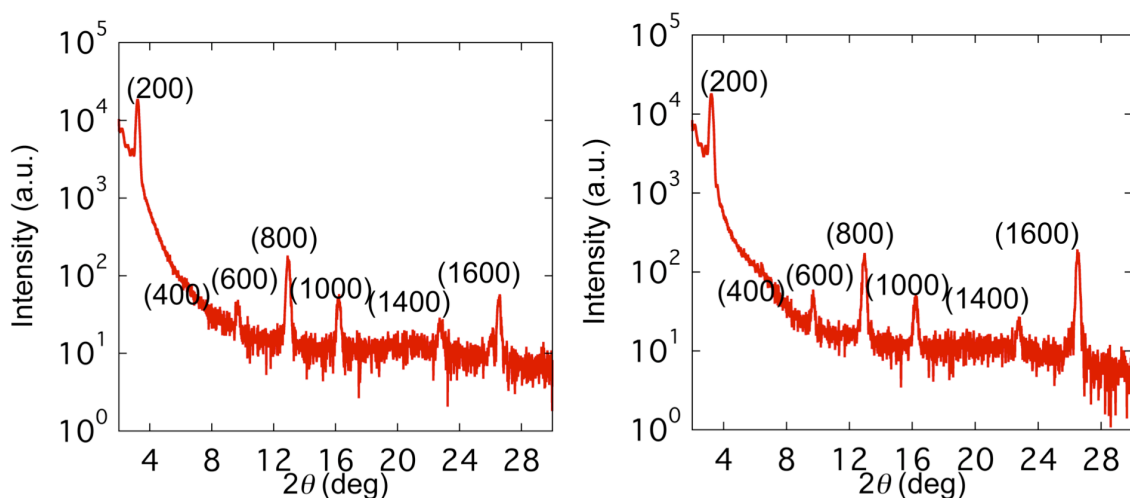
Figure 39. Thin-film XRD patterns of **C₆–DNF–VW** on DTS- (left) and F-DTS-treated (right) Si/SiO₂ substrate; calculated *d*-spacing from (200) ($2\theta = 3.208°$) peak was 55.22 Å.
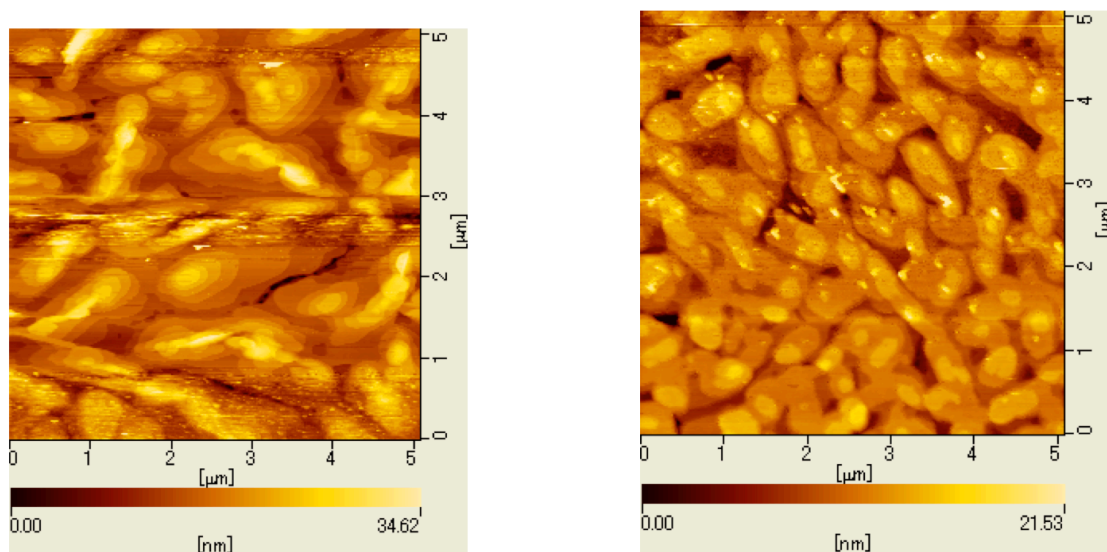
Figure 40. AFM image of **C₆–DNF–VW** on DTS- (left) and F-DTS-treated (right) Si/SiO₂ substrate.

3.3 Evaluation of Hole Mobility in Single-Crystalline Film

The examination of organic semiconducting single crystals is a powerful method for evaluation of intrinsic charge carrier transport capabilities because single crystals have little disorder and no grain boundaries.[49,50] An extremely high hole mobility of 25–40 cm² V⁻¹ s⁻¹ has been achieved using rubrene,[51] and extensive research on single-crystal

transistors is now being performed. The author fabricated single-crystal FETs with **DNF–V**, **C$_{10}$–DNF–VW**, and **C$_{10}$–DNF–VV**. Single crystals suitable for FETs were prepared by physical vapor transport (PVT)[9,51–55] or edge-casting[56] methods, although polycrystalline thin films are popular for industrial use.

Single-Crystal Field-Effect Transistor

Single crystals of alkyl-**DNF–V** derivatives are hard to prepare by PVT, so the author used the edge-casting method. A representative single crystal for a FET is shown in *Figure 41*. The procedure was as follows. The surfaces of substrates with 500 nm or 200 nm thick thermally oxidized SiO$_2$ on doped Si were first cleaned in an ultrasound bath with acetone and 2-propanol for 5 min, consecutively. The surfaces of the cleaned substrates were treated with vapor-deposited β-trimethoxy(2-phenylethyl)silane (PTS).[57] The crystalline thin films were formed using a 0.1 wt% solution of **C$_{10}$–DNF–VV** or **C$_{10}$–DNF–VW** in *o*-dichlorobenzene. A prepared droplet (approximately 50–100 μL) was maintained at the edge of a structure on an inclined substrate at room temperature, so that the crystalline domain grew in the direction of the inclination through evaporation of the solvent. The structure for supporting the droplet can be a small piece of a Si wafer and can be removed after growth of the crystalline film. The acceptor (F$_4$-TCNQ) and the source–drain gold electrodes were then successively deposited on the film through a shadow mask. The doped Si layer acts as a gate electrode with a dielectric constant of 3.9. Electrical characterization was performed using a semiconductor parameter analyzer (Keithley 4200). The field-effect mobilities in the saturation region were estimated using Eq. 3.6. *Figure 42* and *Figure 43* show the single-crystal FET performances using crystalline films based on **C$_{10}$–DNF–VV** and **C$_{10}$–DNF–VW**, respectively. Each device exhibited large hysteresis, which is fatal for practical applications.

According to previous reports, the main origin of hysteresis is the presence of water or oxygen.[58] To reduce the effects of oxygen or water as trap sites, a device consisting of a **C$_{10}$–DNF–VW** crystalline film on a β-PTS-treated 200 nm SiO$_2$ substrate was washed with hydrophilic acetonitrile, which does not dissolve most of the organic semiconductor. As a result, almost no hysteresis was observed for the FET device based on **C$_{10}$–DNF–VW**, as shown in *Figure 44*.
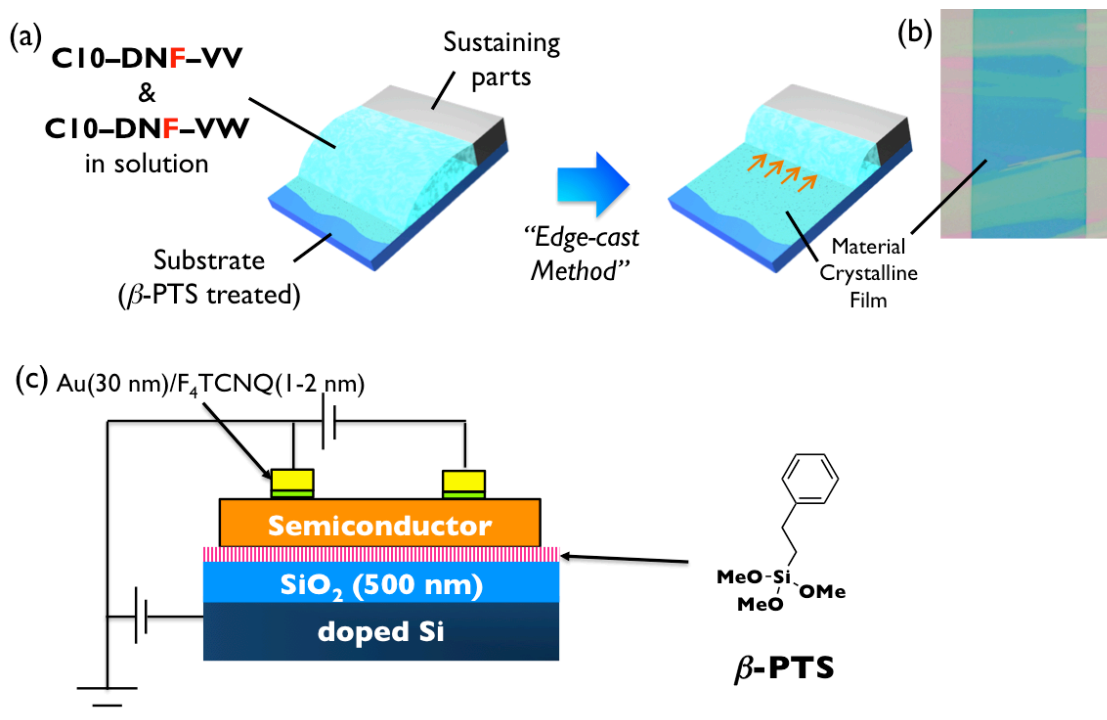
Figure 41. (a) Schematic diagram of crystalline thin film formation by edge-casting method, (b) representative photograph of single-crystal transistor using **C$_{10}$–DNF–VV**, and (c) schematic diagram of structure of device based on **C$_{10}$–DNF–VV** derivatives.
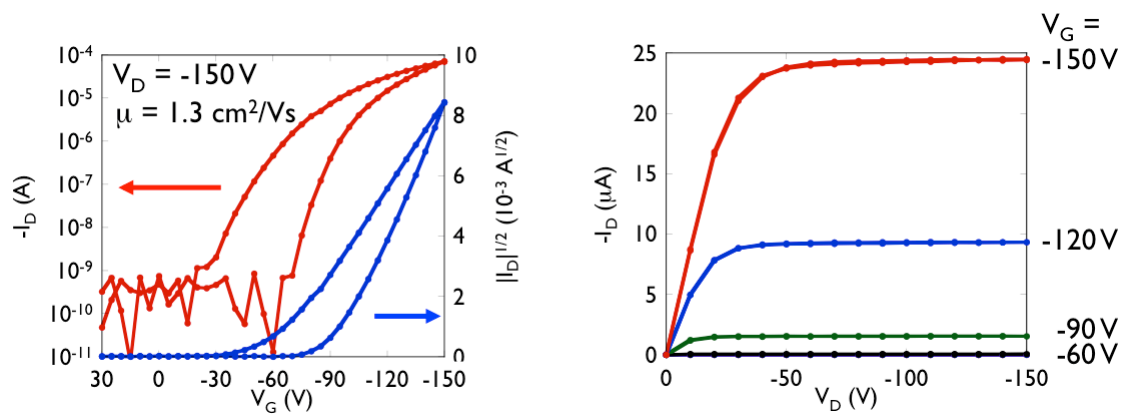
Figure 42. OFET characteristics of **C$_{10}$–DNF–VV**: transfer (left) and output (right) ($L/W = 295/880$, SiO$_2$: 500 nm).
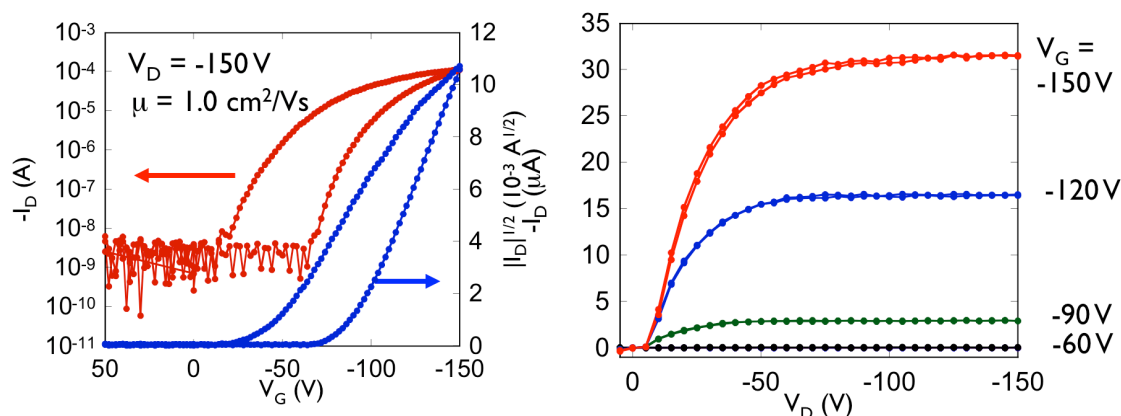
Figure 43. OFET characteristics of **C₁₀–DNF–VW**: transfer (left) and output (right) (*L/W* = 195/490, SiO₂: 500 nm).

Figure 44. OFET characteristics of **C₁₀–DNF–VW** (washed with acetonitrile): transfer (left) and output (right) (*L/W* = 7/30, SiO₂: 200 nm).

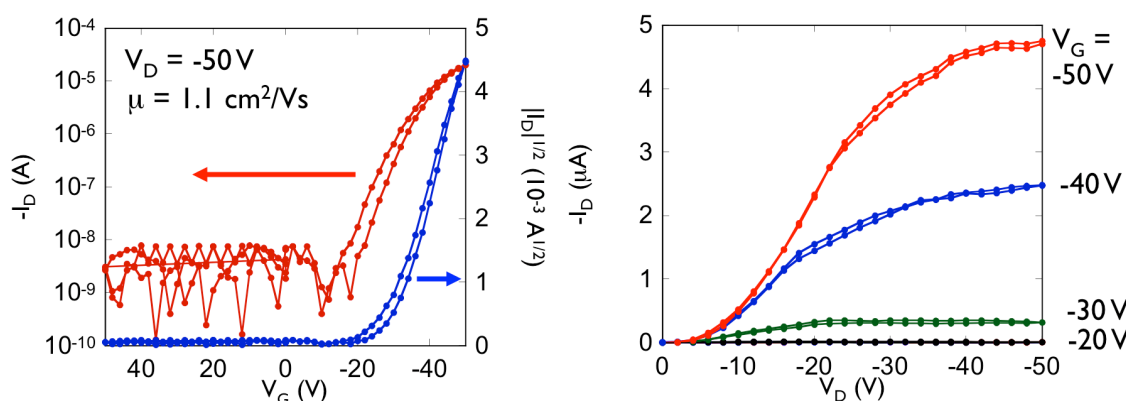Single crystals of unsubstituted oxygen-bridged organic semiconductors (**DNF–V** and **DNF–W**) were prepared by PVT under an argon gas flow. Because favorable semiconductor–insulator interfaces could only be formed by laminating organic single crystals, the author chose a top-contact–bottom-gate configuration (*Figure 45*). The procedure was as follows. The surfaces of substrates with 500 nm thick thermally oxidized SiO₂ on n-doped Si were first cleaned in an ultrasound bath with acetone and 2-propanol for 5 min, consecutively. The surfaces of the cleaned substrates were treated with vapor-deposited heptadecafluorodecyltriethoxysilane (F-DTS). A thin single crystal of **DNF–V** was attached to the prepared substrate electrostatically to construct a transistor. F_4-TCNQ was deposited on the top of the laminated single crystal, to afford an overall thickness of 1–2 nm and gold electrodes (30 nm) were successively deposited through a shadow mask. The **DNF–W** crystal was needle shaped, so the author

fabricated the FET device in a top-contact–top-gate manner (*Figure 46*). The fabrication process was as follows. Parylene SR[53,59] was deposited as the dielectric, with a relative dielectric constant of 3.0 (1300 nm, $C = 2.0$ nF cm^{-2}). A gate electrode was then drawn on the surface of the parylene-coated single crystal using carbon paste.

Figure 45. Single-crystal FET based on **DNF–V**: a) device configuration, b) representative photograph of **DNF–V** single crystal, and c) transfer and d) output curves.

Figure 46. Single-crystal FET based on **DNF–W**: a) top-contact–top-gate device configuration, b) representative photograph of **DNF–W** single-crystal, and c) transfer and d) output curves.

The device characteristics of furan-containing organic semiconductors are summarized in *Table 8*.

Table 8. Single-crystal FET performances of furan-containing organic semiconductors

Compound	μ_{sat} (cm^2 V^{-1} s^{-1})	I_{on}/I_{off}
C$_{10}$–DNF–VV	1.3	10^5
C$_{10}$–DNF–VW	1.1	10^5
DNF–V	1.3	10^5
DNF–W	10^{-2}	10^3

AFM Images of Solution-Crystallized Thin Films

AFM images of solution-crystallized thin films based on **C$_{10}$–DNF–VW** showed that the films were homogeneous. The height of the terrace-like step (–3.7 nm) was in good agreement with the length of **C$_{10}$–DNF–VW** (–3.6 nm), as shown in *Figure 47*. This

means that the molecules are oriented perpendicular to the substrate and the surface is flat on the molecular scale.
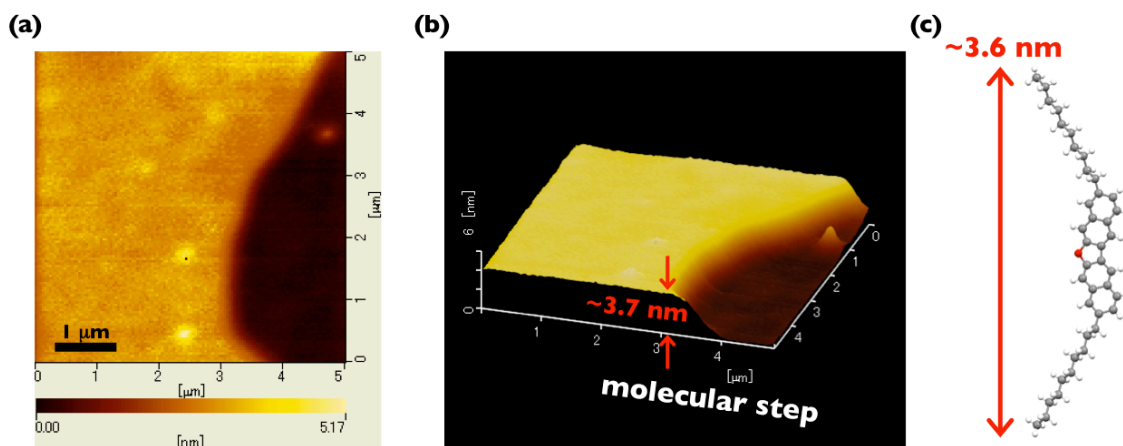
Figure 47. AFM images of solution-grown films of **C$_{10}$–DNF–VW**: (a) top view, (b) bird's eye view, and (c) schematic illustration of crystal structure of **C$_{10}$–DNF–VW**.

Transmission X-Ray Diffraction Patterns of Solution-Crystallized Thin films

In order to examine the in-plane and out-of-plane crystallinities of the alkylated **DNF–V** film, X-ray-diffraction measurements were performed using the high-energy X-ray source (λ = 1.01060 Å) at the photon factory at SPring-8 BL02B1,[48] which is a very bright synchrotron light source, because the single-crystalline thin film is too thin to be measured using irradiation by a laboratory-scale X-ray source. *Figure 48* shows the set-up for transmission XRD measurements. The incident X-ray was irradiated on the substrate vertically for in-plane measurements, and parallel for out-of-plane measurements.
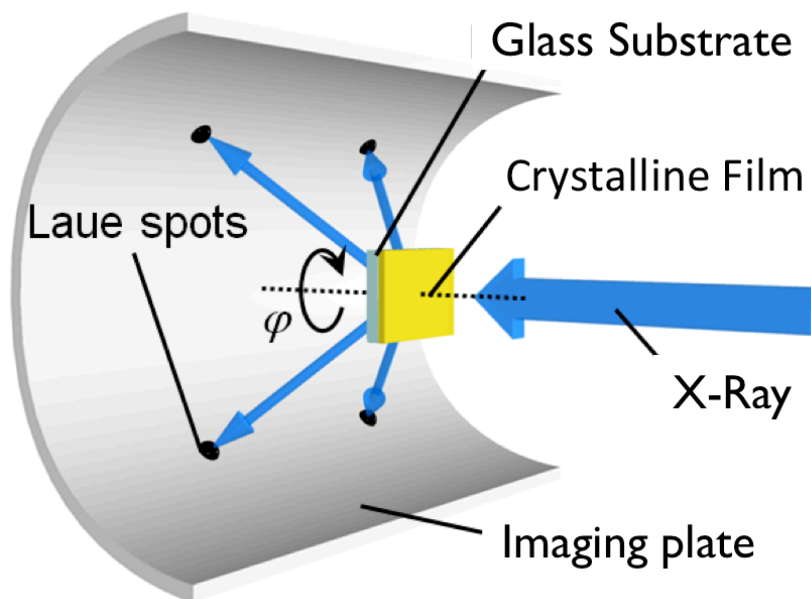
Figure 48. Schematic diagram of apparatus for transmission XRD measurements.

Figure 49 (a) and (b) show a view of the imaging plate, demonstrating obvious Laue spots at the right positions for X-ray irradiation of the bulk crystal of **C$_{10}$–DNF–VW**. The Laue spots were fully assigned from the powder pattern of the material. Clear Laue spots could be assigned to the (*hkl*) parameters when the single-crystalline thin film was formed on a glass substrate. When the film consists of polycrystals, Debye–Scherrer rings are observed on the imaging plate. This is evidence that the solution-grown film of **C$_{10}$–DNF–VW** is essentially a single domain of submillimeter size where the X-ray is irradiated.
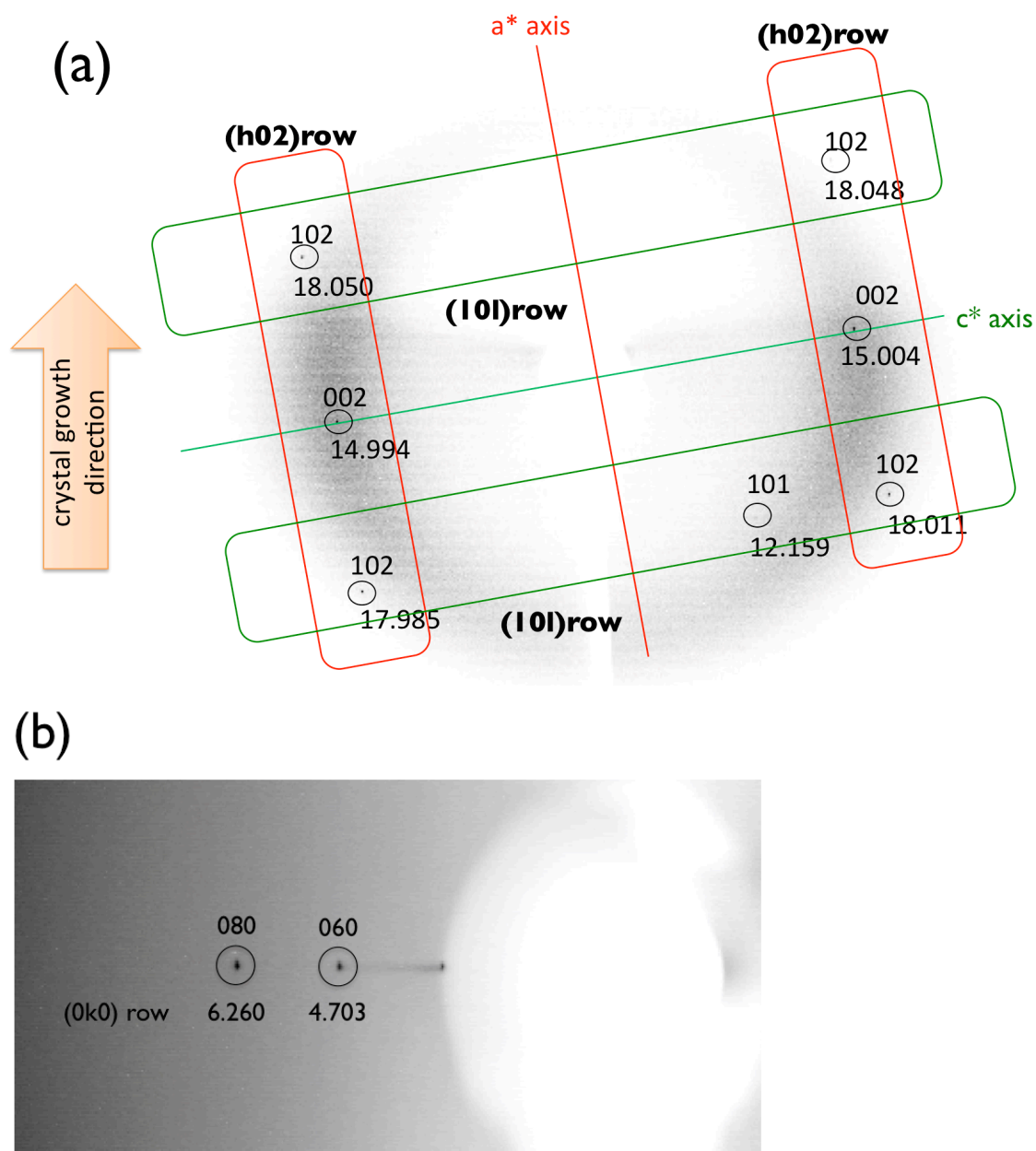
Figure 49. Laue spots of solution-crystallized C_{10}–DNF–VW thin film on imaging plate in (a) in-plane and (b) out-of-plane measurements.

Figure 50 shows Laue spots at the right positions under X-ray irradiation of a bulk crystal of C_{10}–DNF–VV.
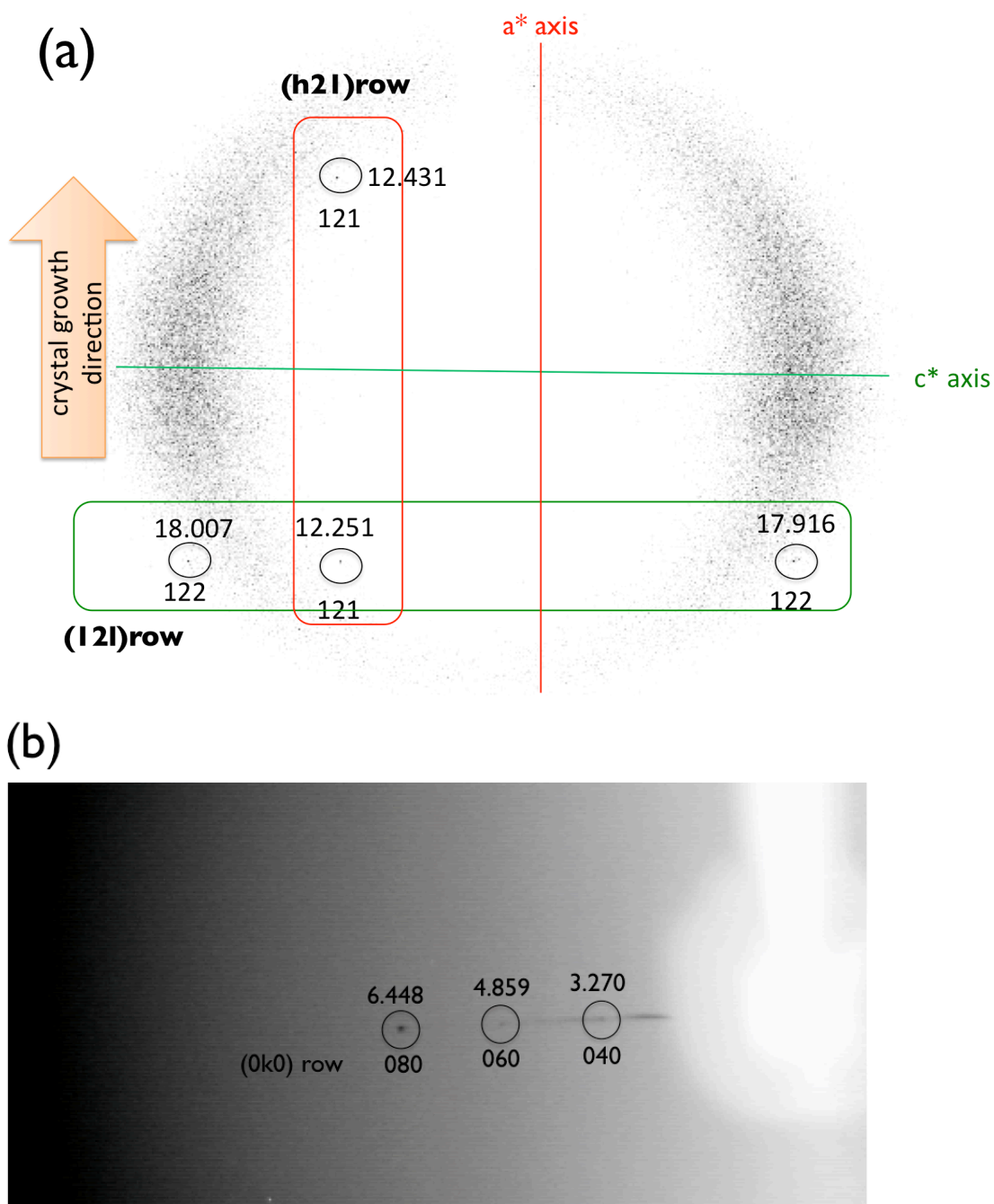
Figure 50. Laue spots of solution-crystallized **C₁₀–DNF–VV** thin film on imaging plate in (a) in-plane and (b) out-of-plane measurements.

The out-of-plane transmission XRD measurements suggest that the b^*-axis, corresponding to the molecular long axis, is perpendicular to the substrate in each compound. Additionally, the in-plane XRD measurements show that the crystal growth direction is parallel to the a-axis, as shown in *Figure 51*. The crystal packing structure

has negligible molecular displacement, as mentioned in Chapter 2, therefore **DNF–V** derivatives exhibit high FET performance of over 1.0 cm^2 V^{-1} s^{-1}, regardless of the positions of substituents.
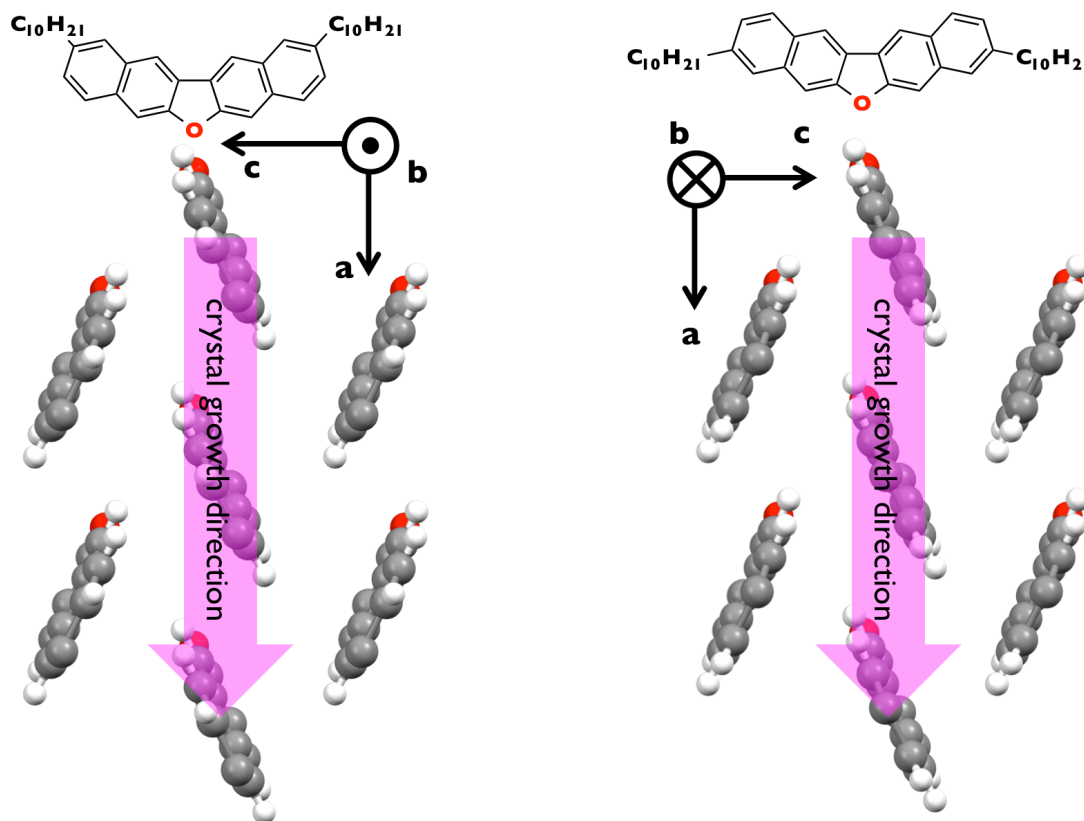
Figure 51. Schematic diagram of relationships between aggregated structure and crystal growth (channel) direction. Left: **C$_{10}$–DNF–VV**, right, **C$_{10}$–DNF–VW**.

In contrast, **DNF–W** stacking is anisotropic (Figure 52). The one-dimensional structure includes discontinuities arising from natural disorder. The charge transport ability is therefore limited by the resistance at molecular disconnections. **DNF–W** therefore exhibited values smaller by two orders of magnitude than those for **DNF–V** derivatives.
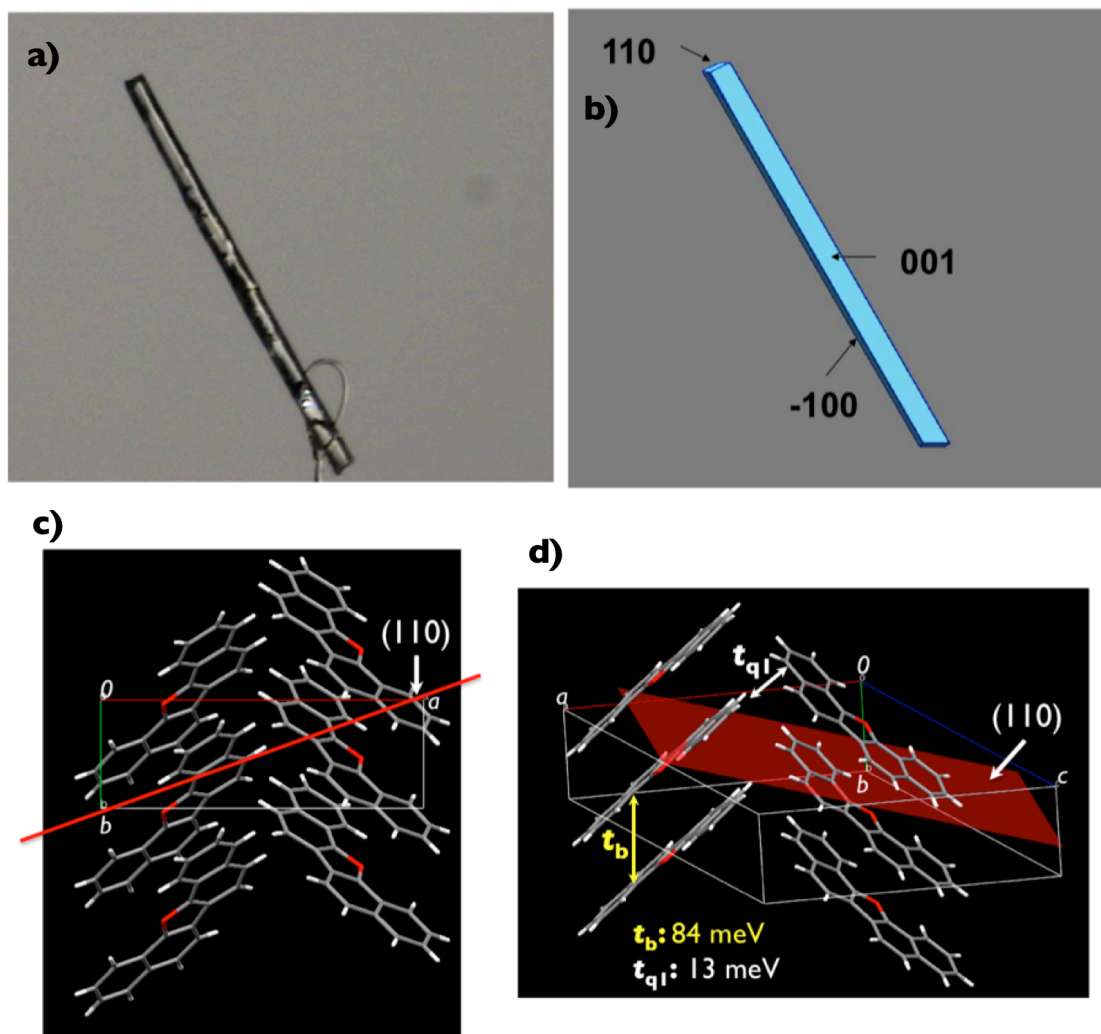
Figure 52. a) Photograph of **DNF–W**, b) its face index, and c) and d) packing structure with (110) plane and transfer integrals.[31]

3.4 Conclusion

In this chapter, the author described the use of **DNF–V** derivatives as organic semiconducting materials. The C_n**–DNF–VW** framework is particularly favorable for OTFT devices. Among these, C_6**–DNF–VW** showed a very high hole mobility of 1.61 cm^2 V^{-1} s^{-1}.

Evaluation of the intrinsic charge carrier mobility using single-crystal FETs clarified that **DNF–V**, C_{10}**–DNF–VW**, and C_{10}**–DNF–VV** crystalline thin films exhibited high hole mobilities of over 1 cm^2 V^{-1} s^{-1}, regardless of the substituent positions, because molecular displacement was negligible. Although large hysteresis

was observed in each as-fabricated device, this issue was resolved by removing trap sites such as oxygen and water by washing with a polar solvent. In sharp contrast, **DNF–W**, whose packing structure is one dimensional, exhibited a hole mobility of 10^{-2} cm^2 V^{-1} s^{-1}. These results show that the C_n**–DNF–VW** framework is the most favorable among oxygen-bridged π-electronic organic semiconductors. Furthermore, in photophysical measurements, C_6**–DNF–VW** and C_{10}**–DNF–VW** showed deep-blue emissions with high quantum efficiencies in the solid state. C_n**–DNF–VW** compounds are therefore promising candidates for the development of blue-light-emitting organic semiconducting devices.

Chapter 4

Investigation of U-Shaped Organic Semiconductors with Twisted π-Electronic Systems (Furan- vs. Thiophene-Containing Semiconductors)

4.1 Introduction

As described in Chapters 2 and 3, oxygen-bridged organic semiconducting materials with bent structures have potential applications in organic electronic devices. The fundamental properties such as solubility, phase-transition temperature, and optical properties of a series of **DNF–V** derivatives were modified by changing the alkyl chain lengths or substituent positions on the **DNF–V** core. In contrast, **DNF–W** forms a π–π-stacked aggregated structure in a single crystal. These results indicated that the bridging positions of oxygen atoms in binaphthalene isomers dramatically change the aggregated structures and carrier transport properties. However, **DNF–W** was more soluble than **DNF–V** derivatives in common organic solvents at room temperature (e.g., 1.6 wt% in chloroform). These results indicate that modifying the central π-core might lead to previously unknown solid-state properties. The author therefore focused on the third structural isomer of a chalcogen-bridged binaphthalene compound, a U-shaped material. In this chapter, the author describes twisted and oxygen- or sulfur-atom containing π-extended materials, dinaphtho[2,1-*b*:1′,2′-*d*]furan (**DNF–U**) and dinaphtho[2,1-*b*:1′,2′-*d*]thiophene (**DNT–U**) as new organic semiconducting materials (*Figure 53*). The intrinsic hole mobilities of **DNF–U** and **DNT–U** were well demonstrated by applications to single-crystal FETs.

DNF–U   DNT–U
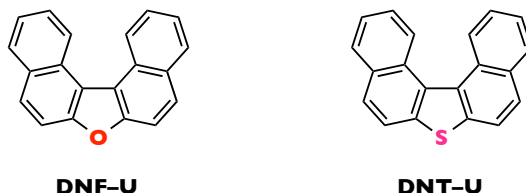
Figure 53. Molecular structures of **DNF–U** and **DNT–U**.

First, the author carried out DFT calculation on **DNF–U** and **DNT–U** at the B3LYP/6-31* level, as illustrated in *Figure 54*. The calculation revealed that 1) U-shaped molecules have a unique twisted structure, because of the presence of steric hindrance between the two internal protons on the naphthalene rings; 2) the π-electron in the highest occupied molecular orbital (HOMO) is well delocalized on the external sides of two naphthalene rings, without losing π-electron conjugation; and 3) the calculated HOMO energy levels of **DNF–U** and **DNT–U** were –5.34 eV and –5.42 eV, respectively, suggesting that this material is a promising candidate for an air-stable p-type organic semiconductor. In this chapter, the author describes and proves the

potential of a new class of organic semiconductors with highly soluble, twisted π-core structures. To demonstrate the intrinsic carrier mobility, the author evaluates an organic single-crystal field-effect transistor performance.
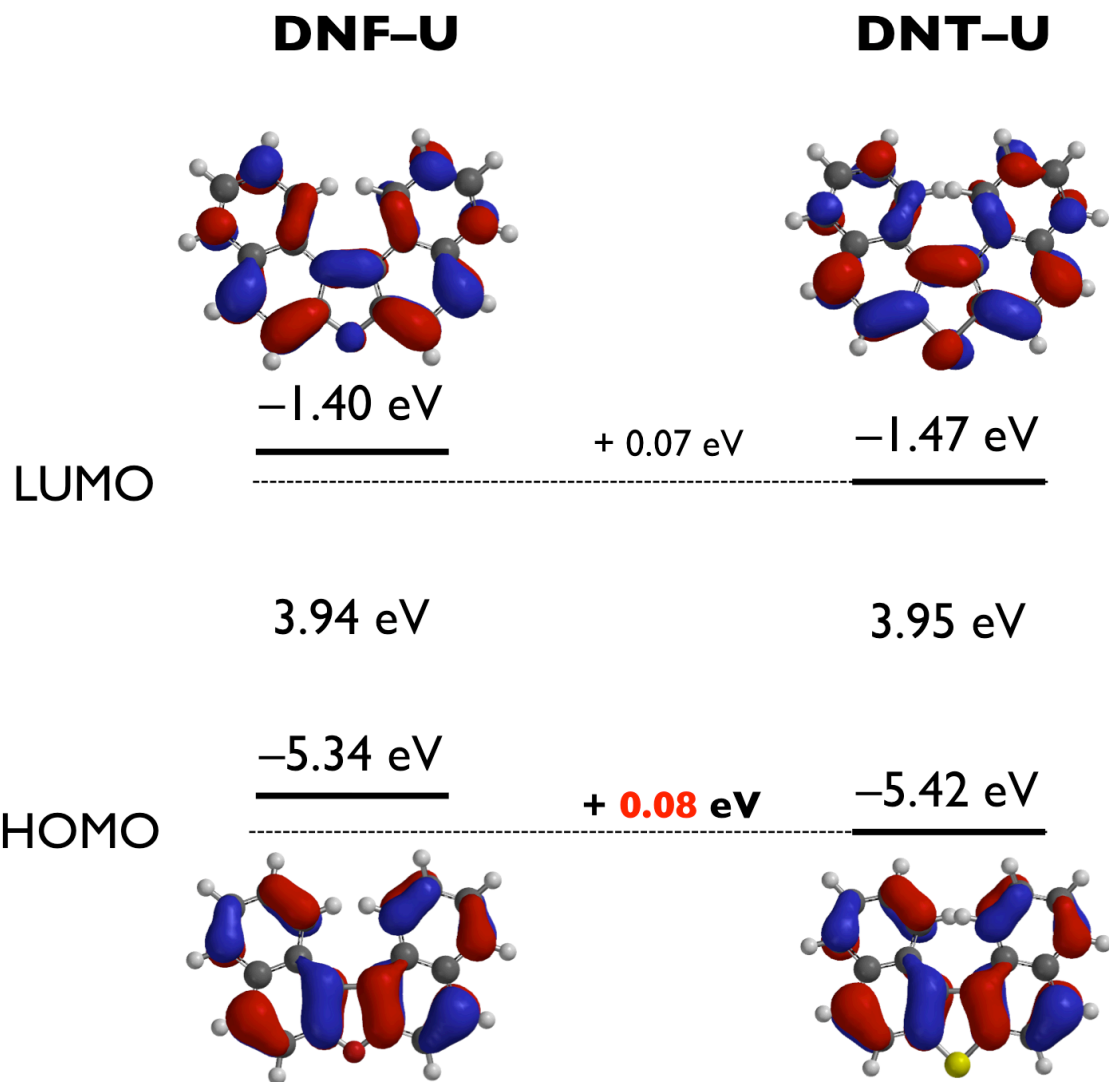
Figure 54. Frontier molecular orbitals of **DNF–U** and **DNT–U**, calculated at B3LYP/6-31G* level using Spartan '04.

4.2 Synthesis

Motivated by a DFT study, the author synthesized **DNF–U** from 1′-bi-2-naphthol (**BINOL**), which is commercially available and inexpensive, as the starting material, using the literature procedure, in which this molecule is synthesized by a simple and quantitative dehydration reaction in the presence of a zeolite catalyst (Scheme 5).[33] Notably, **DNF–U** is highly soluble in common organic solvents; a comparison of the

solubilities of **DNF–U**, **DNF–V**, and **DNF–W** is given in *Table 9*. **DNF–U** has extremely high solubility in chloroform owing to the twisted structure, as discussed below in detail.

Scheme 5. Synthetic scheme for **DNF–U**
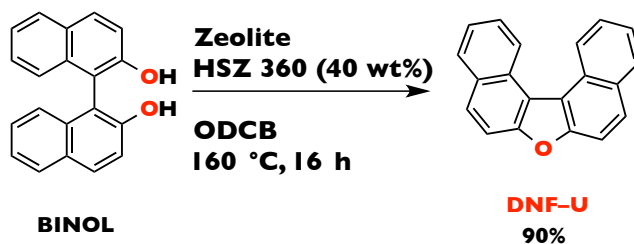
Table 9. Solubilities of oxygen-bridged binaphthalene isomers in chloroform at room temperature

Compound	Solubility (wt%)
DNF–U	6.4
DNF–V	< 0.1
DNF–W	1.6

DNT–U was also synthesized via the literature procedure (Scheme 6).[60] 1,1′-Binaphthyl-2,2′-diyl-*O*,*O*-bis(*N*,*N*-dimethylthiocarbamate),[61] prepared from **BINOL**, smoothly underwent thiophene-ring formation under heating via a Newman–Kwart rearrangement. The solubility of **DNT–U** in chloroform was 0.73 wt%.

Scheme 6. Synthetic scheme **for DNT–U**
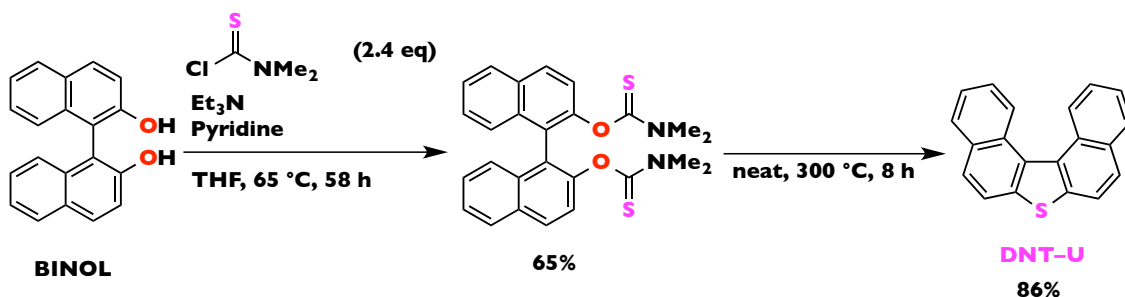
Additionally, the author hypothesized that the zeolite catalyst might also be useful

for constructing dibenzothiophene, the sulfur-containing congener. The author therefore examined the limitations of zeolite use in the conversion of binaphthalenedithiol to dinaphthothiophene. The author synthesized 1,1′-binaphthalene-2,2′-dithiol as the starting material according to the literature procedure (Scheme 7), i.e., by reduction via a Newman–Kwart rearrangement.[62]

Scheme 7. Synthesis of 1,1′-binaphthalene-2,2′-dithiol
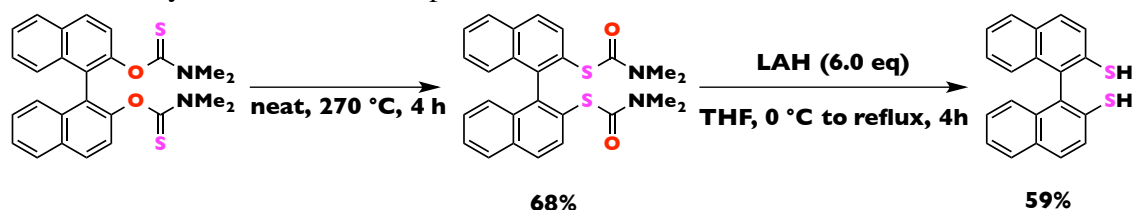
The author then investigated the synthesis of **DNT–U** using a zeolite catalyst (Scheme 8). This is the first time that a zeolite catalyst has proven to be effective in constructing dibenzofuran and dibenzothiophene frameworks from the corresponding substrates, indicating the versatility of this catalyst.

Scheme 8. Synthesis of **DNT–U** from 1,1′-binaphthalene-2,2′-dithiol, promoted by zeolite catalyst
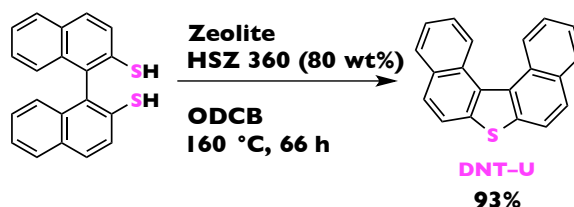
Further functionalization of the U-shaped molecules was performed by bromination, to afford the synthetic module dibromodinaphtho[2,1-*b*:1′2-*d*]furan (**DBrDNF–U**) (Scheme 9). The brominated positions were unambiguously determined using the nuclear Overhauser effect (NOE), because the ^{1}H NMR spectra show that there are two possible bromination positions on **DNF–U**. As shown in the bottom part of *Figure 55*, when the proton at 8.19 ppm was irradiated, there was no correlation with other protons, suggesting that the brominated positions were the 5,9-positions.

Scheme 9. Dibromination of **DNF–U**

Br₂ (2.1 eq)

AcOH, 80 °C, 4h

80%

Irradiation on H$_a$ (δ = 8.19, singlet)

1 No correlation

2 Correlation with H$_b$
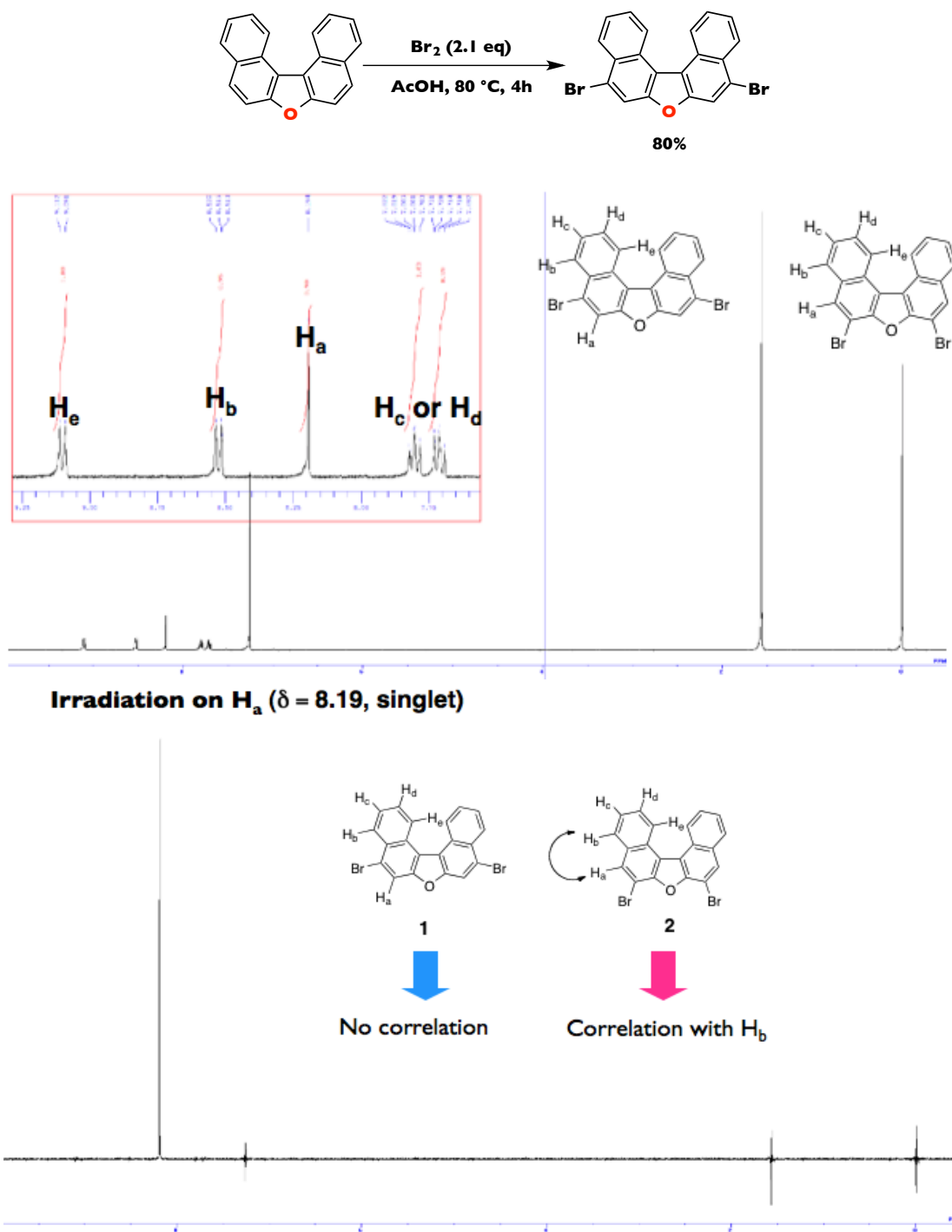
Figure 55. Structural determination of **DBrDNF–U**. Top: NMR spectrum of **DBrDNF–U**. Bottom: NOE chart (irradiation of δ = 8.19, singlet).

Starting from the dibrominated precursor, various **DNF–U** derivatives were synthesized. First, thienyl, furyl, and thiazolyl groups were introduced by Kosugi–

Migita–Stille coupling, affording the products in high yields (Scheme 10).

Scheme 10. Functionalization of **DNF–U** by Kosugi–Migita–Stille coupling
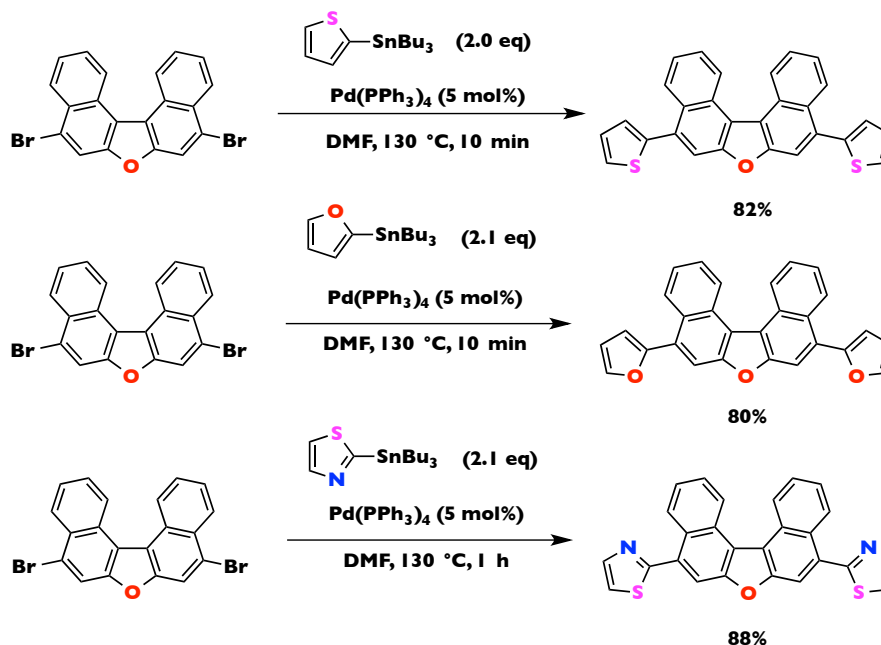
Quinoidal **DNF–U** was also synthesized by oxidation of the dianion intermediate (Scheme11).[63,64]

Scheme 11. Synthesis of quinoidal **DNF–U**
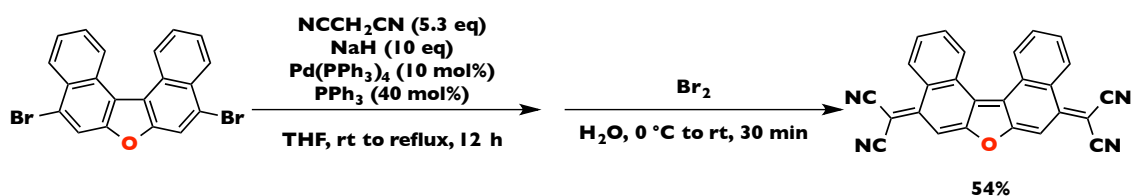
Next, the author carried out alkylation of the **DNF–U** core using the Kumada–Tamao–Corriu cross-coupling reaction, but the debrominated mono-alkylated byproduct was also obtained when NiCl$_2$(dppp) was used as the catalyst. To suppress byproduct formation, catalyst screening was carried out (*Table 10*). PdCl$_2$(dppf) was found to be the most suitable catalyst for the alkylation reaction. Octyl groups were also introduced under these reaction conditions (Scheme 12).

Table 10. Catalyst screening for alkylation of **DNF–U** core

Catalyst	**C$_{12}$–DNF–U**	**Byproduct**
NiCl$_2$(dppp)	50%	50%
PdCl$_2$(dppp)	No reaction	
PdCl$_2$(dppf)	83%	17%

Yields were determined by ^{1}H NMR.

Scheme 12. Synthesis of alkyl-**DNF–U**
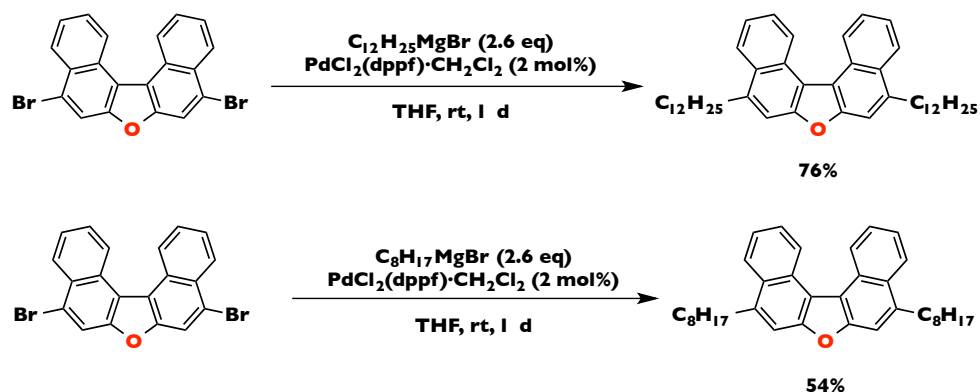
4.3 Electrochemical Properties

The HOMO energy levels were estimated by determining the oxidation potential by electrochemical measurements using cyclic voltammetry (CV) and differential pulse voltammetry (DPV). The cyclic voltammograms of the compounds showed irreversible oxidation waves. The HOMO levels were therefore estimated from the DPV charts. As shown in *Figure 56*, the DPV charts suggested that the oxidation potentials of **DNF–U** and **DNT–U** are +0.91 V and 0.07 V (vs. Fc/Fc$^+$), from which the HOMO energy levels are estimated to be –5.71 eV and –5.77 eV, respectively, using the equation, $E_{HOMO} = -(4.80 + E_{DPV})$.[65] The estimated HOMO energy levels are slightly deep, but applicable to p-type materials.
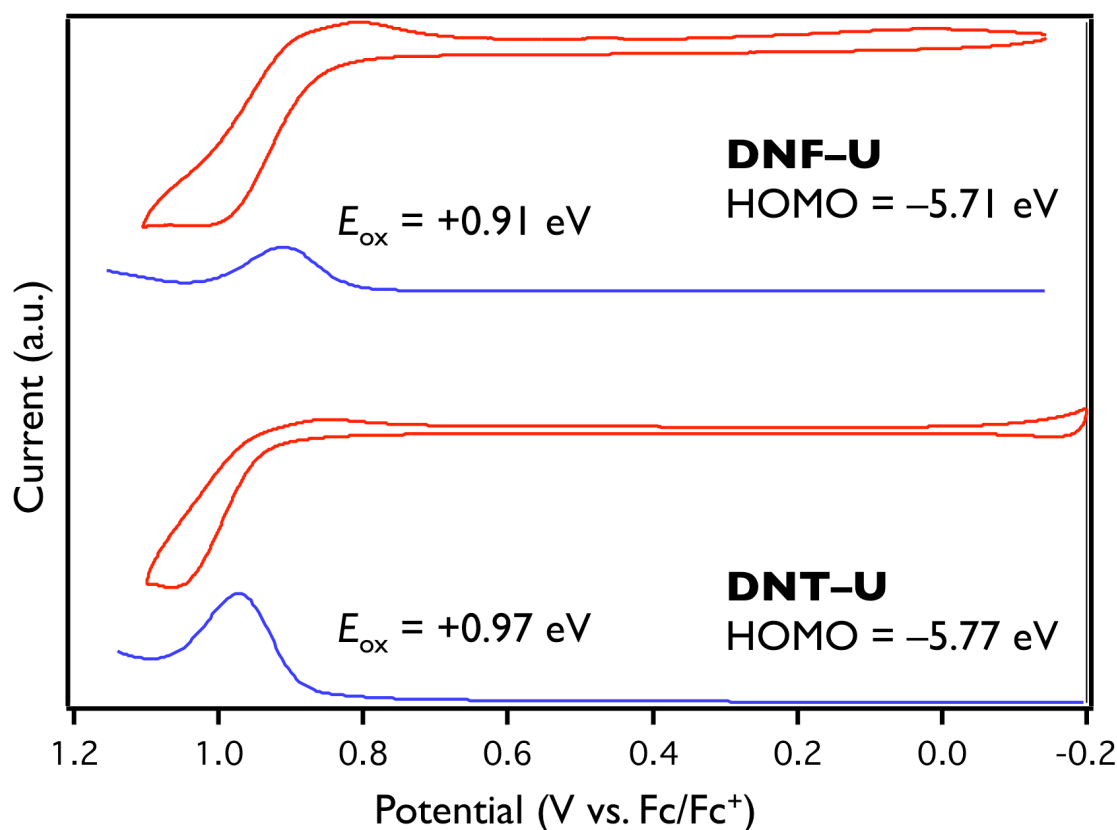
Figure 56. CV (red line) and DPV (blue line) charts of **DNF–U** (top) and **DNT–U** (bottom). Measurements were carried out at a scan rate of 100 mV s^{-1} in dichloromethane (1.0 mM) using n-Bu$_4$NPF$_6$ (0.1 M) as the supporting electrolyte.

4.4 Thermal Stability

Thermogravimetric and differential thermal analysis (TG-DTA) measurements revealed that **DNF–U** and **DNT–U** were completely evaporated after melting at 159 °C and 205 °C, respectively, without thermal decomposition, under a stream of N$_2$ gas (*Figure 57*). The 5% weight loss temperatures ($T_{95\%}$) of **DNF–U** and **DNT–U** were 249 °C and 259 °C, respectively. The high thermal stabilities of these materials enabled us to prepare vapor-grown single crystals by physical vapor transport (PVT).[9,54,55]
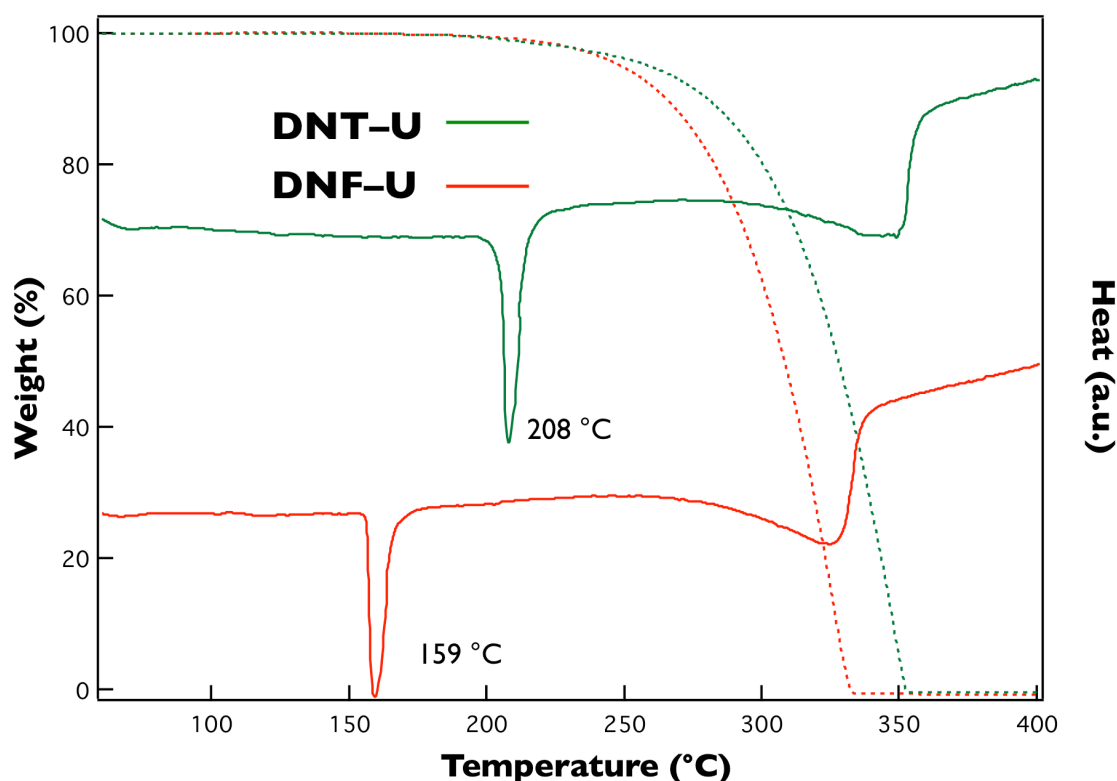
Figure 57. TG-DTA charts of **DNT–U** (green) and **DNF–U** (red). Dotted and solid lines represent TGA and DTA, respectively. Heating rate: 5 K min^{-1}, N$_2$ gas flow rate: 100 mL min^{-1}, reference: Al$_2$O$_3$.

4.5 Optical Properties

The UV-vis absorption spectra of **DNF–U** and **DNT–U** were measured in chloroform. The wavelengths of the absorption maxima and onset of the two compounds were almost the same (*Figure 58*). The central chalcogen atom did not significantly affect the absorption properties. In sharp contrast, high fluorescence quantum yields were obtained for **DNF–U**, and it exhibited a solid-state fluorescence quantum yield of 70%. As shown by the data in *Table 11*, the non-radiative decay constant from the singlet excited states of **DNT–U** is dominant both in solution and in the solid, because of the presence of spin–orbit coupling in the thiophene-containing compound. **DNF–U** and **DNT–U** both showed higher fluorescence quantum yields in the solid than in solution. This might be because of inhibition of molecular fluctuations in the solid state.
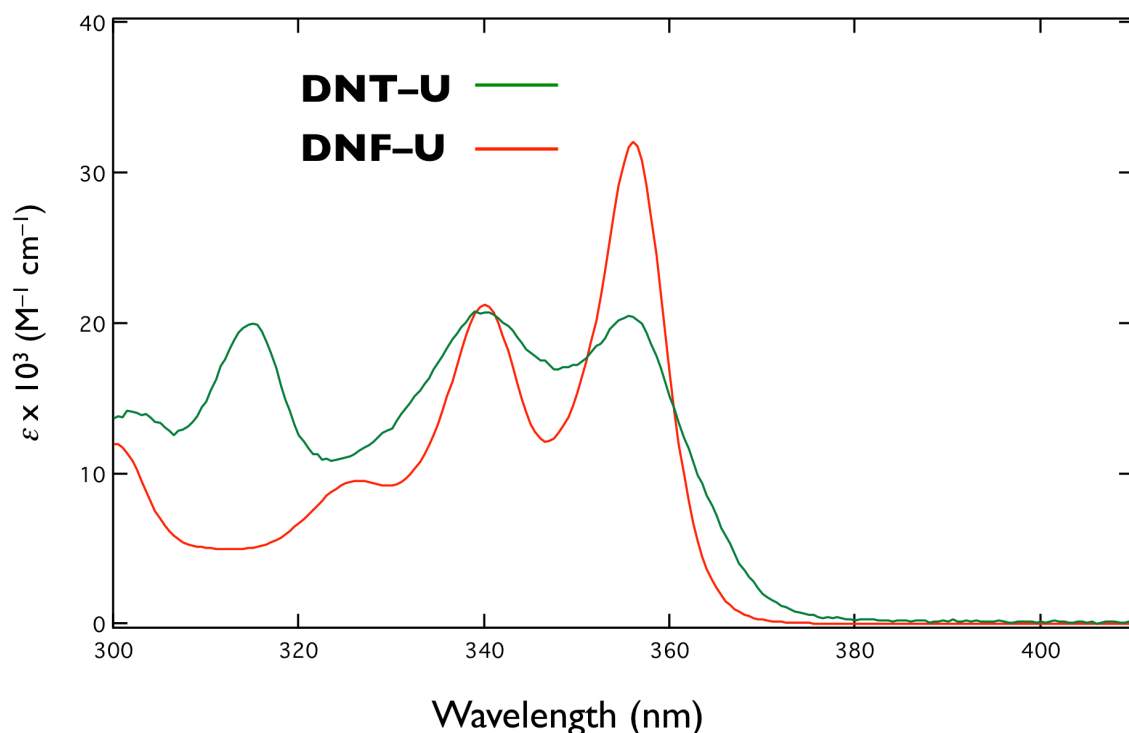
Figure 58. Absorption spectra of **DNF–U** (red) and **DNT–U** (green) in chloroform. (**DNF–U**: $C = 1.4 \times 10^{-5}$ M, **DNT–U**: $C = 7.3 \times 10^{-6}$ M).

Table 11. Fluorescence quantum yields, lifetimes, and photoluminescence rate constants of U-shaped materials

Compound	Solution (in chloroform)				Solid			
	Φ_f	τ (ns)	k_f ($\times 10^7$ s^{-1})[a]	k_{nr} ($\times 10^7$ s^{-1})[a]	Φ_f	τ (ns)	k_f ($\times 10^7$ s^{-1})[a]	k_{nr} ($\times 10^7$ s^{-1})[a]
DNF–U	0.58	2.425	23.9	17.3	0.72	17.415	9.83	4.21
DNT–U	0.01	0.312	3.21	317	0.03	0.538	5.58	180

[a]Radiative and non-radiative decay rate constants were calculated using Φ_f and τ, according to the formulas $k_f = \Phi_f/\tau$ and $k_{nr} = (1-\Phi_f)/\tau$.

4.6 X-Ray Single-Crystal Structural Analysis

Based on the high thermal stabilities of **DNF–U** and **DNT–U** suggested by TG-DTA measurements, the author prepared single crystals by horizontal PVT in a stream of argon gas with flow rates of 30 mL min^{-1} and 50 mL min^{-1}, respectively. In the preparation of the **DNF–U** single crystal, the temperatures of the raw materials and crystal zones were kept at 170 °C and 120 °C, respectively, to produce needle-like

single crystals. In contrast, in the preparation of the **DNT–U** single crystal, the temperatures of the raw materials and crystal zones were kept at 220 °C and 160 °C, respectively, to afford platelet single crystals. The obtained vapor-grown crystals were used for X-ray single-crystal structural analysis. The X-ray single-crystal structural analysis showed molecules with twisted structures, as predicted by the DFT calculations. The molecular torsion angles were 23° for **DNF–U** and 45° for **DNT–U**, as shown in *Figure 59*.

DNF–U   **DNT–U**
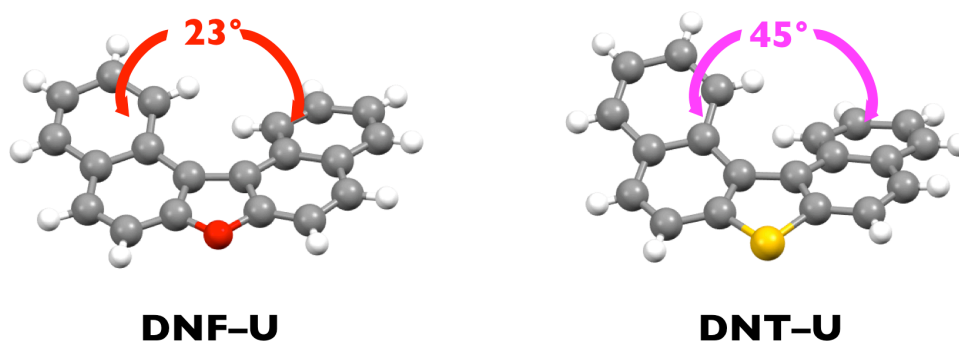
Figure 59. Molecular structures of single crystals of **DNF–U** and **DNT–U**.

Figure 60 shows the molecular arrangement in the conducting plane between the HOMOs of **DNF–U** and **DNT–U** in single crystals. For the single crystal of **DNF–U**, a calculation based on Hückel molecular orbitals affords a transfer integral of 57 meV in the π–π stacking direction of the *a*-axis. Because of the presence of an orbital coefficient on the external naphthalene rings, in the transverse direction of the *b*-axis, **DNF–U** has a transfer integral of 20 meV, which is smaller than that for the stacking direction, but a moderate value. A FET device with the channel direction parallel to the *a*-axis (the π–π stacking direction) could therefore have a high charge carrier mobility. In contrast, **DNT–U** has a large transfer integral of 79 meV only in the π–π stacking direction of the *c*-axis. In the transverse direction of the *a*-axis, the transfer integral is very small (3 meV) because of the ineffective molecular orbital overlap resulting from the one-dimensional columnar face-to-face π-stacking structure.

DNF–U

$t_a = 57$ meV
$t_q = 20$ meV

DNT–U

$t_a = 3$ meV
$t_c = 79$ meV
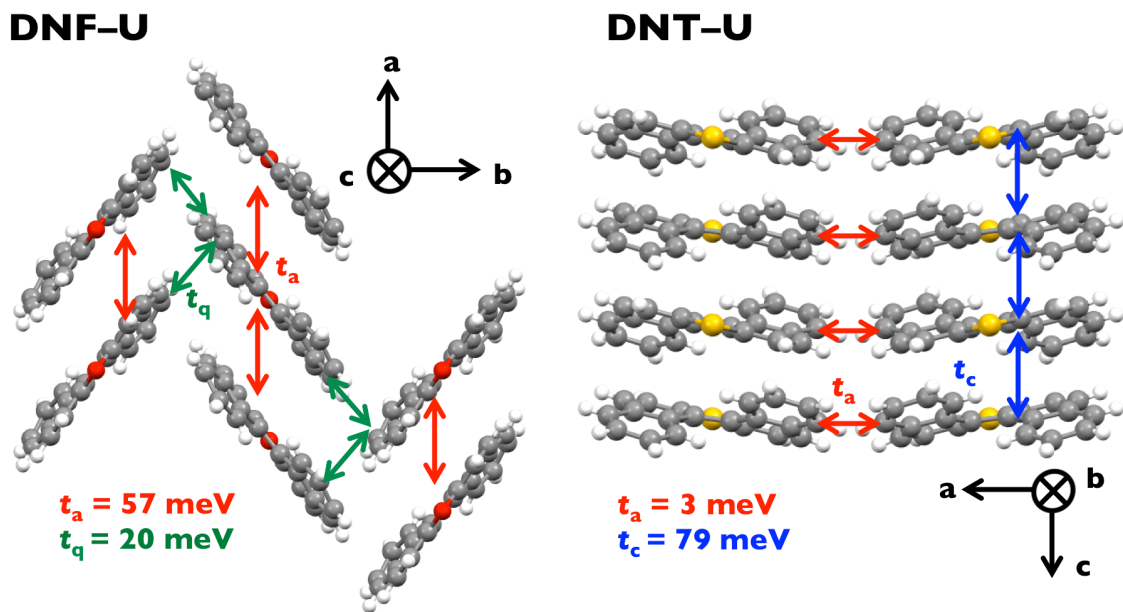
Figure 60. Packing structures of **DNF–U** (left) and **DNT–U** (right), with calculated transfer integrals.

4.7 Evaluation of Hole Mobility in Single-Crystalline Film

In order to evaluate the intrinsic carrier-transporting capabilities of **DNF–U** and **DNT–U**, the author fabricated single-crystal FETs. Since the FET characteristics of organic single crystals are not greatly affected by extrinsic influences such as impurities, grain boundaries, and defects in the channel region, which are often problems with polycrystalline thin films, single-crystal FETs well demonstrate the intrinsic carrier-transporting properties of organic materials.[66]

First, the author used the top-gate–top-contact architecture to fabricate a single-crystal FET using **DNF–U**, as shown in *Figure 61* (a). Good needle-like crystals prepared by PVT were selected, and the FET structure was constructed on a glass substrate. Source and drain electrodes were pasted on top of the crystal using carbon paste. A parylene gate dielectric[53,59] was then formed to a thickness of 1.3 μm, using a laboratory-made reactor. Finally, a gate electrode was painted on the parylene gate dielectric to cover the whole region between the source and drain electrodes. The transfer and output characteristics of the device were both measured under ambient conditions using a Keithley 4200 semiconductor parameter analyzer.
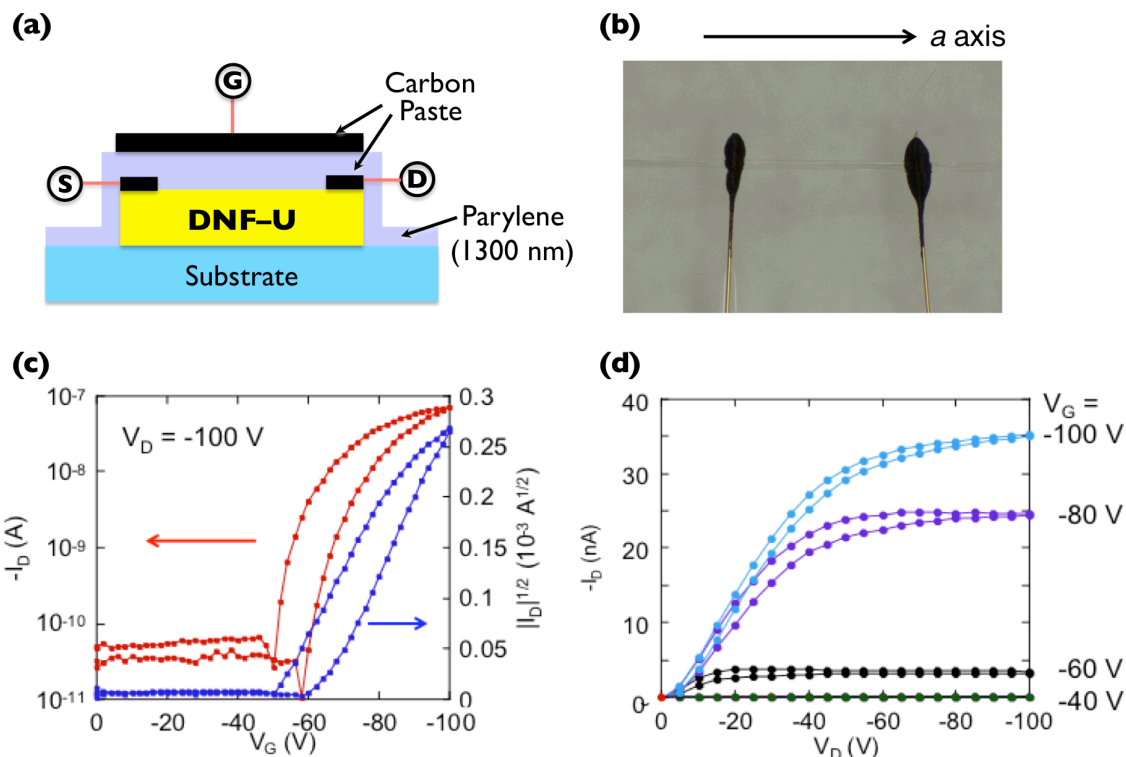
Figure 61. (a) Device configuration, (b) photograph of **DNF–U** single crystal, and (c) transfer and (d) output characteristics.

Figure 61 (c) and (d) show typical transfer and output characteristics of the single-crystal FET; it has p-type behavior with a good I_{on}/I_{off} ratio of 10^4. The saturation of the drain currents in the output characteristics enables us to evaluate its carrier mobility from the slopes in the transfer curve. The maximum value of the mobility is 1.0 cm^2 V^{-1} s^{-1}. XRD analysis of the single crystal used for the FET device showed that the channel direction of the best-performance device was parallel to the π–π stacking direction (*a*-axis), suggesting that the mobility demonstrated in this study well reflected its intrinsic hole mobility (*Figure 62*). The non-negligible threshold voltage probably resulted partially from traps in the gap between the work function of the carbon paste electrodes and the deep HOMO level of **DNF–U**. This injection barrier could be reduced by use of a strong electron acceptor or large work function electrode.[67]
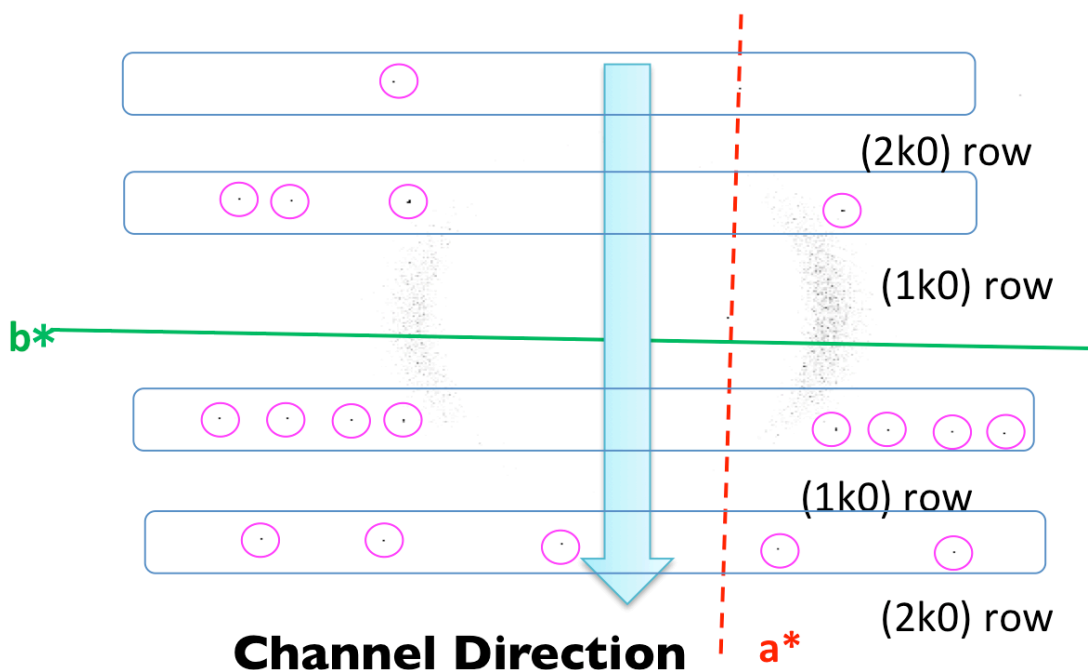
Figure 62. Laue spots of laminated **DNF–U** single crystal on imaging plate in in-plane measurements.

Secondly, the author fabricated FETs with bottom-gate–bottom-contact architectures, using single crystals of **DNT–U**, and evaluated the device characteristics (*Figure 63*). The platelet single crystals obtained by PVT were manually laminated on an F-DTS-treated SiO_2 (thickness: 500 nm) substrate with patterned gold electrodes. The transfer and output characteristics of the **DNT–U** single-crystal FETs are shown in *Figure 63* (a) and (b). Single-crystal devices based on **DNT–U** showed a maximum hole mobility of 0.15 cm^2 V^{-1} s^{-1}. Transmission XRD analysis of the **DNT–U** single crystal used for the FETs showed that the channel direction was parallel to the π–π stacking direction of the *c*-axis in the best-performance device (*Figure 64*), suggesting that the mobility demonstrated in this study well reflected its intrinsic hole mobility. Although the large transfer integral in the channel direction of the *c*-axis was calculated to be 79 meV, the hole mobility was not so high. The reduction in charge transport might be due to statistical disorder and the influence of neighboring molecules with low transfer integrals in the direction of the *a*-axis, which is perpendicular to the one-dimensional stacking direction.[68,69]

(a)

Au(30 nm)/Cr(2 nm)

FDTS-SAM

DNT-U

SiO$_2$ (500 nm)

doped Si (Gate)

F$_3$C
CF$_2$
F$_2$C
CF$_2$
F$_2$C
CF$_2$
F$_2$C
CF$_2$
F$_2$C
CF$_2$

EtO — Si — OEt
OEt

(b)

c axis

(c)

$V_D = -100$ V

$-I_D$ (A)

$|I_D|^{1/2}$ (10^{-3} A$^{1/2}$)

V_G (V)

(d)

$-I_D$ (μA)

V_G = -100 V

-80 V

-60 V

-40 V

20 V, 0 V

V_D (V)

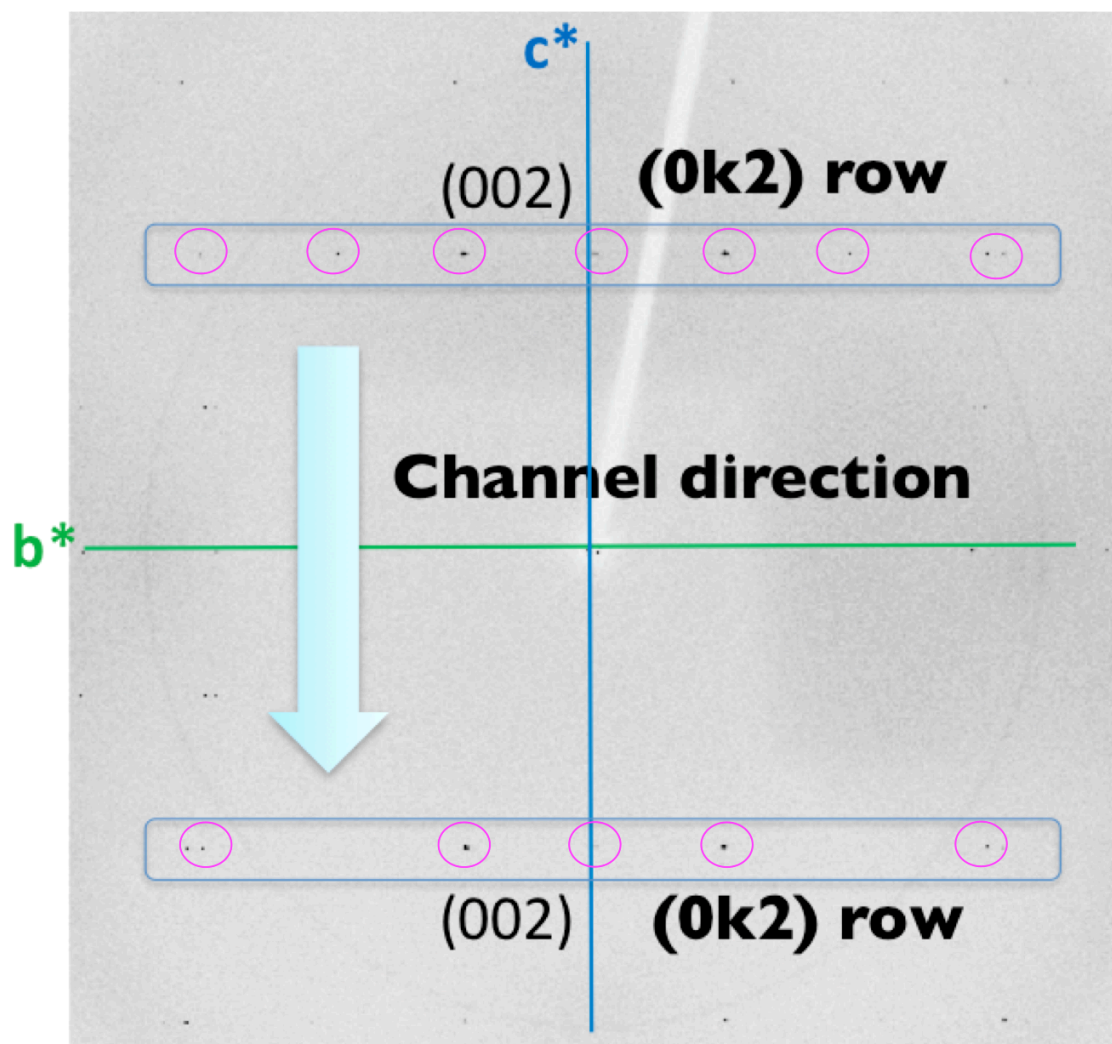*Figure 63.* (a) Device configuration, (b) photograph of **DNT–U** single crystal, and (c) transfer and (d) output characteristics.

Figure 64. Laue spots of laminated **DNT–U** single crystal on imaging plate in in-plane measurements.

For comparison with single-crystal devices, the author also examined vacuum-deposited thin-film transistors using **DNF–U** and **DNT–U**, as shown in *Figure 65* (a). These semiconducting materials were vacuum deposited on the DTS-treated SiO_2 substrate at a nominal thickness of 75 nm, indicated using a quartz film thickness meter at room temperature. F_4-TCNQ and gold electrodes were successively deposited on top of the semiconducting film through a shadow mask. F_4-TCNQ was used as a strong acceptor to reduce the metal/organic interface resistance between the semiconductor and the gold electrodes. The transfer and output characteristics of the devices were both measured under ambient conditions. However, no FET character was observed for the **DNF–U**-based device. AFM measurements indicated that a

polycrystalline film of **DNF–U** was not formed on the substrate, probably because of the formation of amorphous morphology. On the contrary, the **DNT–U**-based FET exhibited a typical p-type transistor behavior. *Figure 65* (c) and (d) illustrate the transfer and output characteristics. The estimated hole mobility of **DNT–U** in the thin film ranged from 1.4×10^{-2} to 2.2×10^{-2} cm^2 V^{-1} s^{-1}, and the threshold voltage was as high as –67 V, as a resulting of the deep HOMO energy level of **DNT–U**. An AFM image of the **DNT–U** thin film shows that this material formed large grains of size over 1 μm, with a three-dimensional island structure, as shown in *Figure 65* (b). Despite the nominal thickness of 75 nm, the grain islands are as high as 150 nm, indicating poor film connectivity in the channels, therefore the intrinsic mobility could not be fully evaluated.
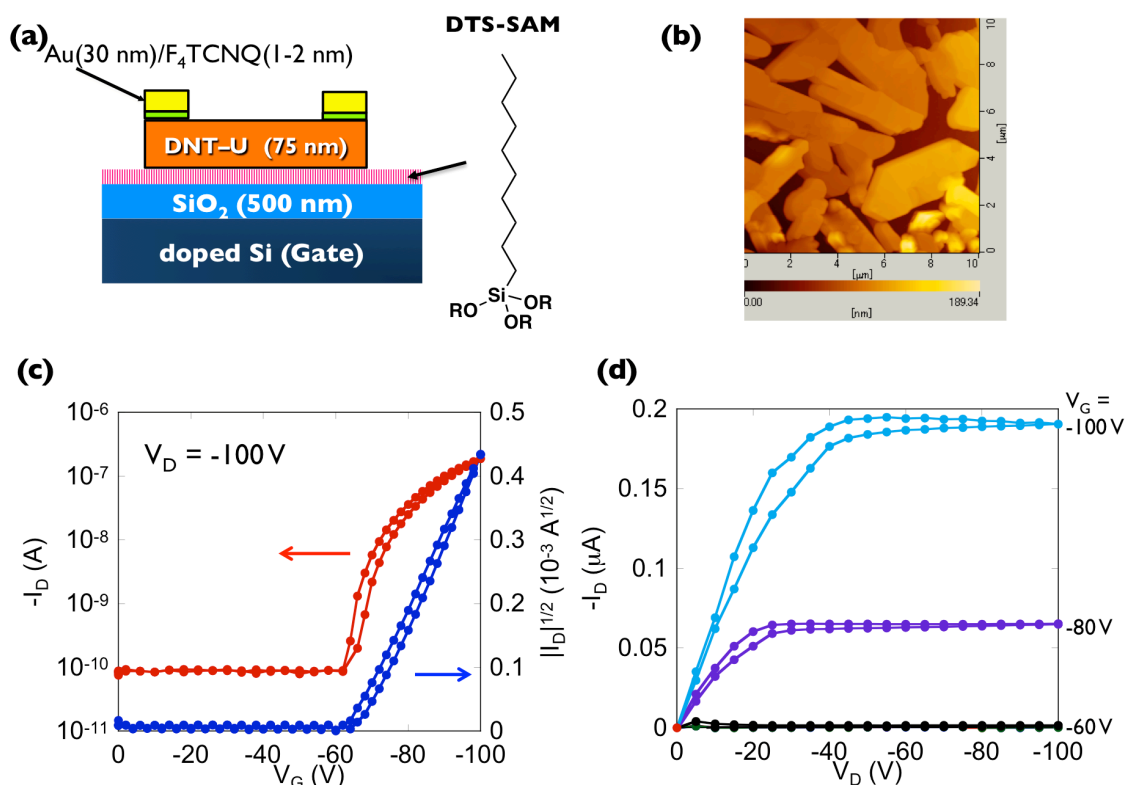
Figure 65. (a) Thin-film device structure, (b) AFM image, and (c) transfer and (d) output characteristics. Top-contact–bottom-gate configuration with *L/W* = 9/20.

Thin-film transistors based on unsubstituted **DNF–U** showed no field effect, as stated above, so thin films of **DNF–U** derivatives with appropriate substituents were prepared using a solution process. The author first fabricated an OTFT device using **C$_{12}$–DNF–U** on a DTS-treated substrate, demonstrating the possibility of using **DNF–U**

derivatives in solution-processed OFETs with hole mobilities of 10^{-3} cm^2 V^{-1} s^{-1}, as shown in *Figure 66*.
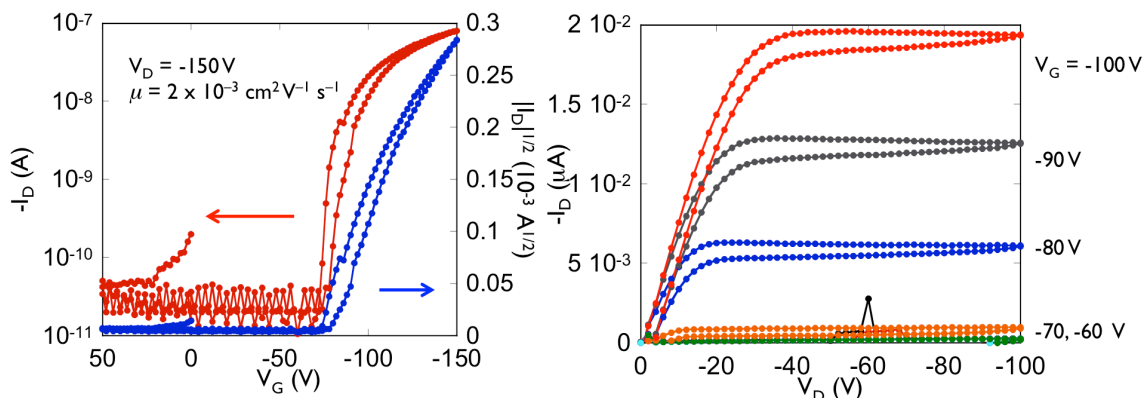
Figure 66. Hole transport properties of **C$_{12}$–DNF–U** in thin-film on DTS-treated SiO$_2$ (500 nm) substrate. Left: transfer curve, right: output curve. Top-contact–bottom-gate configuration with *L/W* = 1/5

4.8 Conclusion

In this chapter, the author described the intrinsic carrier transport abilities of **DNF–U** and **DNT–U**, using their single crystals. Transmission XRD analysis of the single crystal of the best-performance device showed that the channel was parallel to the π–π stacking direction, suggesting that the mobility demonstrated in this chapter well reflects the intrinsic hole mobility. It was revealed that **DNF–U**, whose aggregated structure is two-dimensionally isotropic, showed a value 10 times higher than of **DNT–U**, and had one-dimensional face-to-face packing in the single crystal. Because the size of the molecular torsion angle varies depending on the van der Waals radius of the central chalcogen atom in this U-shaped core structure, the introduction of a series of chalcogen atoms could control the solubilities, packing structures, and device performances. Furthermore, **DNF–U** might be a promising material in research on single-crystal organic electronic devices because **DNF–U** has very high solubility and a high photoluminescence quantum yield in the solid state. Additionally, the author showed the versatility of a zeolite catalyst by constructing furan as well as thiophene rings. This might be promising for the synthesis of more comprehensive organic semiconductors containing fused furan and thiophene moieties. The author also synthesized **DNF–U** derivatives, starting from dibrominated **DNF–U** as a synthetic module. Among the **DNF–U** derivatives, alkylated **DNF–U** can be used in solution

97

processes and showed semiconducting characteristics in thin films.

Experimental Section

Reagents and Starting Materials

Tetrakis(triphenylphosphine)palladium(0), tributyl(2-thienyl)tin, and tributyl(2-furyl)tin were purchased from TCI. All Grignard reagents, tributyl(2-thiazolyl)tin, 1,1′-bis(diphenylphosphino)ferrocene–palladium(II)dichloride–dichloromethane adduct, and malononitrile were purchased from Sigma-Aldrich Inc. Bromine, acetic acid, and triphenylphosphine were purchased from Wako Pure Chemical Industries Ltd. Sodium hydroxide and all anhydrous solvents were purchased from Kanto chemicals. Zeolite HSZ-360 was purchased from the Tosoh Corp.

General Methods of Synthesis and Characterization

All the reactions were carried out under a N_2 atmosphere. Air- or moisture-sensitive liquids and solutions were transferred via a syringe or a Teflon cannula. Analytical thin-layer chromatography (TLC) was performed on glass plates with 0.25 mm 230–400-mesh silica gel containing a fluorescent indicator (Merck Silica gel 60 F254). TLC plates were visualized by exposure to a UV lamp (254 nm and 365 nm) and by dipping in 10% phosphomolybdic acid in ethanol and heating on a hot plate. Flash column chromatography was performed on Kanto silica gel 60. Open-column chromatography was performed on Wakogel C-200 (75–150 μm). All NMR spectra were recorded using JEOL ECA600 and JEOL ECS400 spectrometers. Chemical shifts are reported in parts per million (ppm, δ scale) from residual protons in deuterated solvents for ^{1}H NMR (δ 7.26 ppm for chloroform and δ 5.93 ppm for 1,1,2,2-tetrachloroethane) and from the solvent carbon for ^{13}C NMR (δ 77.16 ppm for chloroform and δ 74.00 ppm for 1,1,2,2-tetrachloroethane). The data are presented in the following format: chemical shift, multiplicity (s = singlet, d = doublet, t = triplet, m = multiplet), coupling constant in hertz (Hz), signal area integration in natural numbers, and assignment (*italic*). Mass spectra were measured using a JEOL JMS-T100LC APCI/ESI mass spectrometer. Melting points and elemental analyses were performed using a Mettler Toledo MP70 melting point system and J-Science Lab JM10 MICRO CORDER, respectively. CV and DPV were conducted using a BAS electrochemical analyzer (ALS 622D) using a three-electrode cell with Pt as the working electrode, a Pt wire as the counter electrode

and 0.01 M Ag/AgNO$_3$ as the reference electrode. The potential was corrected against Fc/Fc$^+$. TG-DTA measurements were carried out using a Rigaku Thermo Plus EVO II TG 8120 instrument. The sample was placed in an aluminum pan and heated at a rate of 5 K min^{-1}, under N$_2$ purging at a flow rate of 100 mL min^{-1}. Al$_2$O$_3$ was used as the reference material. UV-vis absorption spectra were measured using a JASCO V-570 spectrometer. The sample solutions were prepared using degassed, analytical-grade 1,2-dichloroethane. Photoluminescence spectra and absolute quantum yields were obtained using a Hamamatsu Photonics C9920–02 Absolute PL Quantum Yield measurement system. The sample solutions were prepared in degassed, analytical-grade 1,2-dichloroethane. Fluorescence lifetimes were evaluated using a Hamamatsu Photonics Quantaurus-Tau C11367-01 measurement system.

Synthesis of dinaphtho[2,1-*b*:1′,2′-*d*]thiophene (DNT–U) with zeolite catalyst

Zeolite HSZ-360 (40 mg) was added to a solution of 1,1′-binaphthalene-2,2′-dithiol (50 mg, 0.15 mmol) in *o*-DCB (3 mL), and the mixture was stirred for 66 h at 160 °C. After cooling to room temperature, the zeolite was removed by vacuum filtration, and then the mixture was concentrated. The crude product was purified by silica gel column chromatography using chloroform:hexane = 1:1 as the eluent, affording a pale-yellow solid. Yield: 40 mg (93%). ^{1}H NMR (400 MHz, CDCl$_3$): δ 8.89–8.86 (m, 2H, Ar*H*), 8.05–8.03 (m, 2H, Ar*H*), 7.98–7.92 (m, 4H, Ar*H*), 7.60–7.57 (m, 4H, Ar*H*).

Synthesis of DNF–U derivatives

5,9-Dibromodinaphtho[2,1-*b*:1′,2′-*d*]furan (DBrDNF–U)
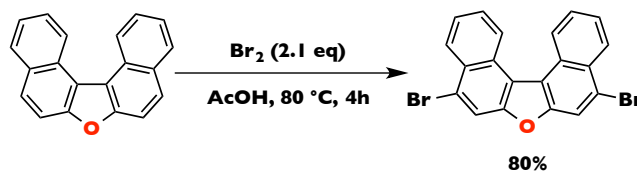
Bromine (6.56 g, 41.05 mmol) was added to a suspension of DNF-U (5.00 g, 18.64 mmol) in acetic acid (100 mL) and the mixture was stirred at 80 °C for 4 h. After cooling to room temperature, the reaction mixture was poured into aqueous sodium hydroxide, and the precipitate was removed by filtration. The crude product was purified by recrystallization from toluene to obtain a white solid. Yield: 6.32 g. ^{1}H NMR (600 MHz, CDCl$_3$): δ 9.09 (d, *J* = 9 Hz, 2H, Ar*H*), 8.52 (d, *J* = 8.4 Hz, 2H, Ar*H*),

8.19 (s, 2H, Ar*H*), 7.80 (t, *J* = 6, 8.4 Hz, 2H, Ar*H*), 7.71 (t, *J* = 8.4, 9 Hz, 2H, Ar*H*). ESI-MS [M + H] *m/z* = 427. Anal. Calcd for $C_{20}H_{10}Br_2O$: C, 56.37; H, 2.37. Found: C, 56.50; H, 2.62.

5,9-Di(2-thienyl)dinaphtho[2,1-*b*:1′,2′-*d*]furan (DTDNF–U)

82%
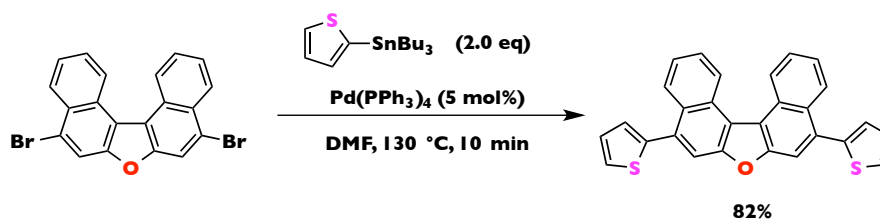
Tributyl(2-thienyl)tin (764 mg, 2.04 mmol) was added to a suspension of **DBrDNF–U** (426 mg, 1.00 mmol) in DMF (10 mL), and the mixture was stirred at 130 °C for 10 min. The resulting solution was cooled to room temperature and poured into aqueous potassium fluoride. After the precipitate was filtered off, the organic layer was extracted with toluene and washed with water and brine. After removal of the solvent, the crude product was filtered through a silica pad using chloroform as the eluent. Finally, the product was purified by GPC using chloroform as the eluent. Yield: 355 mg (82%). [^1]H NMR (600 MHz, $C_2D_2Cl_4$): δ 9.15 (d, *J* = 8.4 Hz, 2H, Ar*H*), 8.41 (d, *J* = 8.4 Hz, 2H, Ar*H*), 7.92 (s, 2H, Ar*H*), 7.76 (d, *J* = 7.2, 7.8 Hz, 2H, Ar*H*), 7.57 (d, *J* = 7.2, 8.4 Hz, 2H, Ar*H*), 7.48 (d, *J* = 4.8 Hz, 2H, Ar*H*), 7.33 (d, *J* = 3.6 Hz, 2H, Ar*H*), 7.23–7.21 (m, 2H, Ar*H*). ESI-MS [M + H] *m/z* = 433. Anal. Calcd for $C_{28}H_{16}OS_2$: C, 77.75; H, 3.73. Found: C, 77.53; H, 3.89.

### 5,9-Di(2-furyl)dinaphtho[2,1-*b*:1′,2′-*d*]furan (DFDNF–U)

80%
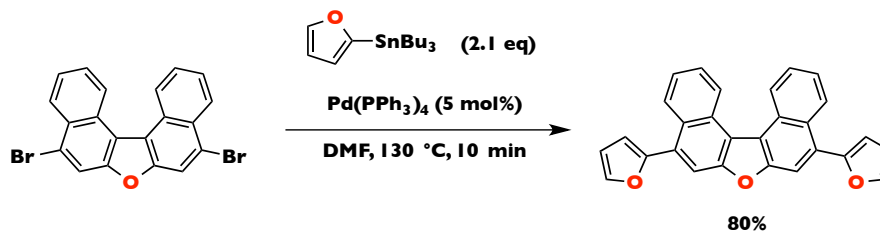
Tributyl(2-furyl)tin (742 mg, 2.08 mmol) was added to a suspension of **DBrDNF–U** (426 mg, 1.00 mmol) in DMF (10 mL), and the mixture was stirred at 130 °C for 10 min. The resulting solution was cooled to room temperature and poured into aqueous potassium fluoride. After the precipitate was filtered off, the organic layer was extracted

with toluene and washed with water and brine. After removal of the solvent, the crude product was filtered through a silica pad using chloroform as the eluent. After removal of the solvent, the crude product was dissolved in chloroform, and then the solution was dispersed in methanol. The obtained pale-yellow solid was filtered through a membrane filter. Yield: 318 mg (80%). ^{1}H NMR (600 MHz, CDCl$_3$): δ 9.20 (d, J = 9 Hz, 2H, ArH), 8.62 (d, J = 8.4 Hz, 2H, ArH), 8.10 (s, 2H, ArH), 7.78 (t, J = 8.4, 7.2 Hz, 2H, ArH), 7.70–7.70 (m, 2H, ArH), 7.64 (t, J = 7.8, 7.2 Hz, 2H, ArH), 6.86 (d, J = 3.6 Hz, 2H, ArH), 6.67–6.66 (m, 2H, ArH). ESI-MS [M + H] m/z = 401.

5,9-Di(2-thiazolyl)dinaphtho[2,1-b:1′,2′-d]furan (DTzDNF–U)
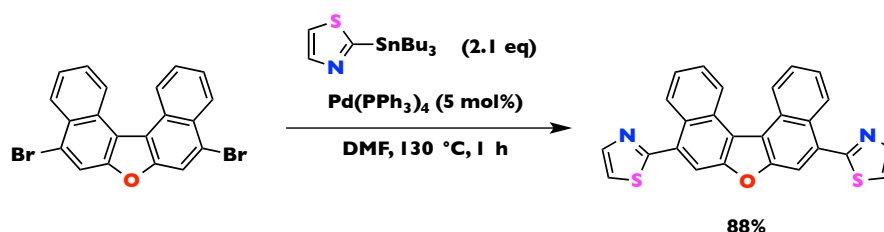
Tributyl(2-thiazolyl)tin (775 mg, 2.07 mmol) was added to a suspension of **DBrDNF–U** (426 mg, 1.00 mmol) in DMF (10 mL), and the suspension was stirred at 130 °C for 1 h. The resulting solution was cooled to room temperature and poured into aqueous potassium fluoride. After the precipitate was filtered off, the organic layer was extracted with toluene and washed with water and brine. After removal of the solvent, the crude product was washed with hexane. The obtained yellow solid was filtered through a membrane filter. Yield: 383 mg (88%). ^{1}H NMR (600 MHz, CDCl$_3$): δ 9.23 (d, J = 8.4 Hz, 2H, ArH), 8.95 (d, J = Hz, 2H, ArH), 8.20 (s, 2H, ArH), 8.12 (d, J = 4.2 Hz, 2H, ArH), 7.82 (t, J = 8.4, 6.6 Hz, 2H, ArH), 7.69 (t, J = 7.8 Hz, 2H, ArH), 7.57 (d, 4.2 Hz, ArH). MALDI-TOF-MS (positive) m/z = 435. Anal. Calcd for C$_{26}$H$_{14}$N$_2$OS$_2$: C, 71.87; H, 3.25; N, 6.45. Found: C, 71.58; H, 3.31; N, 6.44.

## 5,9-Bis(dicyanomethylene)-5,9-dihydrodinaphtho[2,1-b:1′,2′-d]furan
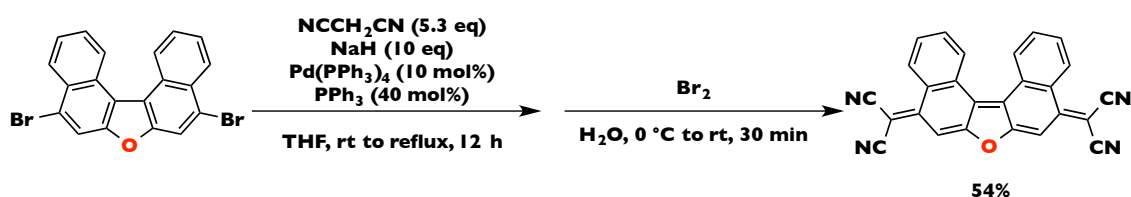
Sodium hydride (55% in oil, 456 mg, 10 mmol) was added to a solution of

malononitrile (353 mg, 5.34 mmol) in dry THF (20 mL), and the mixture was stirred at ambient temperature for 10 min. After addition of tetrakis(triphenylphosphine)palladium (116 mg, 0.10 mmol) and PPh$_3$ (105 mg, 0.4 mmol), **DBrDNF–U** (426 mg, 1.00 mmol) was added. The resulting mixture was refluxed for 12 h. After cooling to room temperature, the THF was removed using a rotary evaporator. The yellow solid was dissolved in water (20 mL), and then bromine (1 mL) was added. After stirring at room temperature for 30 min, the purple precipitate was collected by filtration. The crude material was subjected to silica gel column chromatography using dichloromethane as the eluent. After removal of the solvent, the solid was dissolved in dichloromethane and dispersed in hexane to obtain a dark purple solid. Yield: 212 mg (54%). ^{1}H NMR (600 MHz, CDCl$_3$): δ 8.98 (d, J = 7.8 Hz, 2H, ArH), 8.68 (d, J = 7.2 Hz, 2H, ArH), 7.80–7.78 (m, 4H, ArH), 7.41 (s, 2H, C=C(C)H). MALDI-TOF-MS (negative) m/z = 394.

General procedure for DNF–U alkylation

5,9-Didodecyldinaphthodinaphtho[2,1-b:1′,2′-d]furan (C$_{12}$–DNF–U)
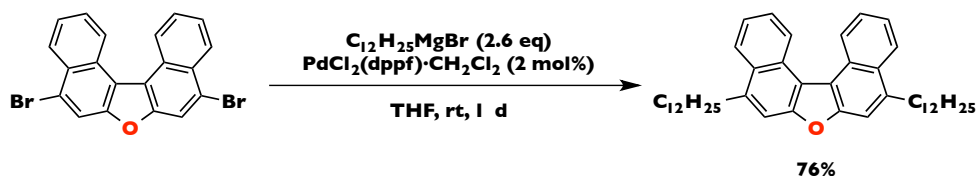
1,1′-Bis(diphenylphosphino)ferrocenepalladium(II)dichloride–dichloromethane adduct (30 mg, 0.036 mmol) was added to a suspension of **DBrDNF–U** (775 mg, 1.82 mmol) in THF (3.6 mL), and then 1.0 M dodecylmagnesium bromide in THF (4.73 mL, 4.73 mmol) was added dropwise to the suspension at 0 °C. The suspension was stirred at room temperature for 24 h. The reaction was quenched with aqueous HCl, and then the organic layer was extracted three times with toluene and the combined organic layer was washed with water and brine. After drying the organic layer over MgSO$_4$, the solvent was removed using a rotary evaporator. The obtained crude product was purified by column chromatography using hexane:chloroform = 9:1 as the eluent, affording a white solid. Yield: 831 mg (76%). ^{1}H NMR (400 MHz, CDCl$_3$): δ 9.17 (d, J = 8.4 Hz, 2H, ArH), 8.26 (d, J = 8.4 Hz, 2H, ArH), 7.72–7.70 (m, 4H, ArH), 7.61 (t, J = 6.6 Hz, 2H, ArH), 3.23 (t, J = 7.2 Hz, 4H, ArCH_2CH$_2$), 1.86 (quin, J = 7.6 Hz, 4H, ArCH$_2$CH_2), 1.51–1.46 (m, 4H, CH$_2$CH_2CH$_2$), 1.43–1.39 (m, 4H, CH$_2$CH_2CH$_2$), 1.34–

1.20 (m, 28H, (CH_2)$_7$), 0.89 (t, J = 8.0 Hz, 6H, CH_3). MALDI-TOF-MS (positive) m/z = 604.

5,9-Dioctyldinaphthodinaphtho[2,1-b:1′,2′-d]furan (C$_8$–DNF–U)
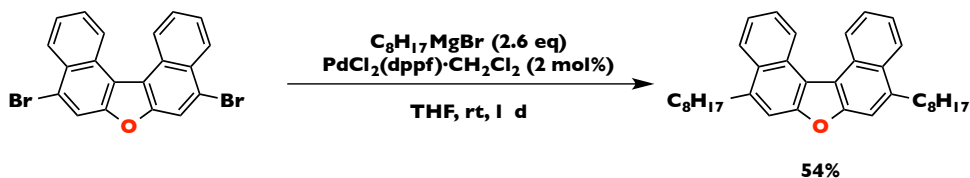
Yield: 595 mg (54%). ^{1}H NMR (600 MHz, CDCl$_3$): δ 9.17 (d, J = 8.4 Hz, 2H, ArH), 8.26 (d, J = 8.4 Hz, 2H, ArH), 7.72–7.70 (m, 4H, ArH), 7.61 (t, J = 6.6 Hz, 2H, ArH), 3.23 (t, J = 6.6 Hz, 4H, ArCH_2CH$_2$), 1.86 (quin, J = 7.8 Hz, 4H, ArCH$_2$CH_2), 1.53–1.48 (m, 4H, CH$_2$CH_2CH$_2$), 1.43–1.37 (m, 4H, CH$_2$CH_2CH$_2$), 1.35–1.25 (m, 12H, (CH_2)$_3$), 0.89 (t, J = 6.6 Hz, 6H, CH_3). MALDI-TOF-MS (positive) m/z = 492.

Single-crystal diffraction data

Single-crystal diffraction data were collected using a Rigaku R-AXIS RAPID II imaging plate diffractometer with Mo Kα or Cu Kα radiation.

Crystal data for **DNF–U**: C$_{20}$H$_{12}$O, M = 268.31, colorless plate, 0.610 × 0.080 × 0.005 mm^3, orthorhombic, $Pccn$, a = 5.9219(9), b = 14.608(2), c = 15.724(2) Å, V = 1360.2(4) Å^3, Z = 4, ρ_{calcd} = 1.310 g cm^{-3}, T = 296 K, $2\theta_{max}$ = 136.3°, Cu Kα radiation, λ = 1.54187 Å, μ = 0.000 mm^{-1}, 14 126 reflections measured, 1246 unique reflections, R_{int} = 10.18%, 104 parameters, R_1 = 0.0780 (I > 2σ(I)), wR_2 = 0.2063 (all data), CCDC–XXX.

Crystal data for **DNT–U**: C$_{20}$H$_{12}$S, M = 284.37, colorless plate, 0.100 × 0.100 × 0.010 mm^3, orthorhombic, $Pbcn$, a = 21.456(2), b = 8.4545(9), c = 7.3522(8) Å, V = 1333.7(3) Å^3, Z = 4, ρ_{calcd} = 1.416 g cm^{-3}, T = 296 K, $2\theta_{max}$ = 54.9°, Mo Kα radiation, λ = 0.71075 Å, μ = 0.000 mm^{-1}, 9683 reflections measured, 1510 unique reflections, R_{int} = 2.99%, 96 parameters, R_1 = 0.0339 (I > 2σ(I)), wR_2 = 0.0963 (all data), CCDC–XXX.

Chapter 5

Summary and Perspectives

In this thesis, the author demonstrated the applications of oxygen-bridged π-conjugated organic semiconductors. Their molecular design, large-scalable synthesis, and intriguing solid-state properties might be of scientific and industrial significance.

In Chapter 2, a synthetic protocol for V-shaped oxygen-bridged molecules, **DNF–V** derivatives, from the corresponding binaphthalene diols and a zeolite catalyst was described. Single-crystal XRD analysis showed that all these molecules form herringbone aggregates with negligible π-core displacements. By introduction of alkyl chains on the **DNF–V** skeleton, molecular alignments with no displacements were successfully achieved, regardless of the alkyl chain positions. However, the substituent positions of the alkyl chains dramatically affected the fundamental properties such as thermal properties, solubility, and photoluminescence derived from the molecular structure.

In Chapter 3, the carrier-transporting abilities of **DNF–V** derivatives and **DNF–W** were evaluated using polycrystalline thin films and single-crystalline films. Single-crystal FET measurements showed that all the **DNF–V** derivatives exhibited high carrier mobilities of over 1.0 cm^2 V^{-1}s^{-1}, because the molecular displacement does not change, regardless of the positions of the alkyl groups. In contrast, **DNF–W**, which formed a one-dimensional π–π stacking structure, had a hole mobility two orders of magnitude lower than those of the **DNF–V** derivatives. These results clearly indicate that the two-dimensional herringbone packing structures of the **DNF–V** derivatives contribute to effective carrier conduction, resulting in high hole mobilities. The results described in Chapters 2 and 3 show that **C$_n$–DNF–VW** is the most favorable framework for light-emitting devices, because high charge mobility and photoluminescence efficiency in the solid state are simultaneously achieved.

In Chapter 4, the author described the electronic properties of furan- or thiophene-containing U-shaped organic semiconductors with twisted π-electronic systems. Compared with thiophene-containing **DNT–U**, furan-containing **DNF–U** showed high solubility, a high fluorescence quantum yield in the solid state, and high hole mobility. The high hole mobility of **DNF–U** is explained by isotropic transfer integrals. Additionally, the author demonstrated the versatility of a zeolite catalyst for the synthesis of fused thiophenes starting from the corresponding naphthalenedithiols.

The results of the author's Ph.D. study verify the usefulness of oxygen-bridged π-conjugated organic semiconductors, based on their high fluorescence characteristics

and carrier transport abilities, which were thought to be difficult to achieve simultaneously. The characteristics of the oxygen-bridged organic semiconductors synthesized in this study suggest that they will be candidates for the next-generation organic electronic devices.

References

(1)   Akamatu, H.; Inokuchi, H.; Matsunaga, Y. *Nature* **1954**, *173*, 168-169.

(2)   Chiang, C. K.; Fincher, C. R., Jr.; Park, Y. W.; Heeger, A. J.; Shirakawa, H.; Louis, E. J.; Gau, S. C.; MacDiarmid, A. G. *Phys. Rev. Lett.* **1977**, *39*, 1098-1101.

(3)   Shirakawa, H.; Louis, E. J.; MacDiarmid, A. G.; Chiang, C. K.; Heeger, A. J. *J. Chem. Soc., Chem. Commun.* **1977**, 578-580.

(4)   Garnier, F.; Hajlaoui, R.; Yassar, A.; Srivastava, P. *Science* **1994**, *265*, 1684-1686.

(5)   E. Katz, H. *J. Mater. Chem.* **1997**, *7*, 369-376.

(6)   Horowitz, G. *Adv. Mater.* **1998**, *10*, 365-377.

(7)   Nelson, S. F.; Lin, Y.-Y.; Gundlach, D. J.; Jackson, T. N. *Appl. Phys. Lett.* **1998**, *72*, 1854-1856.

(8)   Gelinck, G. H.; Geuns, T. C. T.; de Leeuw, D. M. *Appl. Phys. Lett.* **2000**, *77*, 1487-1489.

(9)   Yamada, K.; Okamoto, T.; Kudoh, K.; Wakamiya, A.; Yamaguchi, S.; Takeya, J. *Appl. Phys. Lett.* **2007**, *90*, 072102.

(10)   Tang, C. W.; VanSlyke, S. A. *Appl. Phys. Lett.* **1987**, *51*, 913-915.

(11)   Sariciftci, N. S.; Smilowitz, L.; Heeger, A. J.; Wudl, F. *Science* **1992**, *258*, 1474-1476.

(12)   Yu, G.; Wang, J.; McElvain, J.; Heeger, A. J. *Adv. Mater.* **1998**, *10*, 1431-1434.

(13)   Schmidt-Mende, L.; Fechtenkötter, A.; Müllen, K.; Moons, E.; Friend, R. H.; MacKenzie, J. D. *Science* **2001**, *293*, 1119-1122.

(14)   Moon, H.; Zeis, R.; Borkent, E.-J.; Besnard, C.; Lovinger, A. J.; Siegrist, T.; Kloc, C.; Bao, Z. *J. Am. Chem. Soc.* **2004**, *126*, 15322-15323.

(15)   Anthony, J. E. *Chem. Rev.* **2006**, *106*, 5028-5048.

(16)   Anthony, J. E. *Angew. Chem. Int. Ed.* **2008**, *47*, 452-483.

(17)   Curtis, M. D.; Cao, J.; Kampf, J. W. *J. Am. Chem. Soc.* **2004**, *126*, 4318-4328.

(18)   Coropceanu, V.; Cornil, J.; da Silva Filho, D. A.; Olivier, Y.; Silbey, R.; Brédas, J.-L. *Chem. Rev.* **2007**, *107*, 926-952.

(19)   Lin, Y.-Y.; Gundlach, D. J.; Nelson, S. F.; Jackson, T. N. *IEEE Electron Device Lett.* **1997**, *46*, 606.

(20)   Park, S. K.; Jackson, T. N.; Anthony, J. E.; Mourey, D. A. *Appl.Phys. Lett.* **2007**, *91*, 063514.

(21)   Ebata, H.; Izawa, T.; Miyazaki, E.; Takimiya, K.; Ikeda, M.; Kuwabara, H.; Yui, T. *J. Am. Chem. Soc.* **2007**, *129*, 15732-15733.

(22)   Kang, M. J.; Doi, I.; Mori, H.; Miyazaki, E.; Takimiya, K.; Ikeda, M.; Kuwabara, H. *Adv. Mater.* **2011**, *23*, 1222-1225.

(23)   Nakayama, K.; Hirose, Y.; Soeda, J.; Yoshizumi, M.; Uemura, T.; Uno, M.; Li, W.; Kang, M. J.; Yamagishi, M.; Okada, Y.; Miyazaki, E.; Nakazawa, Y.; Nakao, A.; Takimiya, K.; Takeya, J. *Adv. Mater.* **2011**, *23*, 1626-1629.

(24)   Okamoto, T.; Mitsui, C.; Yamagishi, M.; Nakahara, K.; Soeda, J.; Hirose, Y.; Miwa, K.; Sato, H.; Yamano, A.; Matsushita, T.; Uemura, T.; Takeya, J. *Adv. Mater.* **2013**, 6392-6397.

(25)   Distefano, G.; Jones, D.; Guerra, M.; Favaretto, L.; Modelli, A.; Mengoli, G. *J. Phys. Chem.* **1991**, *95*, 9746-9753.

(26)   Tsuji, H.; Mitsui, C.; Sato, Y.; Nakamura, E. *Adv. Mater.* **2009**, *21*, 3776-3779.

(27)   Oniwa, K.; Kanagasekaran, T.; Jin, T.; Akhtaruzzaman, M.; Yamamoto, Y.; Tamura, H.; Hamada, I.; Shimotani, H.; Asao, N.; Ikeda, S.; Tanigaki, K. *J. Mater. Chem. C* **2013**, *1*, 4163-4170.

(28)   Brédas, J. L.; Calbert, J. P.; da Silva Filho, D. A.; Cornil, J. *Proc. Nat. Acad. Sci.* **2002**, *99*, 5804-5809.

(29)   Cheng, Y. C.; Silbey, R. J.; da Silva Filho, D. A.; Calbert, J. P.; Cornil, J.; Brédas, J. L. *J. Chem. Phys.* **2003**, *118*, 3764-3774.

(30)   Meng, H.; Bao, Z.; Lovinger, A. J.; Wang, B.-C.; Mujsce, A. M. *J. Am. Chem. Soc.* **2001**, *123*, 9214-9215.

(31)   Mitsui, C.; Okamoto, T.; Matsui, H.; Yamagishi, M.; Matsushita, T.; Soeda, J.; Miwa, K.; Sato, H.; Yamano, A.; Uemura, T.; Takeya, J. *Chem.of Mater.* **2013**, *25*, 3952-3956.

(32)   Chatterjea, J. N.; Curtis, R. F.; Dhoubhadel, S. P. *J. Chem. Soc. (Resumed)* **1961**, 765-767.

(33)   Arienti, A.; Bigi, F.; Maggi, R.; Moggi, P.; Rastelli, M.; Sartori, G.; Trere, A. *J. Chem. Soc., Perkin Transactions 1* **1997**, 1391-1394.

(34)   Poutsma, M. L.; Dyer, C. W. *J. Org. Chem.* **1982**, *47*, 3367-3377.

(35)   Marcus, R. A. *Reviews of Modern Physics* **1993**, *65*, 599-610.

(36)   Kohn, W.; Sham, L. J. *Phys. Rev.* **1965**, *140*, A1133-A1138.

(37)   Yamamoto, T.; Takimiya, K. *J. Am. Chem. Soc.* **2007**, *129*, 2224-2225.

(38)   Jurchescu, O. D.; Meetsma, A.; Palstra, T. T. M. *Acta Crystallographica Section B* **2006**, *62*, 330-334.

(39)   *The transfer integrals werecalculated based on PW91 TZP package in Amsterdam Density Functional (ADF) program Users Guide, Department of Theoretical Chemistry, Free University, Amsterdam, Netherlands* **1994**.

(40)   Delgado, M. C. R.; Pigg, K. R.; da Silva Filho, D. t. A.; Gruhn, N. E.; Sakamoto, Y.; Suzuki, T.; Osuna, R. M.; Casado, J.; Hernández, V. c.; Navarrete, J. T. L. p.; Martinelli, N. G.; Cornil, J.; Sánchez-Carrera, R. S.; Coropceanu, V.; Brédas, J.-L. *J. Am. Chem. Soc.* **2009**, *131*, 1502-1512.

(41)   Mori, T. *Bull. Chem. Soc. Jpn* **1998**, *71*, 2509-2526.

(42)   Mori, T.; Kobayashi, A.; Sasaki, Y.; Kobayashi, H.; Saito, G.; Inokuchi, H. *Bull. Chem. Soc. Jpn* **1984**, *57*, 627-633.

(43)   Mewshaw, R. E.; Edsall, R. J.; Yang, C.; Manas, E. S.; Xu, Z. B.; Henderson, R. A.; Keith, J. C.; Harris, H. A. *J. Med. Chem.* **2005**, *48*, 3953-3979.

(44)   Niimi, K.; Kang, M. J.; Miyazaki, E.; Osaka, I.; Takimiya, K. *Org. Lett.* **2011**, *13*, 3430-3433.

(45)   Fürstner, A.; Leitner, A.; Méndez, M.; Krause, H. *J. Am. Chem. Soc.* **2002**, *124*, 13856-13863.

(46)   Minari, T.; Kano, M.; Miyadera, T.; Wang, S.-D.; Aoyagi, Y.; Tsukagoshi, K. *Appl. Phys. Lett.* **2009**, *94*, 093307.

(47)   Kobayashi, S.; Nishikawa, T.; Takenobu, T.; Mori, S.; Shimoda, T.; Mitani, T.; Shimotani, H.; Yoshimoto, N.; Ogawa, S.; Iwasa, Y. *Nat Mater* **2004**, *3*, 317-322.

(48)   Soeda, J.; Hirose, Y.; Yamagishi, M.; Nakao, A.; Uemura, T.; Nakayama, K.; Uno, M.; Nakazawa, Y.; Takimiya, K.; Takeya, J. *Adv. Mater.* **2011**, *23*, 3309-3314.

(49)   Reese, C.; Chung, W.-J.; Ling, M.-m.; Roberts, M.; Bao, Z. *Appl. Phys. Lett.* **2006**, *89*, 202108.

(50)   Sundar, V. C.; Zaumseil, J.; Podzorov, V.; Menard, E.; Willett, R. L.; Someya, T.; Gershenson, M. E.; Rogers, J. A. *Science* **2004**, *303*, 1644-1646.

(51)   Takeya, J.; Yamagishi, M.; Tominari, Y.; Hirahara, R.; Nakazawa, Y.; Nishikawa, T.; Kawase, T.; Shimoda, T.; Ogawa, S. *Appl. Phys. Lett.* **2007**, *90*, 102120.

(52)   Kloc, C.; Simpkins, P. G.; Siegrist, T.; Laudise, R. A. *J. Cryst. Growth* **1997**, *182*, 416-427.

(53)   Podzorov, V.; Pudalov, V. M.; Gershenson, M. E. *Appl. Phys. Lett.* **2003**, *82*, 1739-1741.

(54)   Takeya, J.; Goldmann, C.; Haas, S.; Pernstich, K. P.; Ketterer, B.; Batlogg, B. *J. Appl. Phys.* **2003**, *94*, 5800-5804.

(55)   Yamada, K.; Takeya, J.; Shigeto, K.; Tsukagoshi, K.; Aoyagi, Y.; Iwasa, Y. *Appl. Phys. Lett.* **2006**, *88*, 122110.

(56)   Uemura, T.; Hirose, Y.; Uno, M.; Takimiya, K.; Takeya, J. *Appl. Phys. Express* **2009**, *2*, 111501-111501–111501-111503.

(57)   Soeda, J.; Uemura, T.; Okamoto, T.; Mitsui, C.; Yamagishi, M.; Takeya, J. *Appl. Phys. Express* **2013**, *6*, 076503.

(58)   Kim, W.; Javey, A.; Vermesh, O.; Wang, Q.; Li, Y.; Dai, H. *Nano Lett.* **2003**, *3*, 193-198.

(59)   Pokhodnya, K. I.; Bonner, M. *Chem. Mater.* **2004**, *16*, 5114-5119.

(60)   Shimada, T.; Cho, Y.-H.; Hayashi, T. *J. Am. Chem. Soc.* **2002**, *124*, 13396-13397.

(61)   Fabbri, D.; Delogu, G.; De Lucchi, O. *J. Org. Chem.* **1993**, *58*, 1748-1750.

(62)   He, H.; Chen, L.-Y.; Wong, W.-Y.; Chan, W.-H.; Lee, A. W. M. *Eur. J. Org. Chem.* **2010**, *2010*, 4181-4184.

(63)   Pappenfus, T. M.; Chesterfield, R. J.; Frisbie, C. D.; Mann, K. R.; Casado, J.; Raff, J. D.; Miller, L. L. *J. Am. Chem. Soc.* **2002**, *124*, 4184-4185.

(64)   Pappenfus, T. M.; Raff, J. D.; Hukkanen, E. J.; Burney, J. R.; Casado, J.; Drew, S. M.; Miller, L. L.; Mann, K. R. *J. Org. Chem.* **2002**, *67*, 6015-6024.

(65)   Cardona, C. M.; Li, W.; Kaifer, A. E.; Stockdale, D.; Bazan, G. C. *Adv. Mater.* **2011**, *23*, 2367-2371.

(66)   Boer, R. W. I. d.; Klapwijk, T. M.; Morpurgo, A. F. *Appl. Phys. Lett.* **2003**, *83*, 4345-4347.

(67)   Minari, T.; Miyadera, T.; Tsukagoshi, K.; Aoyagi, Y.; Ito, H. *Appl. Phys. Lett.* **2007**, *91*, 053508.

(68)   Troisi, A.; Orlandi, G. *Phys*. *Rev*. *Lett*. **2006**, *96*, 086601.

(69)   Vehoff, T.; Baumeier, B.; Troisi, A.; Andrienko, D. *J*. *Am*. *Chem*. *Soc*. **2010**, *132*, 11702-11708.

List of Publications

[Publications related to the thesis]

(1) "Furan Fused V-Shaped Organic Semiconducting Materials with High Emission and High Mobility", Nakahara, K.; Mitsui, C.; Okamoto, T.; Yamagishi, M.; Matsui, H.; Ueno, T.; Tanaka, Y.; Yano, M.; Matsushita, T.; Soeda, J.; Hirose, Y.; Sato, H.; Akihito, Y.; Takeya, J. *Chem. Commun.* **2013**, Accepted.

(2) "V-Shaped Organic Semiconductors With Solution Processability, High Mobility, and High Thermal Durability", Okamoto, T.; Mitsui C.; Yamagishi, M.; Nakahara, K.; Soeda, J.; Hirose, Y.; Miwa, K.; Sato, H.; Yamano, A.; Matsushita, T.; Uemura, T.; Takeya, J. *Adv. Mater.* **2013**, *25*, 6392–6397.

(3) "Investigation of Hole Transporting Properties In Thin-Film and Single-Crystal Organic Field-Effect Transistors Based on Dinaphtho[2,1-b:1',2'-d]thiophene", Nakahara, K.; Mitsui, C.; Okamoto, T.; Yamagishi, M.; Soeda, J.; Miwa, K.; Sato, H.; Yamano, A.; Uemura, T.; Takeya, J. *Jpn. J. Appl. Phys.* **2013**, *52*, 05DC10.

(4) "Single-Crystal Field-Effect Transistors with a Furan-Containing Organic Semiconductor Having a Twisted π-Electronic System", Nakahara, K.; Mitsui, C.; Okamoto, T.; Yamagishi, M.; Miwa, K.; Sato, H.; Yamano, A.; Uemura, T.; Takeya, J. *Chem. Lett.* **2013**, *42*, 654–656.

[Publications not related to the thesis]

(5) "Creation of Face-to-face π-π Stacking of Fused Acene Backbones by Aryl-Perfluoroaryl Interactions and Inductions of Charge Transport Properties", Okamoto, T.; Nakahara, K.; Saeki, A.; Seki, S.; Oh, J.-H.; Akkerman, H. B.; Bao, Z.; Miwa, K.; Takeya, J.; Matsuo, Y. *Mater. Rec. Soc. Symp. Proc.* **1360,** OO17.10 (2012).

(6) "Aryl-Perfluoroaryl Substituted Tetracenes: Induction of Face-to-Face π-π Stacking and Enhancement of Charge Carrier Properties", Okamoto, T.; Nakahara, K.; Saeki, A.; Seki, S.; Oh, J. H.; Akkerman, H. B.; Bao, Z.; Matsuo, Y. *Chem. Mater.* **2011**, *23*, 1646–1649.

Acknowledgement

Katsumasa Nakahara
Graduate School of Engineering, Osaka University
December 2013